Interorbital interactions in ytterbium-171

Oscar Bettermann

München 2022

Interorbital interactions in ytterbium-171

Dissertation an der Fakultät für Physik der
Ludwig-Maximilians-Universität München

vorgelegt von

Oscar Bettermann

aus Lausanne, Schweiz

München, den 11. Oktober 2022

Zusammenfassung

Diese Arbeit beschreibt die ausführliche Charakterisierung intra- und interorbitaler Wechselwirkungen in ultrakalten fermionischen Quantengasen von ^{171}Yb Atomen mit zwei elektronischen Orbitalen. Aufgrund ihres metastabilen angeregten elektronischen Uhrenzustandes zusätzlich zum Grundzustand sind erdalkaliartige Elemente wie Ytterbium oder Strontium privilegierte Plattformen für modernste Präzisionsmetrologie und für die Quantensimulation von Systemen mit zwei Orbitalen. Die außergewöhnlich lange Lebensdauer des Uhrenzustands ermöglicht insbesondere die Untersuchung von Quanten-Vielteilchensystemen mit einem zusätzlichen orbitalen Freiheitsgrad. Dies geht über die berühmten Bose- und Fermi-Hubbard-Modelle hinaus, die mit Alkaliatomen zugänglich sind. Bei der Untersuchung der Vielteilchenphysik mit diesen Elementen spielen die interatomaren Wechselwirkungen im Allgemeinen eine entscheidende Rolle.

Wir charakterisieren die intra- und interorbitalen Wechselwirkungen in ^{171}Yb umfassend, indem wir den extrem schmalen optischen Uhrenübergang zwischen dem Grund- und dem Uhrenzustand in einem zustandsunabhängigen optischen Gitter direkt untersuchen. Wir bestimmen mit hoher Genauigkeit die fundamentalen Streulängen, die mit allen Streukanälen für beide Orbitale assoziiert sind und finden Werte, die im Gegensatz zur Situation in anderen erdalkaliartigen Elementen wie ^{173}Yb und ^{87}Sr antiferromagnetische Spinaustauschwechselwirkungen in interorbitalen Paarzuständen implizieren. Die Stabilität dieser Zustände in optischen Gittern wird ebenfalls untersucht, wobei sehr lange Lebensdauern in beiden interorbitalen Wechselwirkungskanälen gefunden werden.

Darüber hinaus beobachten wir eine orbitale Feshbach-Resonanz (OFR), die bisher nur in ^{173}Yb beobachtet wurde und die vollständige Kontrolle über interorbitale Wechselwirkungen ermöglicht. Der interorbitale molekulare Dimer-Zustand, der mit der OFR assoziiert ist, kann direkt über dem Uhrenübergang erzeugt werden und hat eine große Bindungsenergie, die typische Skalen in kalten atomaren Ensembles übersteigt, was ihn für molekulare Uhrenexperimente nützlich machen könnte. Als ersten Schritt in diese Richtung erzeugen wir ein zustandsunabhängiges Potential in erster Ordnung für den Übergang zum Dimer.

Die in dieser Arbeit vorgestellten Ergebnisse machen ^{171}Yb zu einer idealen Plattform für die Quantensimulation von Fermi-Hubbard-Modellen mit orbitalem Freiheitsgrad sowohl im antiferromagnetischen Spinaustausch-Regime als auch im stark wechselwirkenden Regime. Sie führen ^{171}Yb auch als potenziell interessanten Kandidaten für Anwendungen im Bereich der molekularen optischen Uhren ein.

Abstract

This thesis reports on the comprehensive characterization of intra- and interorbital interactions in two-orbital ultracold quantum gases of fermionic ^{171}Yb. Owing to their metastable excited electronic clock state in addition to the ground state, alkaline-earth(-like) (AEL) elements such as ytterbium or strontium are privileged platforms for state-of-the-art precision metrology and for the quantum simulation of two-orbital systems. The remarkably long lifetime of the clock state opens in particular the way for the study of many-body physics with an additional orbital degree of freedom, going beyond the celebrated Bose- and Fermi-Hubbard models accessible using alkali atoms. When studying many-body physics with these elements, interatomic interactions generally play a decisive role.

We extensively characterize intra- and interorbital interactions in ^{171}Yb by directly probing the ultranarrow optical clock transition between the ground and clock states in a state-independent optical lattice. We precisely determine the fundamental scattering lengths associated with the two-particle interaction channels, finding values which notably imply antiferromagnetic spin-exchange interactions in interorbital pair states, as opposed to the situation in other AEL elements such as ^{173}Yb and ^{87}Sr. The stability of these states in optical lattices is probed as well, finding very long lifetimes in both interorbital interaction channels.

We furthermore observe an orbital Feshbach resonance (OFR) which has previously only been witnessed in ^{173}Yb, enabling full control over interorbital interactions. The interorbital molecular dimer state associated with the OFR can be directly addressed on the clock transition and has a large binding energy exceeding typical scales in cold atomic ensembles, making it possibly useful for molecular clock experiments. As a first step in this direction, we demonstrate a first-order state-independent potential for the free-to-bound transition into the dimer.

The results presented in this thesis strongly establish ^{171}Yb as an ideal platform for the quantum simulation of two-orbital Fermi-Hubbard models in both the antiferromagnetic spin-exchanging regime as well as the strongly-interacting regime. They also bring ^{171}Yb to light as a potentially interesting candidate for molecular optical clock applications.

Contents

Introduction

Since the first realization of quantum degenerate bosonic [1, 2] and fermionic [3] gases of neutral atoms nearly thirty years ago, the field of ultracold atoms has experienced a rapid growth. Today, quantum degenerate atomic gases are used in a wide range of applications including quantum metrology [4–6], quantum information processing [7, 8], quantum many-body physics [9–14], molecular physics [15–18] or topology [19–21] to only name a few.

An especially remarkable aspect of ultracold quantum gases is the extraordinary level of control over experimental parameters such as the potential energy or interatomic interactions. The potential landscape experienced by the atomic sample can be fully engineered with laser light, which exerts an optical dipole force on the atoms [22]. In particular, interfering coherent laser beams can be used to create nearly defect-free periodic potentials, so-called optical lattices [23]. Different laser configurations lead to various lattice dimensionalities or geometries, such as cubic [24], triangular [25], honeycomb [26] or kagome [27]. In addition, programmable spatial light modulators such as liquid crystal or digital micromirror devices have been successfully introduced to project arbitrary potentials on atomic samples [28]. Furthermore, the recent advent of quantum gas microscopes [29–31] and optical tweezer arrays [32] has enabled the readout and control of individual atoms, giving access to observables previously out of reach. Moreover, magnetic Feshbach resonances [33] enable extensive control over interatomic interactions via an external magnetic field and have been an essential tool for the realization of quantum gases in the strongly interacting regime [11].

This striking tunability opens the way for the versatile implementation of various many-body quantum systems. These can be precisely engineered to faithfully imitate certain quantum physical systems of interest by replicating the Hamiltonian governing their time evolution, thereby realizing the concept of a quantum simulator envisioned by Feynman back in 1981 [34]. The potentially large number of particles in ultracold atomic ensembles enables the quantum simulation of large systems reaching beyond the computational capabilities of classical computers [35]. Neutral atoms have therefore attracted considerable interest for analog quantum simulation, steering swift developments in recent years [12–14, 35–40]. In parallel, other promising platforms such as trapped ions [41, 42], superconducting resonators [43], photons [44] or Rydberg atoms [45] have emerged as well.

Neutral atoms in optical lattices are particularly well-suited for the investigation of many-body physics [9–14], which has been previously limited to experiments with solid-state sys-

tems. In particular, ultracold spin-1/2 Fermions in optical lattices mimic electrons in solids and thus nearly perfectly realize the celebrated Fermi-Hubbard model describing the dynamics of interacting fermionic particles in a discrete lattice [38, 46, 47]. This model is widely used in solid-state physics since it is believed to describe a broad range of strongly-correlated materials, including high-critical-temperature superconductors in the presence of doping [48, 49]. The Fermi-Hubbard model is especially relevant in the context of quantum simulation since it is only exactly solvable in one dimension [50], relying on numerical approaches such as quantum Monte Carlo [51, 52] or dynamical mean-field theory [53, 54] to make predictions in the two- and three-dimensional cases. Even then, simulations are limited to systems containing only up to a few thousands of atoms. Following the first observation of fermionic quantum gases in the Mott insulating phase [55, 56], an impressive diversity of experiments has explored the Fermi-Hubbard model with alkali atoms [12–14, 31, 46, 47], including recent groundbreaking work probing antiferromagnetic ordering emerging at low temperatures [57–62].

Although such stunning experimental findings have been achieved in the study of Fermi-Hubbard-like models with alkali atoms, these elements only allow for the convenient implementation of single-orbital systems. A rich variety of captivating quantum phenomena however arises from the orbital degree of freedom of the particles such as the Kondo effect [63, 64], heavy-Fermion behavior [64, 65] or colossal magnetoresistance [66, 67]. Since the numerical simulation of these phenomena is a daunting task, our current understanding of their underlying physics is very limited and can greatly benefit from analog quantum simulations to gain further insight.

In this context, alkaline-earth(-like) (AEL) elements such as ytterbium or strontium have been established in the last decade as a privileged platform for the simulation of two-orbital quantum systems, in addition to being used for state-of-the-art precision metrology. In contrast to alkali metals, these elements possess two valence electrons, leading to a richer helium-like electronic level structure. Of central importance is the lowest-lying metastable excited electronic «clock» state, which is connected to the ground state via an ultranarrow optical «clock» transition [68].

Fermionic isotopes of AEL atoms such as ^{171}Yb, ^{173}Yb or ^{87}Sr enable the quantum simulation of Fermi-Hubbard models generalized to multiple orbitals, reaching beyond the capabilities of alkali atoms [39, 69–72]. Indeed, owing to the extremely long lifetime of the clock state, these atoms are ideal candidates for the study of physical systems containing atoms in two distinct electronic states, or orbitals. In the limit of zero magnetic fields, atoms in different orbitals interact via spin-exchange interactions [69, 73–76]. Together with the use of state-dependent optical lattice potentials [75–77] featuring potentially very different mobilities between atoms in distinct orbital states, this opens the way for the investigation of quantum magnetism such as the celebrated Kondo [78–81], Kondo lattice [69, 82–84] or Kugel-Khomskii [69] models. Promising experimental findings have been made in this direction through the observation of interorbital spin exchange in state-dependent lattices [75, 76].

Interactions between two ground- or clock-state AEL atoms are nearly independent of the nuclear spin, a consequence of the zero total angular momentum in both states [69, 85]. This leads to a potentially large SU(N) symmetry of the Hamiltonian describing the system at zero

magnetic field [73, 86, 87], where N is the number of nuclear spin states. This number is particularly large in ^{173}Yb ($N = 6$) and in ^{87}Sr ($N = 10$). This is in strong contrast with the SU(2) symmetry arising in alkali quantum gases or in solid-state systems and has for instance enabled the observation of Mott insulators with enhanced SU(N) symmetry [88–90], which are believed to show exotic magnetic ordering at low temperatures [91–94].

Ytterbium, which has been first cooled down to quantum degeneracy nearly twenty years ago [95], is now relatively commonly used in multiple cold-atom experiments over the world. Its two fermionic isotopes, ^{171}Yb and ^{173}Yb, are particularly promising candidates for the investigation of two-orbital many-body physics. In this context, ^{173}Yb has to this day attracted the greatest attention owing to its six different nuclear spin states which have led to the experimental demonstration of fermionic Mott insulators with SU($N \leq 6$) symmetry [88–90]. Interorbital interactions between atoms in distinct electronic ground or clock states are very well characterized and most notably imply ferromagnetic spin-exchange interactions [73]. This enables for instance the study of the ferromagnetic Kondo lattice model, which is relevant in the context of colossal magnetoresistance. However, the finite elastic scattering between ground-state atoms [96] as well as the ferromagnetic nature of interorbital spin-exchange interactions hinder the study of crucial models such as the antiferromagnetic Kondo lattice model [69, 82–84, 97], which has a rich phase diagram expected to describe for instance heavy-Fermion behavior in metals [64, 98].

On the other hand, ^{171}Yb, which only features two nuclear spin states, has to this day rather been considered in the context of optical atomic clocks [6, 99, 100] or quantum information processing [101, 102]. Given the almost vanishing elastic scattering of atoms in the electronic ground state in ^{171}Yb [96], this isotope has the potential to be a promising candidate for quantum simulations as well. The suitability of ^{171}Yb for the implementation of two-orbital systems can however only be reliably assessed with the full knowledge of intra- and interorbital interactions in this isotope. In the frame of this thesis, we extensively characterize these interactions by probing the elastic scattering of atomic pairs in the electronic clock state as well as in superpositions of ground and clock state using lattice spectroscopy on the narrow-line clock transition. We furthermore probe inelastic scattering in these states by measuring their lattice lifetime.

Remarkably, interorbital interactions between atoms in the electronic ground and clock states can be tuned over a large range via an external magnetic field, using the so-called orbital Feshbach resonance mechanism [103, 104] which has been predicted [103] and observed [105, 106] for the first time in ^{173}Yb. This novel type of Feshbach resonance, which intrinsically differs from usual magnetic Feshbach resonances [33], enables the study of two-orbital samples in the strongly interacting regime and has inspired numerous theoretical proposals in recent years [97, 107–117]. The orbital Feshbach resonance has been used to this day as a central experimental tool for the observation of multiorbital Fermi polarons [118] as well as for the study of transport in the mass-imbalanced Fermi-Hubbard model [119]. Alternatively, interorbital interactions can be enhanced using confinement-induced resonances [120, 121], which have been demonstrated in ^{173}Yb [75]. In this work, we also observe and characterize an orbital Feshbach resonance in ^{171}Yb for the first time, enabling extensive control

over interorbital interactions in this isotope as well.

Finally, the ultranarrow transition in AEL elements has enabled the development of the currently most accurate clocks in the world, which probe the clock line in ultracold ytterbium or strontium atoms in state-independent optical lattices [6, 122]. Impressive recent technical progress has led to optical atomic clocks with relative uncertainties on the 10^{-18} level [99, 123], paving the way for applications in general relativity [99, 124–127], improved constraints on dark matter [128, 129] or tests of fundamental physics [130]. The advent of such clocks also makes AEL elements solid candidates to replace caesium in the definition of the SI second [131]. Another exciting application is the development of molecular lattice clocks [132, 133], which could enable fundamental measurements beyond the reach of atomic clocks such as precision tests of electron-to-proton mass ratio variations [134]. In particular, the production of ultracold molecules on the clock transition would enable molecular spectroscopy on the Hz level [135]. We find an interorbital molecular dimer state in ^{171}Yb that can be directly addressed on the clock transition, with properties such as its binding energy that can be precisely probed spectroscopically. This dimer lies at the heart of the orbital Feshbach resonance mechanism since it is the least-bound state supported by the closed interorbital interaction channel. We find this state to have a large binding energy exceeding all other typical scales in cold atomic ensembles, making it a potentially interesting candidate in the context of optical molecular clocks. As a first step in this direction, we demonstrate a first-order state-insensitive trapping potential for the free-to-bound transition into the dimer state.

Outline

This thesis consists in seven chapters, including this introduction, which are organized as follows.

Chapter 2 reviews the electronic structure of ytterbium as well as its most relevant atomic properties, highlighting the key differences between both fermionic isotopes ^{171}Yb and ^{173}Yb. A detailed description of scattering between atoms in the electronic ground and clock state is given, showing in particular the mechanism underlying the orbital Feshbach resonance in AEL atoms. Finally, the physics of multiorbital quantum gases in optical lattices is discussed, including relevant models such as the Kondo lattice model.

In **Chapter 3**, an overview of the experimental apparatus and relevant techniques used to prepare and detect ultracold gases of ytterbium with electronic as well as nuclear spin degrees of freedom is given. In particular, high-precision spectroscopy on the ultranarrow clock line in a state-independent lattice is described in detail as it is the most central experimental technique used throughout this work. The chapter ends with the measurement of the differential and quadratic Zeeman shifts in ^{171}Yb, which are important atomic properties for the experiments presented in the following chapters.

In **Chapter 4**, a set of four measurements characterizing intra- and interorbital interactions in ^{171}Yb is presented. The s-wave scattering lengths corresponding to the interorbital pair states and to the intraorbital pair state in the clock state are precisely determined via clock-line spectroscopy at low magnetic fields. Furthermore, inelastic scattering in these states is

probed by measuring their lifetime in optical lattices.

Chapter 5 reports on the first experimental observation of an orbital Feshbach resonance in ^{171}Yb. By means of clock-line spectroscopy at large magnetic fields, the energy of both the least-bound state supported by the closed-channel interatomic potential as well as the free open-channel pair state is measured. The resonance position, resonance width and background scattering length are characterized by fitting the data in the vicinity of the resonance to an effective open-channel model. In a separate measurement, the position of the scattering length zero-crossing is precisely determined as well.

Chapter 6 focuses on the least-bound interorbital molecular dimer state associated with the orbital Feshbach resonance. The dimer is created via direct clock-line spectroscopy both in a cubic and a single-axis optical lattice, exhibiting a large binding energy. A first-order state-independent potential is engineered for the free-to-bound transition at a given optical lattice depth by introducing a suitable differential light shift between the ground and clock states.

Chapter 7 concludes this work by briefly summarizing the most important findings obtained throughout this thesis and gives an outlook about future prospects in exploring multiorbital many-body systems with antiferromagnetic spin exchange and tunable interorbital interactions using ^{171}Yb atoms.

Publications

The main results presented in this thesis have been published in the following research article:

- <u>O. Bettermann</u>, N. Darkwah Oppong, G. Pasqualetti, L. Riegger, I. Bloch, and S. Fölling, *Clock-line photoassociation of strongly bond dimers in a magic-wavelength lattice*, arXiv: 2003.10599

During the course of this thesis, the following additional research articles have been published:

- N. Darkwah Oppong, G. Pasqualetti, <u>O. Bettermann</u>, P. Zechmann, M. Knap, I. Bloch, and S. Fölling, *Probing transport and slow relaxation in the mass-imbalanced Fermi-Hubbard model*, Phys. Rev. X **12**, 031026 (2022)

- N. Darkwah Oppong, L. Riegger, <u>O. Bettermann</u>, M. Höfer, I. Bloch, and S. Fölling, *Observation of Coherent Multiorbital Polarons in a Two-Dimensional Fermi Gas*, Phys. Rev. Lett. **122**, 193604 (2019)

Two-orbital physics with ultracold ytterbium atoms

Alkaline-earth(-like) atoms such as ytterbium or strontium are a privileged platform for the analog quantum simulation of two-orbital many-body physics as well as for the the implementation of state-of-the-art optical atomic clocks. In this chapter, we review the electronic structure of ytterbium together with some relevant atomic properties, in particular for the fermionic isotopes ^{171}Yb and ^{173}Yb. After that, a theoretical description of scattering between atoms in the electronic ground and clock state is given, leading in particular to the orbital Feshbach resonance mechanism which makes interorbital interactions tunable with an external magnetic field. The physics of two-orbital quantum gases in optical lattices is described as well, leading to the Kondo lattice model and mass-imbalanced Fermi-Hubbard models as examples of possible implementations with fermionic ytterbium isotopes.

2.1 Ytterbium electronic structure and atomic properties

Ytterbium is a rare-earth element in the lanthanide series which has the atomic number $Z = 70$. It has multiple stable isotopes, namely five bosonic ones with mass numbers $A = 168, 170, 172,$ 174 and 176 as well as two fermionic ones with $A = 171$ and 173. All bosonic isotopes have a vanishing nuclear spin $I = 0$ while both fermionic isotopes ^{171}Yb and ^{173}Yb have non-zero nuclear spins $I = 1/2$ and $I = 5/2$, respectively. Most isotopes have a relatively large natural abundance above 10%, which makes ytterbium very convenient for the almost seemless switching between different isotopes in atomic physics experiments or for the study of inter-isotope mixtures [96]. In particular, the isotope ^{171}Yb used throughout this work has a natural abundance about 14% [136].

   In the ground state, ytterbium has an electron configuration given by $[\text{Xe}]\,4f^{14}6s^2$, which features a closed f shell. The resulting helium-like electronic structure is therefore mostly determined by the two valence electrons in the outer $6s^2$ shell in the same way as in alkaline-earth elements such as magnesium or strontium. For this reason, ytterbium is sometimes referred to as an alkaline-earth-like element. In Fig. 2.1, we show the energy level diagram of the electronic states relevant to this work, also including the relevant electronic transitions. Similar to the helium atom, the level diagram is split into two manifolds, the electronic spin-singlet
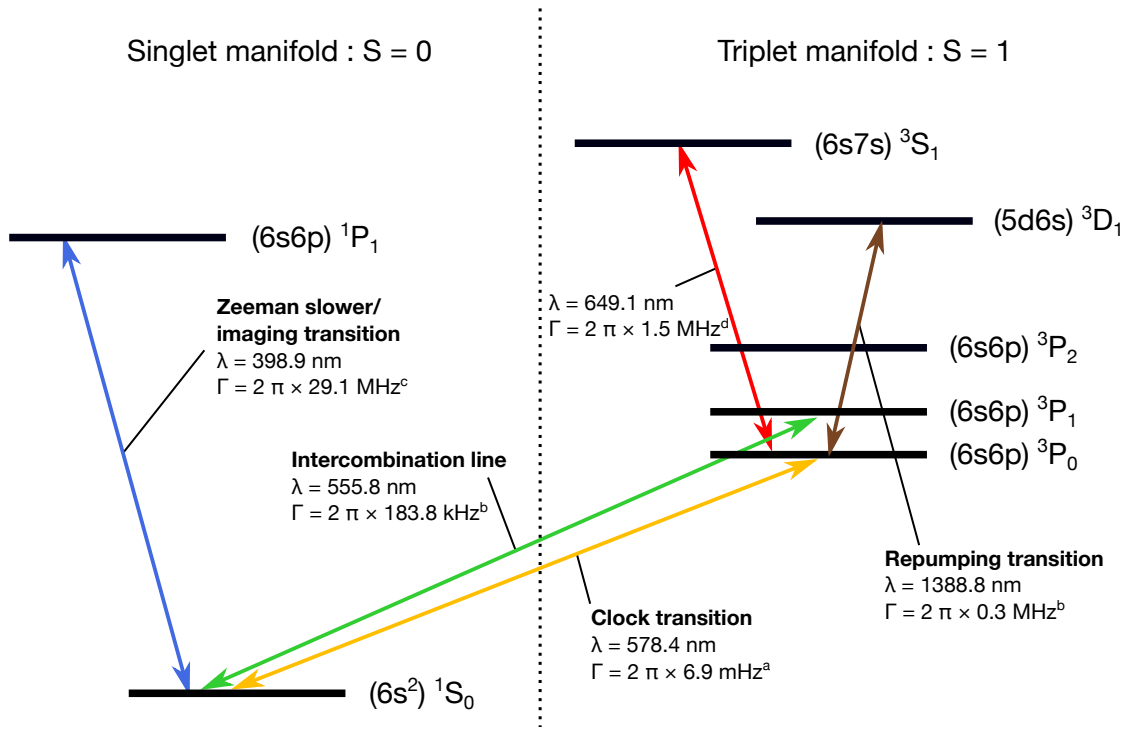
Figure 2.1 – **Relevant lowest-lying electronic states and optical transitions in ^{171}Yb.** We show the level diagram (not to scale) including the relevant electronic orbitals for this work. Each electronic state is labeled with its associated Russel-Sanders (RS) symbol $^{2S+1}L_J$, assuming bare LS eigenstates. The hyperfine structure is omitted for simplicity. Relevant electronic transitions are represented by colored double-arrows between states. For each transition, the vacuum wavelength λ and natural linewidth Γ is specified. The values for Γ are taken from Refs. [68][a],[137][b],[138][c] and [139][d].

manifold with spin $S = 0$ and spin-triplet manifold with spin $S = 1$. In good approximation, the electronic states can be labeled in Russel-Sanders (RS) notation $^{2S+1}L_J$. This suggests bare LS eigenstates where the electronic spin S, orbital angular momentum L and total electronic angular momentum $|L - S| < J < L + S$ are good quantum numbers.

Imaging and Zeeman slowing transition

Within an electronic spin manifold with $S = 0$ or $S = 1$, broad dipole-allowed transitions are featured. One example is the 399 nm $^1S_0 \leftrightarrow {}^1P_1$ transition, which has a natural linewidth $\Gamma = 2\pi \times 29.1$ MHz [138] and is almost closed, with negligible decay to other lower-lying electronic states. In our experiment, the large linewidth and scattering rate make this transition well-suited for Zeeman slowing and for in-situ absorption imaging of ground-state atoms.

Intercombination line

In contrast to transitions within an electronic spin manifold, transitions involving a spin flip $\Delta S = \pm 1$ violate the electric dipole selection rules and are therefore strictly forbidden in a pure LS coupling picture. However, this picture is not exact in ytterbium, which has a rather

large atomic number Z, and a significant mixing between the $^1P_1$ and $^3P_1$ states originates from spin-orbit coupling [140]. This induces a decay channel for the $^3P_1$ state to the ground state $^1S_0$. As a result, a so-called intercombination line $^1S_0 \leftrightarrow {}^3P_1$ of wavelength 555.8 nm and natural linewidth $\Gamma = 2\pi \times 183.8$ kHz [137] exists. This transition is closed and of intermediate strength. It is therefore very suitable for the operation of the magneto-optical trap in our experiment, providing a remarkably low Doppler temperature $T_D = \hbar\Gamma/2k_B = 4.4\,\mu$K (where k_B denotes the Boltzmann constant) while ensuring a sufficiently large capture velocity. In our experiment, this transition is also used for spin state preparation and detection.

Clock transition

Arguably the most remarkable transition in ytterbium and other alkaline-earth atoms such as strontium is the $^1S_0 \leftrightarrow {}^3P_0$ transition, which is doubly forbidden in the LS coupling picture as it violates the $J = 0 \leftrightarrow J' = 0$ selection rule in addition to the $\Delta S = 0$ rule. In fermionic isotopes with $I \neq 0$, the hyperfine interaction leads to a small admixture of the $^3P_0$, $^3P_1$ and $^3P_2$ states [140], ultimately yielding a finite coupling between the $^1S_0$ and $^3P_0$ states via the coupling between $^1S_0$ and $^3P_1$ described above. The resulting $^1S_0 \leftrightarrow {}^3P_0$ transition occurs at a wavelength $\lambda = 578.4$ nm and has an extraordinarily small natural linewidth $\Gamma = 2\pi \times 6.9$ mHz [68].

This particularly narrow so-called «clock» transition has two important implications. On one hand, its large optical frequency yields an impressive quality factor $Q \sim 10^{17}$ which makes these atoms particularly promising in the context of optical atomic clocks [6] and credible candidates to replace caesium in the definition of the SI second [131]. The very low sensitivity of the $^1S_0$ and $^3P_0$ states to external magnetic fields owing to their zero total electronic angular momentum $J = 0$ is a further important property for the implementation of optical atomic clocks. In this work, we extensively use the narrow linewidth of the clock transition to spectroscopically investigate interactions between ytterbium atoms in the $^1S_0$ and $^3P_0$ states.

On the other hand, the extremely small linewidth of the transition implies a remarkably long lifetime above 10 s of the $^3P_0$ state before decaying to the ground state, making the $^3P_0$ «clock» state metastable. Consequently, both electronic states $^1S_0$ and $^3P_0$ can be used to implement systems featuring an additional orbital degree of freedom, enabling the study of two-orbital many-body physics with ytterbium atoms [69].

Other transitions

In addition to the three main transitions discussed above, we mention two other transitions relevant to this work. First, the repumping transition $^3P_0 \leftrightarrow {}^3D_1$ of wavelength $\lambda = 1388.8$ nm and linewidth $\Gamma = 2\pi \times 0.3$ MHz [137] is used in our experiment to repump atoms intially in the $^3P_0$ state back to the ground state in order to be imaged on the $^1S_0 \leftrightarrow {}^1P_1$ line. Finally, the broad $^3P_0 \leftrightarrow {}^3S_1$ transition at 649.1 nm is relevant for the calculation of the atomic polarizability in the ground and in the clock state.

	^{171}Yb	^{173}Yb	^{174}Yb
^{171}Yb	**-2.8(3.6)**	-578(60)	**429(13)**
^{173}Yb		199(2)	139(2)
^{174}Yb			105(2)

Table 2.1 – **Ground-state s-wave scattering lengths between ytterbium atoms in different isotopes.** All values are taken from Ref. [96] and in units of the Bohr radius a_0. The bold numbers refer to scattering lengths directly relevant to this work.

Nuclear spin states

Both ^{1}S$_0$ and ^{3}P$_0$ states have a zero total electronic angular momentum $J = 0$ such that their total angular momentum F is directly given by the nuclear spin I. As a consequence, ^{173}Yb ($I = 5/2$) features six different spin states $m_F \in \{-5/2, -3/2, \ldots, +5/2\}$ while ^{171}Yb ($I = 1/2$) only has two different $m_F \in \{\pm 1/2\}$.

A central feature arising from $J = 0$ is that I is almost perfectly decoupled from J in both ^{1}S$_0$ and ^{3}P$_0$ states. This implies that the scattering properties of pairs with ^{1}S$_0$ and ^{3}P$_0$ atoms are independent of the nuclear spin [69], with the exception of the Pauli exclusion principle for Fermions. The interactions between two ytterbium atoms in ^{1}S$_0$ or in ^{3}P$_0$ can therefore be described with a single s-wave scattering length. This property arises from the fact that the total angular momentum is solely contained in the atomic nucleus and is therefore only weakly affected by collisions occurring on the scale of the electronic cloud radius.

In particular, the decoupling between I and J involves an SU(N) spin symmetry of the Hamiltonian describing an ultracold gas of ytterbium atoms, where N denotes the number of different spin states [69]. The isotope ^{171}Yb has $N = 2$, which leads to the usual SU(2) spin symmetry occuring in electron gases and accessible with alkali atoms. On the other hand, ^{173}Yb features a potentially large spin symmetry SU($N \le 6$) arising from $N = 6$. This enables the study of Fermi-Hubbard models with enhanced SU(3) color symmetry or even larger SU(N) symmetries [89, 90], which are expected to show exotic magnetic ordering at low temperatures [91–94].

Intra- and interisotope interactions

At ultracold temperatures where energies are low, interactions between two ytterbium atoms in the ground state ^{1}S$_0$ or in the clock state ^{3}P$_0$ can be described by a single s-wave scattering length owing to the interactions being independent of the m_F spin state. In Table 2.1, we show the most relevant ground-state intra- and interisotope scattering lengths for this work measured by means of two-color photoassociation spectroscopy [96].

The extremely small scattering length in ^{171}Yb is striking and in strong contrast with the intermediate value in the other fermionic isotope, ^{173}Yb. This feature is highly desirable in the implementation of certain two-orbital many-body systems. One example is the Kondo lattice model with ytterbium which is discussed in Section 2.3.3 and assumes vanishing interactions
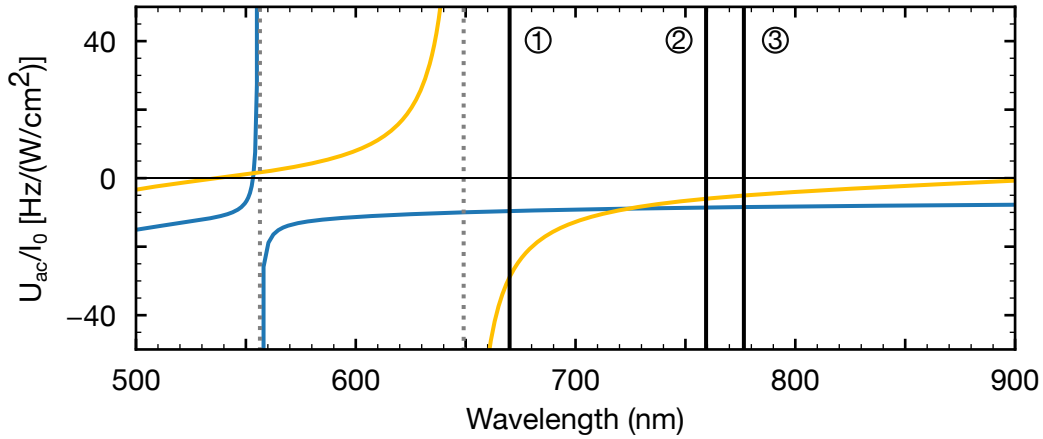
Figure 2.2 – **State-dependent and state-independent potentials in ^{171}Yb.** We show the scalar light shift U_{ac} relative to the laser light intensity I_0 for atoms in the $^1S_0$ (blue solid lines) and $^3P_0$ states (yellow solid lines). The shifts are determined from the LS coupling estimate described in Ref. [142]. The dotted vertical lines denote the atomic transitions $^1S_0 \leftrightarrow {}^3P_1$ and $^3P_0 \leftrightarrow {}^3S_1$ occuring at 556 nm and 649 nm, respectively. The solid vertical black lines denote the wavelengths relevant to this work, the ① state-dependent lattice wavelength (670 nm), ② magic wavelength (759.4 nm), ③ light-shift-canceling wavelength (776.6 nm) for the free-to-bound transition investigated in Chapter 6. The simple model used here does not predict the magic wavelength where both light shifts are equal very accurately. For a better prediction, we refer to the calculation presented in Ref. [143].

between ground-state atoms.

On the other hand, the almost zero ground-state scattering length in ^{171}Yb presents an experimental challenge when performing forced evaporative cooling on these atoms, which consequently thermalize extremely slowly. A solution discussed in Section 3.1.3 is to evaporate ^{171}Yb atoms together with ^{174}Yb atoms to exploit the relatively large scattering length between these isotopes.

Note that only the elastic scattering between ground-state ytterbium atoms is discussed here. In Chapter 4, elastic as well as inelastic scattering in interorbital as well as in clock-state pairs are comprehensively characterized.

State-dependent and state-independent potentials

Atoms trapped with laser light experience an ac Stark shift proportional to the light intensity and to the atomic polarizability. In general, the polarizability depends on the wavelength of the trapping light and on the electronic state of the atom. The dependence of the light shift relative to the laser light intensity is shown in Fig. 2.2 for ^{171}Yb atoms in the $^1S_0$ and $^3P_0$ states, following a LS coupling estimate calculation described in Ref. [142]. In the vicinity of the $^3P_0 \leftrightarrow {}^3S_1$ transition at 649 nm, trapping potentials with large depth ratio between $^1S_0$ and $^3P_0$ atoms can be engineered such as the state-dependent lattice (introduced in Section 3.1.1) in our experiment, which operates at 670 nm. These potentials are especially relevant when implementing two-orbital Fermi-Hubbard models with distinct mobility between different orbitals

such as the Kondo lattice model or the mass-imbalanced Fermi-Hubbard model introduced in Section 2.3.

On the other hand, the so-called magic wavelength where both atomic polarizabilities are equal is crucial in the context of precision spectroscopy, as discussed in Section 3.3.3. Nearly all the experiments reported in this work are performed at this magic wavelength of 759.4 nm, with the only exception of the light-shift-canceling potential for the free-to-bound transition reported in Chapter 6.

2.2 Interactions in two-orbital ultracold quantum gases

When using ultracold atoms as a platform for the analog quantum simulation of many-body physics, interactions between atoms generally play a crucial role in the evolution of the system and need to be well-understood. In this section, elastic scattering between two ultracold atoms is described, leading to the introduction of the s-wave scattering length. This is a key quantity containing most information about low-energy scattering in atomic samples. We then move on to discuss how interorbital interactions between atoms in the electronic ground state $^1S_0$ and clock state $^3P_0$ take place in the specific case of ^{171}Yb. In particular, we show how both interorbital interaction channels lead to an orbital Feshbach resonance allowing to tune interactions between $^1S_0$ and $^3P_0$ atoms with an external magnetic field.

2.2.1 Low-energy elastic scattering of atoms

Here, we consider scattering in a dilute gas of ultracold neutral atoms with density n. Atoms are assumed to interact via a conservative short-range potential with characteristic length scale r_0 beyond which the potential rapidly vanishes, such as a van der Waals potential. If the mean interparticle distance $n^{-1/3}$ is much larger than r_0, only two-body collisions need to be considered. Assuming isotropic interactions, the potential $V(r)$ is central and the problem of two interacting atoms can in general be reduced to a single-particle potential scattering problem in the center-of-mass frame following the Schrödinger equation

$$\left[\frac{\hbar^2 \nabla^2}{2m_r} + V(r) \right] \psi(\mathbf{r}) = E\psi(\mathbf{r}), \tag{2.1}$$

where m_r is the reduced mass and $\mathbf{r}$ the relative coordinate for the two-body problem. At large $r \to \infty$ such that $V(r) \to 0$, the asymptotically free solutions $\psi_{\mathbf{k}}(\mathbf{r})$ for the scattering problem take the energy solutions $E_{\mathbf{k}} = \hbar^2 \mathbf{k}^2 / 2m_r$, where $\mathbf{k}$ denotes the wave vector of the scattered wave. A standard ansatz wavefunction fulfilling this boundary condition is

$$\psi_{\mathbf{k}}(\mathbf{r}) = e^{i\mathbf{k}\cdot\mathbf{r}} + f(\mathbf{k}, \theta) \frac{e^{ikr}}{r}. \tag{2.2}$$

The first term is an incoming plane wave while the second term describes an outgoing spherical wave modulated with the scattering amplitude $f(\mathbf{k}, \theta)$. The scattering amplitude contains all

the information about the scattering process and is related to the differential scattering cross section via $d\sigma/d\Omega = |f(\mathbf{k}, \theta)|^2$. A partial-wave expansion of $f(\mathbf{k}, \theta)$ leads to

$$f(\mathbf{k}, \theta) = \frac{1}{2ik} \sum_{l=0}^{\infty} (2l+1)\left(e^{2i\delta_l} - 1\right) P_l(\cos\theta),$$ (2.3)

defining the scattering phase shift δ_l of the lth partial wave and the Legendre polynomial $P_l(x)$ of order l. For short-range potentials behaving as r^{-6} such as the van der Waals potential and low energies k, the scattering phase shift varies as k^{2l+1} for $l \in \{0, 1\}$ and as k^4 for all higher partial waves $l \geq 2$ [144]. Therefore for $k \to 0$ only the $l = 0$ term is relevant in the sum in Eq. (2.3), the so-called *s*-wave. This is a good approximation for cold atomic ensembles and means that at low energies the angular properties of the scattering cannot be resolved anymore, leading to a scattering amplitude

$$f(k) = \frac{1}{k \cot \delta_0(k) - ik}.$$ (2.4)

The s-wave phase shift can be expanded for low energies, leading to [144]

$$k \cot \delta_0(k) \approx -\frac{1}{a} + \frac{1}{2} r_{\text{eff}} k^2,$$ (2.5)

which defines the s-wave scattering length a and the effective range r_{eff} representing the first energy-dependent correction to the scattering amplitude.

In practice, when calculating low-energy properties of the system, details about the real interatomic potential can be replaced by an effective potential yielding the same scattering length a as the original problem, neglecting effective range contributions. A good choice is the Fermi pseudopotential

$$V(\mathbf{r}) = \frac{4\pi\hbar^2 a}{2m_r} \delta^{(3)}(\mathbf{r})$$ (2.6)

describing zero-range contact interactions.

2.2.2 The van der Waals potential

At large interatomic distances, the molecular interaction potential between two neutral atoms is dominated by the attractive van der Waals potential defined for $l = 0$ as

$$V_{\text{vdW}}(r) = -\frac{C_6}{r^6}$$ (2.7)

and which is entirely characterized by the single C_6 coefficient. Typical scales are defined by the van der Waals length [33]

$$l_{\text{vdW}} = \frac{1}{2} \left(\frac{2m_r C_6}{\hbar^2}\right)^{-1/4}$$ (2.8)

and energy

$$E_{\text{vdW}} = \frac{\hbar^2}{2m_r l_{\text{vdW}}^2}.$$ (2.9)

Remarkably, the two-body problem defined in Eq. (2.1) can be solved for any type of short-range potential of the form $V(r) = -\alpha/r^n$ using the semiclassical WKB approximation to describe the atomic motion in the potential well. In the $n = 6$ case corresponding to a van der Waals potential, the s-wave scattering length is given by the expression [145]

$$a = \bar{a}\left[1 - \tan\left(\Phi - \frac{\pi}{8}\right)\right], \tag{2.10}$$

defining the zero-energy semiclassical phase shift

$$\Phi = \int_{\tilde{r}}^{\infty} dr \sqrt{-2mV(r)} \tag{2.11}$$

where $\tilde{r}$ is the classical turning point obeying $V(\tilde{r}) = 0$. The mean scattering length $\bar{a}$ is defined as

$$\bar{a} = \sqrt{2\gamma}\frac{\Gamma(3/4)}{\Gamma(1/4)} \tag{2.12}$$
$$\approx 0.956\, l_{\text{vdW}}$$

with the Gamma function $\Gamma(x)$ and asymptotic parameter

$$\gamma = \sqrt{\frac{2m_r}{m_e C_6}}, \tag{2.13}$$

where m_e denotes the electron mass. The corresponding mean energy is given by

$$\bar{E} = \frac{\hbar^2}{2m_r \bar{a}^2}. \tag{2.14}$$

In addition to the s-wave scattering length a, the effective range can be analytically calculated as well, yielding [145]

$$r_{\text{eff}} = \frac{\bar{a}}{3}\left[\frac{\Gamma(1/4)}{\Gamma(3/4)}\right]^2\left[1 - 2\frac{\bar{a}}{a} + 2\left(\frac{\bar{a}}{a}\right)^2\right]. \tag{2.15}$$

2.2.3   Two-orbital interaction channels

The concepts and derivations presented in Sections 2.2.1 and 2.2.2 are very general and apply to a variety of scattering problems. Here, we move to the specific case of interactions between ^{171}Yb atoms in the electronic ground state ^{1}S$_0$ and in the electronic clock state ^{3}P$_0$. We introduce the notation $|g\rangle \equiv |^1\text{S}_0\rangle$ and $|e\rangle \equiv |^3\text{P}_0\rangle$ to describe the orbital state of one atom. Similarly, we introduce the notation $|\uparrow\rangle \equiv |m_F = +1/2\rangle$ and $|\downarrow\rangle \equiv |m_F = -1/2\rangle$ to describe the nuclear spin state of one atom.

Interactions between atoms in the same orbital $X \in \{g, e\}$ are characterized by two intraorbital scattering lengths a_{gg} and a_{ee}. The corresponding interaction states are given by

$$|gg\rangle \equiv |gg\rangle \otimes |s\rangle, \tag{2.16}$$
$$|ee\rangle \equiv |ee\rangle \otimes |s\rangle,$$

where the spin singlet state $|s\rangle = (|\uparrow\downarrow\rangle - |\downarrow\uparrow\rangle)/\sqrt{2}$ ensures that the the total wavefunction is antisymmetric under particle exchange.

On the other hand, two interorbital pair states with one atom in $|g\rangle$ and one atom in $|e\rangle$ can be defined with both orbital and spin degrees of freedom either symmetric or antisymmetric, namely

$$
\begin{aligned}
|eg^+\rangle &= \frac{1}{\sqrt{2}} (|eg\rangle + |ge\rangle) \otimes |s\rangle, \\
|eg^-\rangle &= \frac{1}{\sqrt{2}} (|eg\rangle - |ge\rangle) \otimes |t\rangle,
\end{aligned}
\tag{2.17}
$$

with the spin triplet state $|t\rangle \in \{|\uparrow\uparrow\rangle, |\downarrow\downarrow\rangle, (|\uparrow\downarrow\rangle + |\downarrow\uparrow\rangle)/\sqrt{2}\}$. Here, the corresponding interorbital s-wave scattering lengths are defined as a_{eg}^+ and a_{eg}^-. Overall, only four s-wave scattering lengths are required to fully describe all interaction channels. In order to characterize two-orbital interactions in ^{171}Yb, $a_{eg}^\pm$ and a_{ee} need to be experimentally determined in addition to a_{gg}, which has been measured in Ref. [96].

At zero magnetic field, where all spin states are degenerate, both interorbital pair states defined in Eq. (2.17) are eigenstates of the Hamiltonian describing the two-body interactions. The corresponding eigenenergies $U_{eg}^\pm$ depend on the external potential and on the interorbital scattering lengths $a_{eg}^\pm$. At finite magnetic fields B, however, a mixing between $|eg^+\rangle$ and $|eg^-\rangle$ is induced by the differential Zeeman shift between $|g, m_F\rangle$ and $|e, m_{F'}\rangle$ states. This effect, which arises from the difference in the Landé g-factor for atoms in $|g\rangle$ and in $|e\rangle$, is explained and characterized in detail for ^{171}Yb in Section 3.4. The resulting interaction Hamiltonian in the $\{|eg^+\rangle, |eg^-\rangle\}$ basis is [73]

$$
\hat{H} = \begin{pmatrix} U_{eg}^+ & \delta(B) \\ \delta(B) & U_{eg}^- \end{pmatrix},
\tag{2.18}
$$

where $\delta(B) = h \times 399.0(1)\,\text{Hz} \times B/2$ is the differential Zeeman shift measured in Section 3.4. Diagonalization of the interaction Hamiltonian in Eq. (2.18) in this basis leads to the eigenenergies

$$
E_\pm(B) = V \pm V_{ex} \sqrt{1 + \left[\frac{\delta(B)}{V_{ex}}\right]^2},
\tag{2.19}
$$

defining the spin-exchange interaction energy

$$
V_{ex} = \frac{U_{eg}^+ - U_{eg}^-}{2}
\tag{2.20}
$$

and direct interaction energy

$$
V = \frac{U_{eg}^+ + U_{eg}^-}{2}.
\tag{2.21}
$$

The energy branches resulting from Eq. (2.19) are shown in Fig. 4.3 for ^{171}Yb atoms probed using interaction spectroscopy measurements in a deep optical lattice. In Section 4.2, we use the obtained energy branches to extract the interaction energies $U_{eg}^\pm$ in a first step and finally the fundamental interorbital scattering lengths $a_{eg}^\pm$ in ^{171}Yb in a second step.

The eigenstates corresponding to $E_\pm(B)$ are given by

$$
\begin{aligned}
|\psi_{\text{eg}}^+\rangle &= -\frac{[V_{\text{ex}} + c(B)]}{\sqrt{2}\sqrt{\delta(B)^2 + V_{\text{ex}}^2 + V_{\text{ex}}c(B)}}|eg^+\rangle + \frac{\delta(B)}{\sqrt{2}\sqrt{\delta(B)^2 + V_{\text{ex}}^2 + V_{\text{ex}}c(B)}}|eg^-\rangle, \\
|\psi_{\text{eg}}^-\rangle &= -\frac{[V_{\text{ex}} - c(B)]}{\sqrt{2}\sqrt{\delta(B)^2 + V_{\text{ex}}^2 - V_{\text{ex}}c(B)}}|eg^+\rangle + \frac{\delta(B)}{\sqrt{2}\sqrt{\delta(B)^2 + V_{\text{ex}}^2 - V_{\text{ex}}c(B)}}|eg^-\rangle,
\end{aligned} \tag{2.22}
$$

with $c(B) = \sqrt{\delta(B)^2 + V_{\text{ex}}^2}$. In the limit of large magnetic fields where $\delta(B) \gg V_{\text{ex}}$, the eigenstates of the interaction Hamiltonian in Eq. (2.18) become

$$
\begin{aligned}
|\psi_{\text{eg}}^+\rangle &\rightarrow |eg\uparrow\downarrow\rangle = \frac{1}{\sqrt{2}}\left(|eg^-\rangle - |eg^+\rangle\right) = \frac{1}{\sqrt{2}}\left(|e\uparrow\rangle|g\downarrow\rangle - |g\downarrow\rangle|e\uparrow\rangle\right) \\
|\psi_{\text{eg}}^-\rangle &\rightarrow |eg\downarrow\uparrow\rangle = \frac{1}{\sqrt{2}}\left(|eg^-\rangle + |eg^+\rangle\right) = \frac{1}{\sqrt{2}}\left(|e\downarrow\rangle|g\uparrow\rangle - |g\uparrow\rangle|e\downarrow\rangle\right),
\end{aligned} \tag{2.23}
$$

with eigenenergies given by $E_\pm(B) \approx V \pm \text{sgn}(V_{\text{ex}})|\delta(B)|$, where $\text{sgn}(V_{\text{ex}})$ denotes the sign of the spin-exchange interaction energy V_{ex}.

2.2.4   Orbital Feshbach resonances

Magnetic Feshbach resonances [33] occuring in alkali atoms are an essential tool in cold atoms experiments since they enable full control over the scattering length a between atoms in the sample by simply tuning an external magnetic field. In particular, the strongly interacting regime where $|a|$ becomes very large can be explored in the vicinity of a Feshbach resonance [11].

In a simple picture, we consider two cold atoms colliding with very small energy E and featuring two interaction channels, an energetically accessible open channel $|o\rangle$ and an energetically inaccessible closed channel $|c\rangle$ with corresponding molecular potentials $V_o(r)$ and $V_c(r)$. A Feshbach resonance occurs if both interaction channels are coupled and if the least-bound state supported by the closed-channel molecular potential approaches the open-channel entrance energy at long interparticle distances r. This is generally achieved by using an external magnetic field B. Around a magnetically tuned Feshbach resonance, the s-wave scattering length describing the interactions between both atoms takes the form [33]

$$
a(B) = a_{\text{bg}}\left(1 - \frac{\Delta}{B - B_0}\right), \tag{2.24}
$$

where B_0 is the resonance position, Δ the resonance width and a_{bg} the background scattering length.

In alkali atoms with electronic ground state $^2S_{1/2}$, two interaction channels corresponding to a spin singlet or triplet are available for the scattering process. At large magnetic fields B, the relative energy between both channels varies linearly in B with a magnetic moment about $-2\mu_B \approx -2.8\,\text{MHz/G}$ [33]. This leads to a Feshbach resonance occurring at the magnetic field B_0 where the closed-channel bound state is brought into resonance with the energy of the incoming atoms, as illustrated in Fig. 2.3(a).
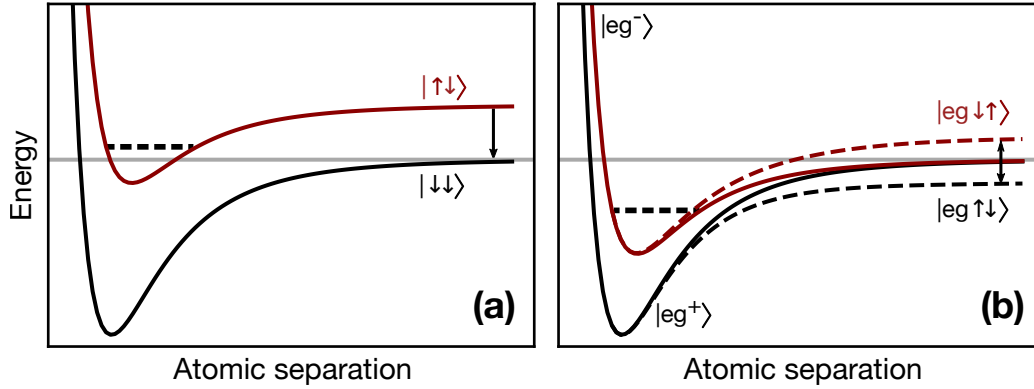
Figure 2.3 – **Feshbach resonance mechanisms.** The magnetic field dependence of the open- (solid black lines) and closed-channel (solid red lines) interatomic molecular interaction potentials is shown in **(a)** usual magnetic Feshbach resonances in alkali atoms and **(b)** orbital Feshbach resonances in alkaline-earth(-like) atoms. In the case of magnetic Feshbach resonances, the open scattering channel corresponds to the spin singlet state while the closed channel corresponds to the triplet state. The relative energy between both channels can be tuned with an external magnetic field with a slope $-2\mu_B \approx -2.8\,\mathrm{MHz/G}$, where μ_B denotes the Bohr magneton. When the energy of the least-bound state supported by the closed channel (horizontal dashed black line) is equal to the entrance energy of the open channel, a Feshbach resonance occurs and the scattering length diverges. In the case of an orbital Feshbach resonance, the entrance energy of the open channel $|o\rangle = |eg \uparrow\downarrow\rangle$ is tuned to enter in resonance with least-bound state $|b_c\rangle$ supported by the closed channel $|c\rangle = |eg \downarrow\uparrow\rangle$. This is achieved by using the differential Zeeman shift, which induces a small differential magnetic moment $h \times 399.0\,(1)\,\mathrm{Hz/G}$ between both channels.

The situation is different in alkaline-earth(-like) atoms such as ytterbium, which feature a ground state $^1\mathrm{S}_0$ with $J = 0$. As already mentioned in Section 2.1, the zero total electronic angular momentum leads to a strong decoupling between J and I implying a single scattering channel for all collisions between two atoms in the same electronic state. Therefore, no magnetic Feshbach resonance is expected to occur in the $^1\mathrm{S}_0$ and $^3\mathrm{P}_0$ states in Yb. However, the situation is different when considering scattering between one $^1\mathrm{S}_0$ atom and one $^3\mathrm{P}_0$ atom. Here, two interorbital interaction channels $|o\rangle$ and $|c\rangle$ exist. At large atomic separations and finite magnetic fields, they are given by the eigenstates of the Zeeman Hamiltonian $|eg \uparrow\downarrow\rangle$ and $|eg \downarrow\uparrow\rangle$ defined in Eq. (2.23), respectively, since the atoms are non-interacting ($U^{\pm}_{\mathrm{eg}} \to 0$). Here, the differential Zeeman shift introduced in Section 2.2.3 shifts down the entrance energy of the open channel $|o\rangle$ while shifting up the entrance energy of the closed channel $|c\rangle$. This induces a differential magnetic moment $\delta\mu = h \times 399.0\,(1)\,\mathrm{Hz/G}$ between both scattering channels.

At small atomic separations, interactions become dominant over the Zeeman shift, and the open and closed channels are given by $|eg^+\rangle$ and $|eg^-\rangle$, respectively. The interaction part of the Hamiltonian describing the scattering process can therefore be expressed using a regularized

pseudopotential [103]

$$\hat{V} = \frac{4\pi\hbar^2}{m}\left(a_{\mathrm{eg}}^+ |eg^+\rangle\langle eg^+| + a_{\mathrm{eg}}^- |eg^-\rangle\langle eg^-|\right)\delta^{(3)}(\mathbf{r})\frac{\partial}{\partial r}r, \tag{2.25}$$

where m denotes the atomic mass. This yields in the $\{|o\rangle, |c\rangle\}$ basis [103]

$$\hat{V} = \hat{V}_{\mathrm{d}}\left(|o\rangle\langle o| + |c\rangle\langle c|\right) + \hat{V}_{\mathrm{ex}}\left(|c\rangle\langle o| + |o\rangle\langle c|\right), \tag{2.26}$$

with $V_\alpha = \left(4\pi\hbar^2/m\right)a_\alpha\delta^{(3)}(\mathbf{r})(\partial/\partial r)r$. Here we have defined $a_{\mathrm{d}} = \left(a_{\mathrm{eg}}^+ + a_{\mathrm{eg}}^-\right)/2$ and $a_{\mathrm{ex}} = \left(a_{\mathrm{eg}}^- - a_{\mathrm{eg}}^+\right)/2$. The second term in Eq. (2.26) describes interorbital spin exchange and effectively couples both interorbital scattering channels $|o\rangle$ and $|c\rangle$. For $a_{\mathrm{d}} > 0$, a bound state supported by the molecular potential of the closed channel always exists, with binding energy

$$\epsilon_{\mathrm{b}} = -\frac{\hbar^2}{ma_{\mathrm{d}}^2}. \tag{2.27}$$

From the above, it appears that all requirements for a Feshbach resonance are fulfilled, yielding a so-called orbital Feshbach resonance [103] such as illustrated in Fig. 2.3(b), which has first been observed in ^{173}Yb [105, 106]. In Chapter 5, we report on the first experimental observation of an orbital Feshbach resonance in ^{171}Yb.

The open-channel scattering length is determined by solving the Schrödinger equation for the full Hamiltonian $\hat{H} = \hat{H}_0 + \hat{V}$ including the non-interacting Hamiltonian $\hat{H}_0$ and is given by [103]

$$a(B) = \frac{-a_{\mathrm{d}} + \sqrt{m\delta(B)/\hbar^2}\left(a_{\mathrm{d}}^2 - a_{\mathrm{ex}}^2\right)}{a_{\mathrm{d}}\sqrt{m\delta(B)/\hbar^2} - 1}, \tag{2.28}$$

with the differential Zeeman shift $\delta(B)/h = B \times 399.0(1)$ Hz for ^{171}Yb. Using the interorbital scattering lengths determined in Section 4.2 for ^{171}Yb, $a(B)$ such as described by Eq. (2.28) diverges at a magnetic field $B \approx 536$ G corresponding to the expected position of the orbital Feshbach resonance in this isotope. As reported in Chapter 5, we find the resonance to occur at a much larger magnetic field $B \approx 1300$ G. We explain this discrepancy by the very large Zeeman shift on resonance, making the scattering amplitude highly sensitive to finite-range effects which are not considered in Eq. (2.28).

Finally, we introduce the dimensionless resonance strength parameter, which is defined as [33]

$$s_{\mathrm{res}} = \frac{a_{\mathrm{bg}}}{\bar{a}}\frac{\delta\mu\Delta}{\bar{E}}, \tag{2.29}$$

with the resonance width Δ, background scattering length a_{bg} and differential magnetic moment $\delta\mu$. The mean scattering length $\bar{a}$ and mean energy $\bar{E}$ are defined in Eqs. (2.12) and (2.14), respectively. This parameter allows to classify Feshbach resonances into narrow (or closed-channel dominated) resonances for $s_{\mathrm{res}} \ll 1$ and broad (or open channel dominated) resonances for $s_{\mathrm{res}} \gg 1$. Owing to the very small differential magnetic moments $\delta\mu$ involved in orbital Feshbach resonances compared to the situation in magnetic Feshbach resonances, these can be classified as very narrow despite featuring widths $\Delta \sim 100$ G.

2.3   Two-orbital Fermi-Hubbard models

Optical lattices are an important tool for the study of many-body physics [9, 11, 12, 14] since they realize periodic potential landscapes for ultracold atomic ensembles. Fermions in optical lattices mimic the behavior of electrons in a crystal and allow for the quantum simulation of the Fermi-Hubbard model. In alkaline-earth(-like) atoms, this Fermi-Hubbard model can be generalized to feature two orbitals and $SU(N)$ symmetry. Furthermore, optical lattices are a key ingredient for precision spectroscopy measurements since they quantize the atomic motion, see Section 3.3.2 for a detailed discussion. All the measurements reported in this work have therefore been performed in an optical lattice.

2.3.1   Optical lattices

In cold atoms experiments, optical lattices are conveniently generated by interfering one or multiple laser beams. A simple experimental implementation is to use a single retro-reflected beam interfering with itself. In this case, the resulting potential is given by

$$V(\mathbf{r}) = \sum_{i=\{x,y,z\}} -V_{0,i}\sin^2(kr_i),$$
(2.30)

where the inhomogeneous intensity profile of the laser generating the lattice potential is neglected[1]. The potential along the axis i has a periodicity of $\lambda_i/2$, where λ_i denotes the wavelength of the lattice laser along i. The lattice depth $V_{0,i}$ is proportional to the intensity I_0 of the lattice laser and is usually given in units of the lattice photon recoil energy $E_{\mathrm{rec}} = \hbar^2 k_i^2/2m$, with wave vector $k_i = 2\pi/\lambda_i$ and atomic mass m.

Along a single lattice axis x, the non-interacting single-particle Hamiltonian for an atom in an optical lattice is given by

$$\hat{H}_0 = -\frac{\hbar^2\nabla^2}{2m} + V(x).$$
(2.31)

Since the potential is spatially periodic, the solutions of the Schrödinger equation satisfy the Bloch theorem and take the form

$$\phi_{q,n}(x) = e^{iqx/\hbar}u_{q,n}(x),$$
(2.32)

where q is the lattice momentum, n the lattice band, and $u_{q,n}(x)$ a function with the same periodicity as the lattice. Expanding $u_{q,n}(x)$ as a discrete Fourier sum

$$u_{q,n}(x) = \sum_l c_{q,n}^l e^{i2lkx}$$
(2.33)

and inserting Eq. (2.33) into the Schrödinger equation yields the eigenenergy spectrum, which can be obtained via numerical diagonalization [146].

---

[1]In Section 3.3.4, we show that the lattice inhomogeneity needs to be taken into account for certain applications.

An important alternative orthonormal set of functions describing atoms in a lattice are the so-called Wannier functions, which are defined as

$$w_{n,j}(x) = w_n(x - x_j) = \int_{-\pi/a}^{\pi/a} \frac{dq}{2\pi} \phi_{q,n}(x) e^{-iqx_j} \tag{2.34}$$

on the lattice site j. These functions are localized around the lattice potential minima and form a natural basis to describe on-site interactions and nearest-neighbor tunneling in deep lattices.

In second quantization, the non-interacting Hamiltonian in Eq. (2.31) takes the form

$$\hat{H}_0 = \int dx \hat{\Psi}^\dagger(x) \left[-\frac{\hbar^2 \nabla^2}{2m} + V(x) \right] \hat{\Psi}(x), \tag{2.35}$$

with the field operators $\hat{\Psi}(x) = \sum_{n,i} w_{n,i}^*(x) \hat{a}_{n,i}$ expanded in terms of the Wannier function and annihilation operator $\hat{a}_{n,i}$ on each lattice site i and band n. Limiting the problem to nearest-neighbor tunneling yields the tight-binding Hamiltonian

$$\hat{H}_0 \approx -t \sum_{\langle i,j \rangle} \left(\hat{a}_i^\dagger \hat{a}_j + \text{h.c.} \right), \tag{2.36}$$

defining the tunneling matrix element

$$t = -\int dx\, w_n(x - x_i) \left[-\frac{\hbar^2 \nabla^2}{2m} + V(x) \right] w_n^*(x - x_i) \tag{2.37}$$

which can be computed numerically. In Section 2.4, the interaction part of the Hamiltonian is derived, see Eq. (2.48). Summing both contributions and taking into account the spin σ of the atoms leads to the Fermi-Hubbard Hamiltonian

$$\hat{H} = -t \sum_{\langle i,j \rangle, \sigma} \left(\hat{a}_{i,\sigma}^\dagger \hat{a}_{j,\sigma} + \text{h.c.} \right) + \frac{U}{2} \sum_{i, \sigma \neq \sigma'} \hat{n}_{i,\sigma} \hat{n}_{i,\sigma'}, \tag{2.38}$$

where $\hat{n}_{i,\sigma} = \hat{a}_{i,\sigma}^\dagger \hat{a}_{i,\sigma}$ is the number operator.

Finally, we note that in the limit of deep lattices, the on-site trapping potential experienced by an atom can be approximated with an harmonic potential. Expanding the potential $V(x)$ around $x = 0$ yields the corresponding harmonic oscillator frequency

$$\omega_{\text{ho}} = \frac{2\sqrt{s}}{\hbar} E_{\text{rec}} \tag{2.39}$$

and harmonic oscillator length

$$a_{\text{ho}} = \sqrt{\frac{\hbar}{m\omega_{\text{ho}}}}, \tag{2.40}$$

where s denotes the lattice depth V_0 in units of E_{rec}. Expanding the lattice potential up to next-to-leading order x^4 leads to a modified ground band ($n = 0$) energy

$$E_0 = \left(2\sqrt{s} - \frac{1}{4} \right) E_{\text{rec}} \tag{2.41}$$

containing the first energy correction $-E_{\text{rec}}/4$ arising from the lattice anharmonicity. This correction is independent of the lattice depth s.

2.3.2 Two-orbital Fermi-Hubbard Hamiltonian

The Fermi-Hubbard Hamiltonian introduced in Eq. (2.38) can be generalized to the case of two electronic orbitals $\alpha = \{g, e\}$ and $SU(N)$-symmetric interactions. The resulting two-orbital Fermi-Hubbard Hamiltonian is given by [69]

$$
\hat{H} = - \sum_{\langle i,j \rangle, \alpha, \sigma} t_\alpha \left(\hat{a}^\dagger_{i,\alpha,\sigma} \hat{a}_{j,\alpha,\sigma} + \text{h.c.} \right) + \sum_{i, \alpha, \sigma \neq \sigma'} \frac{U_{\alpha\alpha}}{2} \hat{n}_{i,\alpha,\sigma} \hat{n}_{i,\alpha,\sigma'}
$$
$$
+ V \sum_i \hat{n}_{i,e} \hat{n}_{i,g} + V_{\text{ex}} \sum_{i, \sigma, \sigma'} \hat{a}^\dagger_{i,g,\sigma} \hat{a}^\dagger_{i,e,\sigma'} \hat{a}_{i,e,\sigma'} \hat{a}_{i,g,\sigma},
$$

(2.42)

with the direct and spin exchange interaction energies V and V_{ex} defined in Eqs. (2.21) and (2.20), respectively. The on-site interaction energies $U_{\alpha\alpha}$ are obtained from the fundamental s-wave scattering lengths $a_{\alpha\alpha}$ using one of the methods discussed in Section 2.4. The first line in Eq. (2.42) is similar to the single-band Fermi-Hubbard Hamiltonian in Eq. (2.38) in the g and e orbitals. The second line, however, couples both orbitals and gives rise to two additional terms. While the first term represents the direct interorbital on-site interactions, the second term describes on-site spin-exchanging interactions. The ratio of the tunneling matrix element t_e to t_g can be readily tuned via the wavelength of the lattice laser, see Fig. 2.2, enabling the use of so-called state-dependent lattices [75].

The two-orbital Hamiltonian in Eq. (2.42) is very general. By careful choice of the experimental parameters, particular two-orbital models of interest can be engineered. In the next sections, two examples of such models are introduced.

2.3.3 Kondo lattice model

The Kondo lattice model [147] describes in solid state physics the spin-exchange interactions between mobile conduction electrons and strongly localized spins. It is the generalization of the Kondo impurity model to a unit-filled lattice of localized magnetic impurities.

Starting from the general Hamiltonian in Eq. (2.42), one can set the lattice wavelength such that $|e\rangle$ atoms are strongly localized with $t_e \approx 0$ and $n_{i,e} \approx 1$ while keeping the $|g\rangle$ atoms mobile. Furthermore neglecting the direct interaction term which corresponds to a constant energy offset and assuming $U_{gg} \approx 0$, the general Hamiltonian reduces to [69]

$$
\hat{H}_{\text{KLM}} = -t_g \sum_{\langle i,j \rangle, \sigma} \left(\hat{a}^\dagger_{i,g,\sigma} \hat{a}_{j,g,\sigma} + \text{h.c.} \right) + V_{\text{ex}} \sum_{i, \sigma, \sigma'} \hat{a}^\dagger_{i,g,\sigma} \hat{a}^\dagger_{i,e,\sigma'} \hat{a}_{i,e,\sigma'} \hat{a}_{i,g,\sigma},
$$

(2.43)

which corresponds to the Kondo lattice model Hamiltonian. In ^{171}Yb, the very small s-wave scattering length $a_{gg} \approx 0$ in the ground state makes $U_{gg} \approx 0$ a good approximation. In contrast, a very shallow lattice for $|g\rangle$ atoms needs to be used in ^{173}Yb in order to fulfill this condition.

The properties of the Kondo lattice model strongly depend on the sign of the spin exchange interaction energy V_{ex}. In ^{173}Yb, $V_{\text{ex}} > 0$, corresponding to ferromagnetic spin exchange interactions [73]. This situation favors the formation of spin-triplet states between mobile conduction fermions and localized spins and is relevant for example in the context of colossal

magnetoresistance [66, 67]. In ^{171}Yb, the interorbital scattering lengths determined in Section 4.2 imply $V_{ex} < 0$, corresponding to antiferromagnetic spin exchange interactions. This situation favors the formation of spin-singlet states between mobile and localized spins and describes for instance heavy-Fermion behavior in metals [64, 98]. In the single-impurity limit, the antiferromagnetic spin-exchange interaction gives rise to the Kondo effect [63] describing the resistance minimum with temperature in metals with magnetic impurities [148].

2.3.4   Mass-imbalanced Fermi-Hubbard model

A second example of a model that can be derived from Eq. (2.42) is the mass-imbalanced Fermi-Hubbard model with tunable interactions. In the presence of an external magnetic field B, the differential Zeeman shift discussed in Section 3.4 strongly suppresses the spin-exchange interactions and allows to tune interorbital interactions $U_{eg}(B)$ using an orbital Feshbach resonance. If atoms are prepared in the single-particle states $|e\rangle \equiv |e\uparrow\rangle$ and $|g\rangle \equiv |g\downarrow\rangle$ corresponding to the open interaction channel in ^{171}Yb, the Hamiltonian in Eq. (2.42) becomes

$$\hat{H}_{\mathrm{LH}} = -\sum_{\langle i,j \rangle} t_\alpha \left(\hat{a}_{i,\alpha}^\dagger \hat{a}_{j,\alpha} + \mathrm{h.c.} \right) + U_{eg}(B) \sum_i \hat{n}_{ig} \hat{n}_{ie}, \tag{2.44}$$

where the ratio between t_e and t_g corresponding to a mass imbalance between $|g\rangle$ and $|e\rangle$ atoms can be tuned with the lattice laser wavelength. In ^{171}Yb we furthermore have $U_{gg} \approx 0$. In a recent experiment [119], transport properties in the one-dimensional mass-imbalnced Fermi-Hubbard model have been investigated using ^{171}Yb atoms. In this measurement, the orbital Feshbach resonance in ^{171}Yb reported in Chapter 5 has played a central role.

2.4   On-site interaction models

  Most measurements performed in this work consist in spectroscopically probing the interactions between two ytterbium atoms subjected to various experimental conditions. The obtained interaction energies, however, depend on these conditions such as the trapping potential. In order to extract more universal quantities from our measurements such as s-wave scattering lengths, suitable models for the interaction energy need to be used together with a careful characterization of the experimental conditions.

    In this section, two models which are extensively used in the following chapters to compute the interaction energies of two ultracold atoms on a single lattice site are described.

2.4.1   Wannier functions overlap

In a first approach, the Hubbard on-site interaction energy corresponding to two indistinguishable atoms interacting in an optical lattice via a point-like pseudo-potential is used. Here, we consider the general expression for the interaction Hamiltonian

$$\hat{H}_{\mathrm{int}} = \frac{1}{2} \int d\mathbf{r}\, \hat{\Psi}^\dagger(\mathbf{r}) \hat{\Psi}^\dagger(\mathbf{r}') \hat{U}(\mathbf{r}-\mathbf{r}') \hat{\Psi}(\mathbf{r}') \hat{\Psi}(\mathbf{r}) \tag{2.45}$$

in second quantization. The field operator $\hat{\Psi}(\mathbf{r})$ can be expanded in terms of the corresponding atomic wavefunction, leading to

$$\hat{\Psi}(\mathbf{r}) = \sum_i \hat{a}_i \psi_i(\mathbf{r}), \tag{2.46}$$

where $\hat{a}_i$ is the annihilation operator for an atom and $\psi_i(\mathbf{r})$ the atomic wavefunction, both defined on a lattice site i. On the other hand, the interaction operator $\hat{U}(\mathbf{r})$ is given by the pseudo-potential

$$\hat{U}(\mathbf{r}) = \frac{4\pi\hbar^2 a}{m} \delta^{(3)}(\mathbf{r}), \tag{2.47}$$

where m denotes the atomic mass and a the s-wave scattering length defining the interaction between the atoms. Inserting Eqs. (2.46) and (2.47) into Eq. (2.45) yields

$$\hat{H}_{\text{int}} = \frac{U}{2} \sum_i \hat{n}_i (\hat{n}_i - 1), \tag{2.48}$$

defining the number operator $\hat{n}_i = \hat{a}_i^\dagger \hat{a}_i$ and the Hubbard on-site interaction energy

$$U = \frac{4\pi\hbar^2 a}{m} \prod_{i=\{x,y,z\}} \left(\int dr \, |\psi_i(r)|^4 \right), \tag{2.49}$$

where we have assumed two identical particles with separable wavefunction $\psi(\mathbf{r}) = \psi_x(x)\psi_y(y)\psi_z(z)$ along each spatial axis. Equation (2.49) is very general since it does not explicitly take into account the specific potential the atoms undergo but only contains the overlap of the atomic spatial wavefunctions. The external potential is indirectly taken into account when making a particular choice for the wavefunction. In a cubic optical lattice, the simplest choice is to assume both wavefunctions to be given by the ground-band Wannier function $|w_{0,i}(r)|$ corresponding to a given lattice depth and wavelength along each lattice axis i, leading to

$$U = \frac{4\pi\hbar^2 a}{m} \prod_{i=\{x,y,z\}} \left(\int dr \, |w_{0,i}(r)|^4 \right). \tag{2.50}$$

Equation (2.50) is only valid in the limit of small scattering lengths a and deep lattices, where contributions from higher lattice bands are negligible. In general, these contributions reduce the interaction energy U. If U is experimentally determined as in the measurements reported in the following chapters, the corresponding s-wave scattering length a is therefore underestimated when computing the interaction energy with Eq (2.50).

On-site inelastic scattering

In addition to the elastic on-site interactions described above, inelastic scattering occurs between atomic pairs, leading to a loss of these atoms. This is particularly relevant in the case of atomic pairs in the electronic clock state $^3P_0$ which show strong inelastic scattering as demonstrated in Section 4.5. The on-site pair lifetime $\tau_{XX'}$, where X and X' denote the electronic

states of both atoms, can be obtained via [149]

$$(\tau_{XX'})^{-1} = 2\beta_{XX'} \int \mathrm{d}^3\mathbf{r} \, |w_X(\mathbf{r})|^2 \, |w_{X'}(\mathbf{r})|^2, \tag{2.51}$$

assuming that both atoms are in the ground lattice band. Here, $\beta_{XX'}$ defines the two-body loss-rate coefficient for atomic pairs in X and X'. In Chapter 4, we characterize the two-body loss-rate coefficient of interorbital pairs as well as of clock-state pairs in ^{171}Yb.

2.4.2 Two ultracold atoms in a harmonic trap

A second approach to model interatomic interactions is to consider the exactly-solvable problem of two ultracold atoms in an isotropic harmonic trap interacting via a regularized contact potential [150]. The Hamiltonian describing the motion of both atoms takes the general form

$$\hat{H} = -\frac{\hbar^2}{2m}\nabla_1^2 - \frac{\hbar^2}{2m}\nabla_2^2 + \frac{1}{2}m\omega^2\mathbf{r}_1^2 + \frac{1}{2}m\omega^2\mathbf{r}_2^2 + \frac{4\pi\hbar^2 a}{m}\delta_{\mathrm{reg}}^{(3)}(\mathbf{r}_1 - \mathbf{r}_2), \tag{2.52}$$

where m is the atomic mass, ω the harmonic oscillator frequency of the trap and $\delta_{\mathrm{reg}}^{(3)}(\mathbf{r}) = \delta^{(3)}(\mathbf{r})(\partial/\partial r)r$ the regularized Dirac delta function [151]. Since the kinetic and potential energy parts of the Hamiltonian are quadratic, the problem can be separated into center-of-mass and relative motion. While the center-of-mass part of the problem leads to the usual harmonic oscillator solutions for the Schrödinger equation, the solutions for the relative motion are obtained by considering a wavefunction of the form

$$\psi(\mathbf{r}) = \sum_{n=0}^{\infty} c_n \varphi_n(\mathbf{r}), \tag{2.53}$$

where $\varphi_n(\mathbf{r})$ denotes the harmonic oscillator wavefunction in state n. The resulting eigenergies E are defined by [150]

$$\sqrt{2}\frac{\Gamma(-E/2\hbar\omega + 3/4)}{\Gamma(-E/2\hbar\omega + 1/4)} = \frac{a_{\mathrm{ho}}}{a}, \tag{2.54}$$

where a_{ho} is the harmonic oscillator length defined in Eq. (2.40) and $\Gamma(x)$ denotes the Gamma function. The left-hand side of Eq. (2.54) vanishes for $E = (1/2 + 2n)\hbar\omega$. On the other hand, it diverges for the unperturbed oscillator levels $E = (3/2 + 2n)\hbar\omega$ corresponding to the non-interacting case with $a = 0$.

In Fig. 2.4, the energy branches obtained from Eq. (2.54) are shown both as a function of the scattering length a [Fig. 2.4(a)] and as a function of the inverse scattering length $1/a$ [Fig. 2.4(b)]. In the measurement of the intra- and interorbital scattering lengths in ^{171}Yb reported in Chapter 4, the second-lowest-lying energy branch shown in Fig. 2.4(a) is used to extract the scattering lengths from the measured on-site interaction energies. On the other hand, both lowest-lying branches shown in Fig. 2.4(b) are probed in Chapter 5 to observe and characterize the OFR in ^{171}Yb.

In the limit of very deep lattices, Eq. (2.54) is a good model to describe on-site interactions using the harmonic oscillator frequency defined in Eq. (2.39). However, at finite lattice
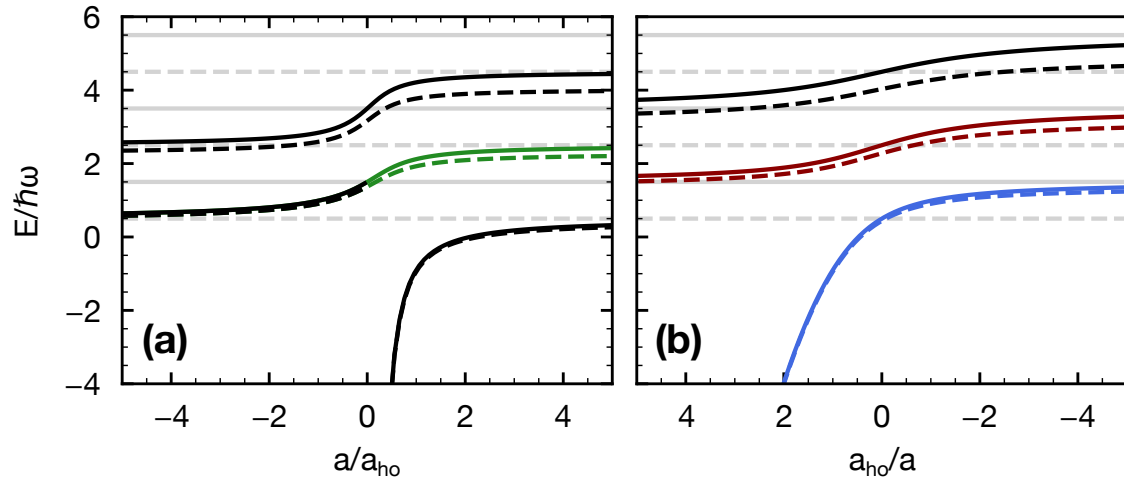
Figure 2.4 – **Exact energy solutions for two ultracold atoms in an harmonic trap.** We show the three lowest-lying energy branches solving Eq. (2.54) as a function of the **(a)** scattering length a and **(b)** inverse scattering length $1/a$. The energies are represented in units of the harmonic oscillator level spacing $\hbar\omega$ while the scattering length is given in units of the harmonic oscillator length a_ho. Solid (dashed) horizontal gray lines denote poles (zeroes) of the left hand side in Eq. (2.54). The green branch in (a) is used for the extraction of the s-wave scattering lengths from the measured on-site interaction energies in Chapter 4. On the other hand, the blue and red branches in (b) are probed in Chapter 5 to characterize the OFR in ^{171}Yb. When comparing these energies with our experimental data, the zero-point energy $3\hbar\omega/2$ is first removed. The uncorrected energy branches are shown as solid lines while the energy branches corrected for the anharmonicity in a $30\,E_\mathrm{rec}$ optical lattice are shown as dashed lines.

depths, the lattice potential anharmonicity plays a significant role and needs to be taken into consideration in the calculation of the on-site interaction energies. We do this by means of first-order perturbation theory, expanding the lattice potential up to 8th order. The corrected energies for a $30\,E_\mathrm{rec}$ deep isotropic lattice are shown as dashed lines in Fig. 2.4.

Experimental methods

The experiments presented in this thesis are performed on quantum degenerate gases of ^{171}Yb atoms trapped in optical lattices. Complex experimental techniques are required to allow for the reproducible production, manipulation and detection of samples. In this chapter, we review the experimental methods used in the frame of this thesis. First, the production of ultracold ytterbium gases is described, including an overview of our experimental setup and cooling techniques. After that, all relevant methods for sample preparation and detection are introduced, addressing both the electronic and the nuclear spin degrees of freedom. In particular, clock-line spectroscopy in a state-independent optical lattice is discussed in detail since it plays a central part in all experiments presented in the following chapters. Finally, a measurement of the differential and quadratic Zeeman shifts on the clock transition in ^{171}Yb is reported as these atomic properties play an important role in the experiments presented in this thesis.

3.1   Preparation of degenerate Fermi gases of ytterbium

The first step of our experiments is always the production of ultracold ^{171}Yb quantum-degenerate gases in a dipole trap. In this section, an overview of our experimental setup is given along with a description of the cooling procedure, where atoms initially trapped in a magneto-optical trap (MOT) are subsequently cooled by means of forced evaporative cooling. The implementation is more complex with ^{171}Yb than with the other fermionic isotope, ^{173}Yb. This is due to the almost vanishing s-wave scattering length in the ground state, which hinders efficient forced evaporative cooling and requires sympathetic cooling with another isotope, which we have chosen to be ^{174}Yb.

3.1.1   Experimental setup overview

Our experimental apparatus, which has been running for multiple years now, has undergone numerous improvements over time and is currently in a mature stage where significant technical changes are made at a rather slower pace. The experimental setup is therefore only briefly discussed in the following, with a focus on recent upgrades. For further technical details about the setup, we refer to previous thesis works [142, 152–155].

A schematic illustration of the experimental setup used in this thesis is shown in Fig. 3.1. It consists of an ultrahigh vacuum system surrounded by multiple coils to generate magnetic fields and numerous laser beams to address the atoms. The main part of the setup is an octagonal stainless steel chamber with a background pressure around 10^{-11} mbar in which the atoms are trapped and manipulated. In such an ultra-high vacuum, our degenerate Fermi gases have a very long lifetime over 100 s. The chamber features eight CF40 and two CF100 flange connections to ensure optimal optical access to the atoms. The atomic source is an oven heated up to 400 °C and filled with small pieces of nearly-pure ytterbium metal containing all isotopes with their natural abundance. Atoms exit the oven through a collimation section and form an atomic beam with an average longitudinal thermal velocity about 340 m/s.

The longitudinal atomic velocity is reduced by a Zeeman slower consisting of a counter-propagating laser beam (ZS) addressing the broad $^1S_0 \rightarrow {}^1P_1$ line and of a coil (C_{ZS}) generating a spatially-dependent magnetic field. The atoms are subsequently cooled and trapped in the center of the main chamber in a MOT operating on the narrow 556 nm $^1S_0 \rightarrow {}^3P_1$ intercombination line. The trapping potential is generated by two pairs of coils running in anti-Helmholtz configuration, the transverse (C_{TV}) and MOT (C_{MOT}) coils. Laser cooling in all spatial dimensions is provided by six MOT beams, with a remarkably low Doppler temperature $T_D = 4.4\,\mu K$ arising from the narrow linewidth 182 kHz of the transition. In Helmholtz configuration, the transverse coils produce a maximal horizontal magnetic field $B_{TV} = 25$ G at the position of the atoms. The MOT coils, on the other hand, have been designed to withstand large currents and we have generated vertical magnetic fields up to $B_z = 1650$ G using them.

After cooling in the MOT, atoms are transferred into a far-off-resonant crossed optical dipole trap (xODT) consisting of two high-power 1064 nm horizontal (HDT) and vertical (VDT) laser beams, in which forced evaporative cooling is performed to reach quantum degeneracy. Two 759 nm laser beams propagating horizontally (mHDT) and vertically (mVDT) are employed as additional optical dipole traps, presenting the advantage of operating at the magic wavelength of the clock transition (see Section 3.3.3) such that both electronic states $^1S_0$ and $^3P_0$ experience the same trapping potential. A set of three perpendicular retro-reflected 759 nm beams (L_1, L_2 and L_3) generates a cubic magic-wavelength optical lattice with a maximal average depth about $40\,E_{rec}$, where E_{rec} denotes the lattice photon recoil energy, in which the atoms are finally loaded to perform our experiments.

The electronic state of the atoms is manipulated with resonant 578 nm light addressing the clock transition. Three clock-laser beam paths are employed, each of them aligned with one lattice axis (clock L_1, clock L_2 and clock L_3) to operate in the Lamb-Dicke regime (see Section 3.3.2).

Two 399 nm beams are used for absorption imaging of the sample (see Section 3.2.2). A first horizontal beam (img hor) enables time-of-flight imaging from the side after free expansion from the trap, and is recorded on a CCD camera with low magnification (3.9 μm/px). A second vertical beam (img ver) is dedicated to high-resolution in-situ imaging in the trap and is recorded on an EMCCD camera with a magnification of 0.47 μm/px. In addition, a 1389 nm repumper laser allows for separate imaging of $^1S_0$ and $^3P_0$ atoms (see Section 3.2.2) and a 556 nm optical Stern-Gerlach (OSG) beam enables nuclear spin state detection after
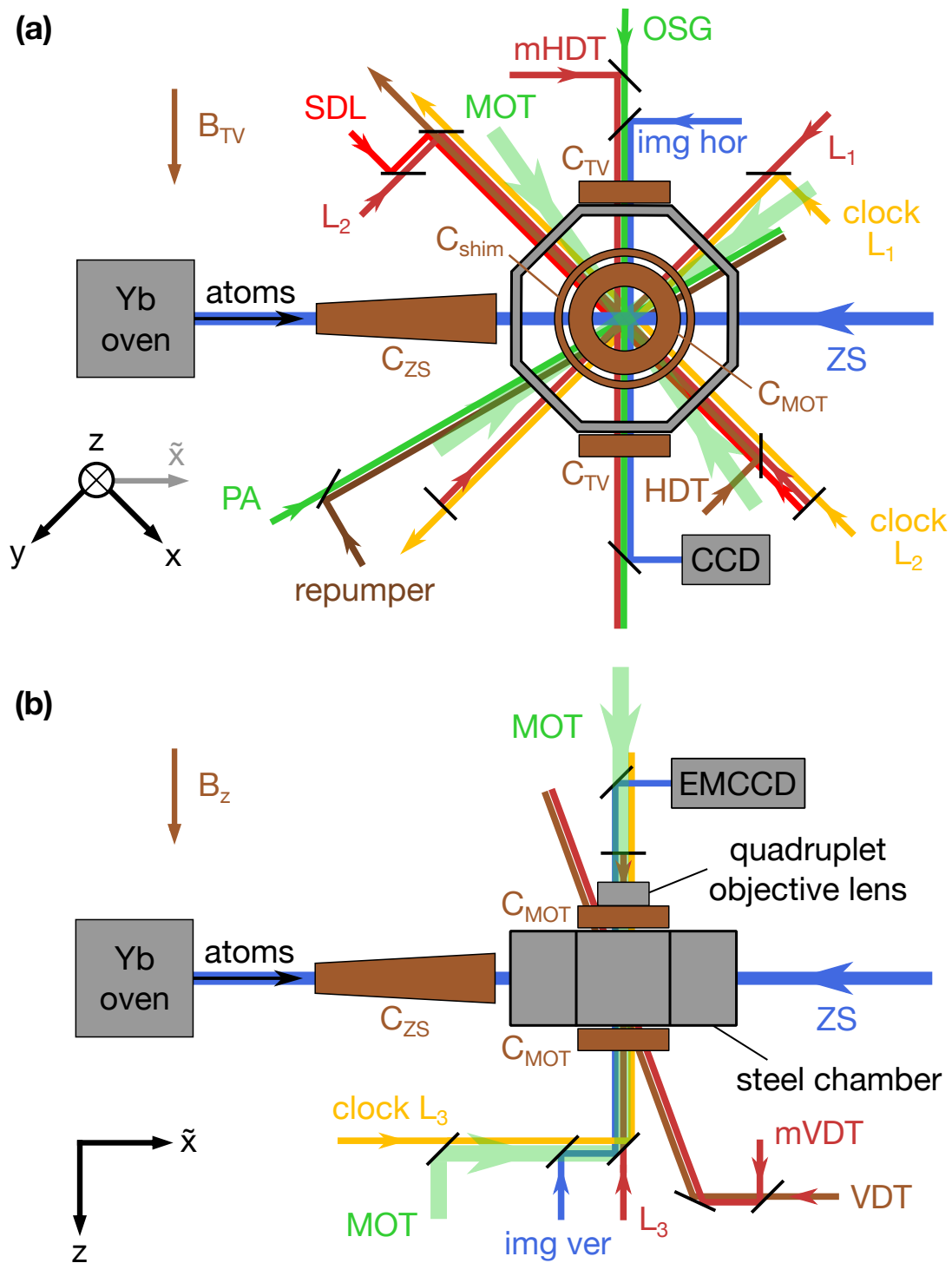
Figure 3.1 – Overview of the experimental setup. Sketch of the relevant laser beam paths and coils, shown **(a)** from the top and **(b)** from the side (not to scale). The magnetic fields B_{TV} and B_{MOT} are generated by the transverse (C_{TV}) and MOT (C_{MOT}) coils running in Helmholtz configuration, respectively. This figure is an update of the setup presented in Ref. [142], with an additional clock laser path along the lattice axis L_2. A brief description of each part of the setup is given in the main text.

time-of-flight expansion (see Section 3.2.4). Note that one full experimental cycle, which encompasses the production, manipulation and detection of an experimental sample, lasts about 30 s and needs to be be repeated for every data point taken in a measurement because of the destructive nature of our detection method.

Finally, our setup also features a 670 nm state-dependent optical lattice (SDL) as well as a 556 nm molecular photoassociation (PA) beam which have been used in previous projects but not in the frame of this thesis. In a recent upgrade, a 759 nm vertical accordion lattice has been added to the setup with a large spacing of $\approx 3.5\,\mu$m in which atoms can be loaded in one single plane from our xODT. This enables the study of clean two-dimensional systems without the need to average over multiple lattice planes when performing in-situ imaging and is an important step towards the realization of a quantum gas microscope featuring single-lattice-site imaging resolution [29–31, 156, 157]. The experiments presented in this thesis have nevertheless been performed before this upgrade, which has therefore been omitted in Fig. 3.1. A detailed description of our new vertical lattice can be found in Ref. [158].

3.1.2 Two-isotope magneto-optical trap

The ground-state s-wave scattering length $a_{gg}^{171} = -2.8\,(3.6)\,a_0$ [96] in ^{171}Yb, where a_0 denotes the Bohr radius, is strikingly small in comparison to the situation in ^{173}Yb, with $a_{gg}^{173} = 199.4\,(21)\,a_0$ [96]. While being a great feature for the study of certain Fermi-Hubbard models such as the Kondo lattice model [69, 82–84], this also results in an extremely slow thermalization rate and precludes efficient forced evaporation cooling in our xODT. This problem can be circumvented by sympathetically cooling ^{171}Yb atoms together with atoms of another isotope. As can be read from Table 2.1, ^{173}Yb and ^{174}Yb stand out as good potential candidates and have both already successfully been used in other experiments to create degenerate ^{171}Yb Fermi gases [86, 159].

In our experiment, we have implemented a two-color MOT working on the $^1S_0 \rightarrow{}^3P_1$ intercombination line to trap ^{171}Yb together with ^{174}Yb atoms, yielding an inter-isotope scattering length $a_{gg}^{171-173} = 429\,(13)\,a_0$ [96]. We use a single laser resonant with the ^{171}Yb transition together with an electro-optical modulator (EOM). The laser frequency is modulated by the EOM with a modulation frequency of 3.8 GHz corresponding to the isotope shift between ^{171}Yb and ^{174}Yb. This creates a frequency sideband resonant with the transition in ^{174}Yb while the carrier frequency still addresses the ^{171}Yb line, allowing for simultaneous trapping and cooling of both isotopes in the MOT.

The experimental sequence for loading both isotopes in the MOT is sketched in Fig. 3.2(a) and is implemented as follows. First, ^{171}Yb atoms are loaded in the MOT by setting the ZS frequency on resonance with the $^1S_0 \rightarrow{}^1P_1$ transition in ^{171}Yb and keeping the EOM off. After 8 s of ^{171}Yb loading time, the EOM is switched on and the ZS frequency tuned to the ^{174}Yb frequency such that ^{174}Yb atoms are loaded in the MOT. In the meanwhile, sufficient power is kept in the carrier frequency component to hold the ^{171}Yb atoms in the trap. After 4 s of further loading time, the MOT is compressed and $\approx 1.0 \times 10^6\ {}^{171}$Yb as well as $\approx 1.5 \times 10^6\ {}^{174}$Yb atoms are loaded into our xODT to perform evaporative cooling. Further technical details about our
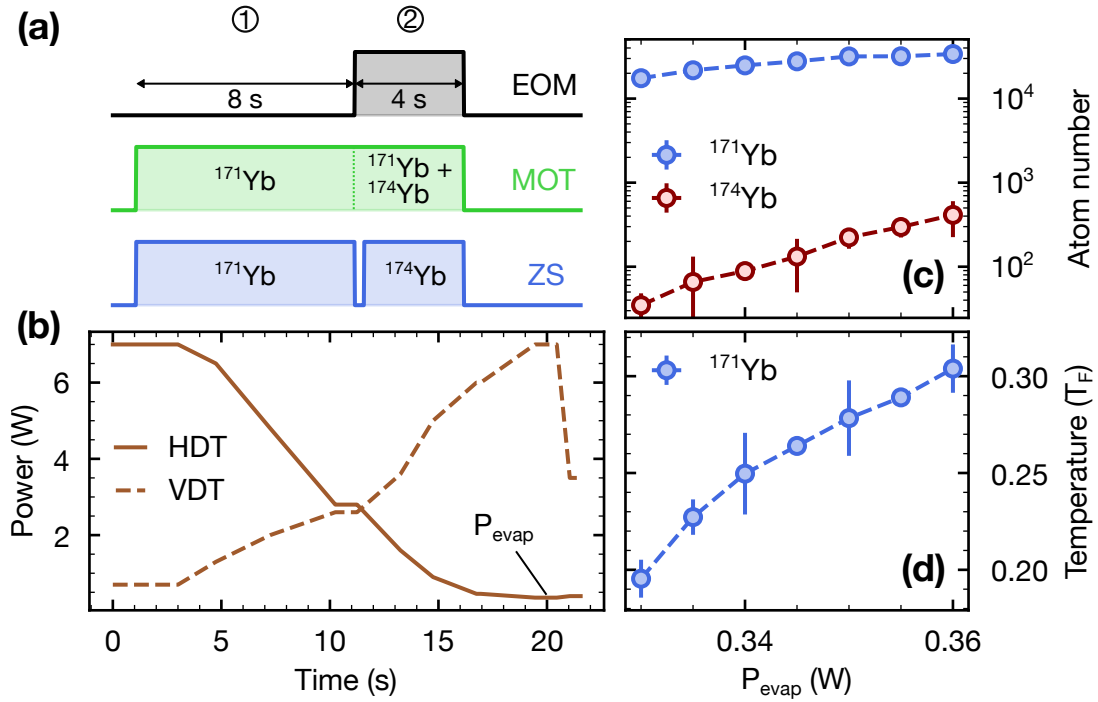
Figure 3.2 – Preparation of quantum degenerate gases of ^{171}Yb. (a) Sketch of our two-color MOT cooling sequence (not to scale). Both isotopes ^{171}Yb and ^{174}Yb are consecutively loaded in the MOT in two main steps: ① ^{171}Yb atoms are captured and cooled during $8\,$s using a ZS and MOT addressing the corresponding transitions in ^{171}Yb, ② The ZS is tuned to the ^{174}Yb transition frequency and the MOT is frequency modulated by an EOM generating a sideband addressing the transition in ^{174}Yb, thereby enabling the simultaneous trapping of both ^{171}Yb and ^{174}Yb atoms in our MOT. **(b)** Forced evaporation cooling sequence after transferring the atoms from the MOT into our xODT. The power in the HDT and in the VDT is shown as a function of time, with the lowest value of the HDT defining the evaporation threshold P_{evap}. By varying P_{evap}, both the final **(c)** atom number and **(d)** sample temperature can be tuned. In our experiments, between 2×10^4 and 3×10^4 ^{171}Yb atoms are typically prepared at a temperature $T/T_F \approx 0.25$ with $< 10^2$ ^{174}Yb atoms remaining in the trap, where T_F denotes the Fermi temperature of the gas. Error bars denote the standard error of two consecutive measurements.

two-color MOT and the preparation of quantum degenerate ^{171}Yb gases in our experiment can be found in Ref. [141].

3.1.3   Sympathetic cooling in a crossed optical dipole trap

After cooling in the MOT, the atoms are transferred into the 1064 nm xODT. The vertical VDT beam is circular with a waist $w_0 = 168\,\mu$m while the horizontal HDT beam is strongly elliptical with horizontal and vertical waists $w_{0,y} = 154\,\mu$m and $w_{0,z} = 20\,\mu$m, respectively [142]. The initial power in the HDT is 7 W while it is 0.7 W in the VDT, leading to trapping frequencies $\omega_x = 2\pi \times 10\,$Hz, $\omega_y = 2\pi \times 88\,$Hz and $\omega_z = 2\pi \times 678\,$Hz along the axes defined in Fig. 3.1. The power in the HDT is subsequently ramped down to a value P_{evap} following the nearly exponential ramp sketched in Fig. 3.2(b), which is very similar to the one used for the

evaporation of ^{173}Yb atoms in our experiment [152]. During this time, the VDT is ramped up to a maximal power of 7 W to compensate for the decrease of ω_x and ω_y when ramping down the HDT, thereby maintaining a sufficient collision rate in the xODT. The evaporation threshold P_{evap} can be varied to set the final atom number and sample temperature, as shown in Fig. 3.2(c-d). Fortunately, for sufficiently low values of P_{evap} only a negligible amount of ^{174}Yb atoms can be detected, essentially leaving only ^{171}Yb atoms in the trap at the end of the evaporation. To ensure that no ^{174}Yb atoms remain at the end of the evaporation, a short pulse resonant with the $^1S_0 \rightarrow {}^1P_1$ transition in ^{174}Yb can be used, thereby kicking all residual ^{174}Yb atoms out of the trap. In our experiment, we typically work with samples between 2×10^4 to 3×10^4 ^{171}Yb atoms at a temperature $T/T_F = 0.25$, where T_F denotes the Fermi temperature of the gas. At the end of the evaporation, typical trapping frequencies are $\omega_x = 2\pi \times 25$ Hz, $\omega_y = 2\pi \times 21$ Hz and $\omega_z = 2\pi \times 152$ Hz, leading to a final trap depth below 1 μK. Atoms are then adiabatically loaded into the cubic optical lattice in which our experiments are performed (see Section 4.1). Typical sample temperatures are low enough to ensure that all atoms are in the motional ground state of each lattice site. We have verified this by means of sideband-resolved clock-line spectroscopy in the lattice (see Section 3.3.2).

3.2 State preparation and detection

Throughout our experiments, the two main atomic internal degrees of freedom probed are the electronic state, in particular the ground state $^1S_0$ and the clock state $^3P_0$, and the nuclear spin, which can take the values $m_F = \pm 1/2$ for ^{171}Yb atoms in $^1S_0$ and $^3P_0$. The ability to reliably prepare and probe the state of an atomic sample therefore is of paramount importance to ensure well-defined and reproducible experimental conditions. In this section, the techniques used in our experiment for state preparation and detection are presented. The electronic degree of freedom is prepared by directly addressing the clock transition with a narrow-linewidth laser and is probed by separately detecting ground- and clock-state atoms by means of absorption imaging. On the other hand, the nuclear spin degree of freedom is prepared via an optical pumping scheme on the intercombination line and is probed using an optical Stern-Gerlach technique.

3.2.1 Addressing the clock transition

The electronic state of the atoms is manipulated by directly driving the $^1S_0 \rightarrow {}^3P_0$ clock transition with a resonant light pulse of wavelength 578.4 nm. To resolve interaction shifts $\sim$ kHz to the clock transition frequency, the laser addressing the transition should have a significantly narrower linewidth $\sim$ 100 Hz. While remaining orders of magnitude above the current state of the art in the context of atomic clock experiments, where linewidths $\sim$ 100 mHz have been achieved [160], these requirements still demand significant care in the design of our clock laser.

The laser source used to drive the clock transition is a 1156.8 nm external cavity diode

laser[1] developed in-house and featuring an output linewidth below 100 kHz. The laser light is amplified by a commercial tapered amplifier (TOPTICA BOOSTA PRO) and is subsequently frequency-doubled to 578.4 nm using a non-linear PPLT crystal in a bow-tie cavity, leading to a maximal available power $P_{\text{max}} \approx 100$ mW at the position of the atoms. A high-finesse reference optical cavity consisting of two mirrors separated by an ultra-low expansion (ULE) glass spacer is used to stabilize the laser via the Pound-Drever-Hall technique [162, 163]. A digital PID controller stabilizes the spacer temperature to a value corresponding to the minimum of its linear thermal expansion coefficient. The cavity is located in a vacuum chamber with a pressure $\approx 10^{-6}$ mbar which itself lies on a passive vibration-damping stage, thereby isolating it from the environment. Using a high-bandwidth control loop, this allows to reduce the laser linewidth to about 100 Hz after frequency doubling. The clock transition frequency is then calibrated in a magic-wavelength optical lattice as absolute reference. The cavity features a linear frequency drift of 1.98 kHz/day, which is compensated by our cavity offset lock. Residual non-linear drifts, which are on the order of 100 Hz/day are canceled by means of daily clock-line spectroscopy calibration measurements. Further technical details about our clock laser setup can be found in Refs. [152, 164].

Our experimental setup features three independent clock laser beam paths, each copropagating along one of the lattice axes L_1, L_2 and L_3 (see Fig. 3.1) and thereby allowing for operating in the Lamb-Dicke regime (see Section 3.3.2). While the paths along L_2 and L_3 are solely used to calibrate our optical lattice (see Section 3.3.4), the L_1 path is used as main axis along which all other measurements are performed. Along this axis, the clock laser beam has a waist $w_0 \approx 200\,\mu$m [142], leading to a maximum light intensity $I_{\text{max}} = 2P_{\text{max}}/\pi w_0^2 \approx 150$ W/cm^2. Furthermore, since the beam waist is much larger than typical cloud sizes $\approx 30\,\mu$m, the light intensity is near-constant over the extent of the cloud.

During the clock pulse, a small bias magnetic field $B \approx 1$ G is generated along the vertical axis at the position of the atoms to preserve the quantization axis, using the low-current shim coil. Larger magnetic fields are generated using both MOT coils running in Helmholtz configuration. Initially limited to $B \approx 1200$ G by the maximal output current 220 A of the power supply, the range of accessible magnetic fields has been extended by operating an additional power supply in parallel. With this upgrade, the magnetic field can theoretically take values up to $B \approx 1800$ G, limited by the maximal voltage 30 V of the power supply. In practice, we have generated magnetic fields up to 1650 G during 1 s using our MOT coils, thereby heating them up to reasonable temperatures $< 40\,°$C. Such large fields are required to observe the orbital Feshbach resonance in ^{171}Yb (see Chapter 5). In a vertical magnetic field, the clock laser light along the L_1 path is linearly polarized. An additional pair of $\lambda/2$ and $\lambda/4$ waveplates mounted on a flip mount allows for convenient switching to a circular polarization without any other change to the experimental configuration, and has been used for the measurements presented in Section 3.4.

---

[1]In a recent upgrade to the experiment, we have replaced our seed laser with a commercial amplified diode laser (TOPTICA TA PRO), leading to enhanced lock stability. Further details can be found in Ref. [161].

3.2.2   Strong saturation absorption imaging

The only directly accessible observable in our experiment is the atomic density distribution, which we access via the standard absorption imaging technique [165]. The in-situ column density distribution is measured by illuminating the atomic cloud with a vertically propagating circularly polarized laser beam resonant with the $|^1S_0, F = 1/2\rangle \rightarrow |^1P_1, F = 3/2\rangle$ transition for a short time Δt. We use high intensity pulses with $\Delta t = 15\,\mu$s, which minimizes atomic motion during the pulse while providing sufficient light to fully penetrate the atomic cloud. At the position of the atoms, the beam waist is about $220\,\mu$m, such that the intensity of the imaging light can be considered constant over the spatial extent of the atomic cloud, which is typically about $30\,\mu$m. During the imaging pulse, a small vertical bias field of $1\,$G is applied to define a quantization axis while keeping the Zeeman splitting of the hyperfine m_F states very small compared to the linewidth of the atomic transition. The beam is imaged in the atomic plane using a high-resolution quadruplet-lens objective with numerical aperture NA = 0.27, which allows for a diffraction-limited resolution of $1.3\,\mu$m [153]. In reality, imperfections in our imaging system such as astigmatism and spherical aberrations limit the resolution to $\approx 3\,\mu$m [118], a value determined after reconstructing the image response function from local density fluctuation measurements[2] [166].

The image is recorded on an EMCCD camera sensor, with an image magnification $\gamma = 0.47\,\mu$m/px [153]. Neglecting imperfections such as photon noise, dark noise or read noise, the number of counts $C(i,j)$ recorded by the sensor on each pixel of position (i,j) is proportional to the incident light intensity $I(i,j)$ and can be expressed as

$$C(i,j) = C_P(i,j) Q_E g, \qquad (3.1)$$

where $C_P(i,j) = I(i,j)\gamma^2 \Delta t / \hbar\omega$ is the number of photons hitting the pixel during the pulse, ω the frequency of the imaging light, Q_E the quantum efficiency of the detector and g the electron-multiplying gain of the camera. The quantum efficiency represents the fraction of photons converted into electron-hole pairs that are successfully detected by the device.

The imaging light intensity, propagating along the axis z, undergoes an attenuation through atomic absorption which can be described as

$$\frac{\mathrm{d}I}{\mathrm{d}z} = -\sigma \frac{I(\mathbf{r})}{1 + \dfrac{I(\mathbf{r})}{I_{\text{sat}}}} n(\mathbf{r}), \qquad (3.2)$$

where $n(\mathbf{r})$ denotes the atomic density distribution, σ the effective absorption cross-section and I_{sat} the effective saturation intensity. Using the resonant absorption cross-section $\sigma_0 = 6\pi c^2/\omega^2$ for a two-level system, we can write $\sigma = \sigma_0/\alpha$, where $\alpha > 1$ accounts for imperfect polarization of the imaging beam, the multi-level structure of the atom or residual detuning of the imaging light [167]. The correction factor α effectively reduces the absorption cross-section σ and has to be determined experimentally since it depends on the specific conditions

---

[2]We have recently added a cylindrical lens in the imaging path to compensate for astigmatism. This has improved the imaging resolution to $\lesssim 2\,\mu$m. However, the experiments presented in this thesis have been performed with a resolution of $\approx 3\,\mu$m.

in which the imaging is performed. Similarly, we have $I_{\text{sat}} = \alpha I_{\text{sat}}^0$, where I_{sat}^0 denotes the two-level saturation intensity. Integrating Eq. (3.2) along z through the entire extent of the cloud leads to [167]

$$n_c(x,y) = \frac{\alpha}{\sigma_0} \left\{ \ln\left[\frac{I_i(x,y)}{I_f(x,y)}\right] + \frac{I_i(x,y) - I_f(x,y)}{\alpha I_{\text{sat}}^0} \right\}, \qquad (3.3)$$

defining the imaging light intensity profiles $I_i(x,y)$ and $I_f(x,y)$ before and after hitting the atoms, respectively, as well as the atomic column density $n_c(x,y) = \int n(\mathbf{r})\,dz$, which is the observable measured in our experiment. Note that Eq. (3.3) is valid for any light intensity, in particular in the saturated regime where $I \gtrsim I_{\text{sat}}$ as well. In terms of counts recorded by each camera pixel, Eq. (3.3) takes the form

$$\sigma_0 n_c(i,j) = \alpha \ln\left[\frac{C_i(i,j)}{C_f(i,j)}\right] + \beta\left[C_i(x,y) - C_f(x,y)\right], \qquad (3.4)$$

with $\beta = 1/\left(C_{\text{sat}}^0 \Delta t\right)$, where $C_{\text{sat}}^0 = I_{\text{sat}}^0 \gamma^2 Q_E g / \hbar\omega$ denotes the count rate per pixel corresponding to a light intensity I_{sat}^0. We estimate this quantity by comparing the peak counts recorded by the camera for a given pulse time to the corresponding peak intensity in units of I_{sat}^0, leading to $C_{\text{sat}}^0 \approx 75.3\,\text{MHz}$.

In practice, the column density distribution is reconstructed by taking three images. First, an imaging pulse is performed in the presence of the atoms. This leads to the measurement of $C_f(i,j)$ on the camera sensor and removes all atoms from the trap because of the large associated photon recoil energy. After that, a second identical imaging pulse is performed in the absence of atoms, giving access to $C_i(i,j)$. Finally, a third image $C_{\text{bg}}(i,j)$ is taken in the absence of imaging light to take into account any background light illumination such that $C_{i,f}(i,j) \rightarrow C_{i,f}(i,j) - C_{\text{bg}}(i,j)$. On Fig. 3.3(a), a typical absorption image of ground-state ^{171}Yb atoms is shown.

Imaging clock-state atoms

The absorption imaging technique used in our experiment only allows for the detection of atoms in the electronic ground state $^1\text{S}_0$. However, our experiments also involve atoms in the clock state $^3\text{P}_0$, which need to be detected as well. In principle, the clock-state population can be indirectly probed via the loss of ground-state atoms. The signal-to-noise ratio is then limited by shot-to-shot fluctuations in the total atom number arising from sample preparation, making in particular small fractions of atoms in the clock state undetectable.

To circumvent this issue, we repump clock-state atoms back to the ground state by driving the $^3\text{P}_0 \rightarrow {}^3\text{D}_1$ transition with a laser of wavelength $1389\,\text{nm}$. Technical details about the setup can be found in Ref. [168]. Atoms in the $^3\text{D}_1$ state decay to the $^3\text{P}_0$, $^3\text{P}_1$ and $^3\text{P}_2$ states, with branching ratios of 0.64, 0.35 and 0.01, respectively. From the $^3\text{P}_1$ state, atoms quickly decay to the ground state, achieving a theoretical maximum repumping efficiency after multiple cycles of 97.5% [168, 169], which is only limited by the fraction of atoms ending up in the dark metastable $^3\text{P}_2$ state. In practice, we measure a repumping efficiency of 70.5(5.1)% by
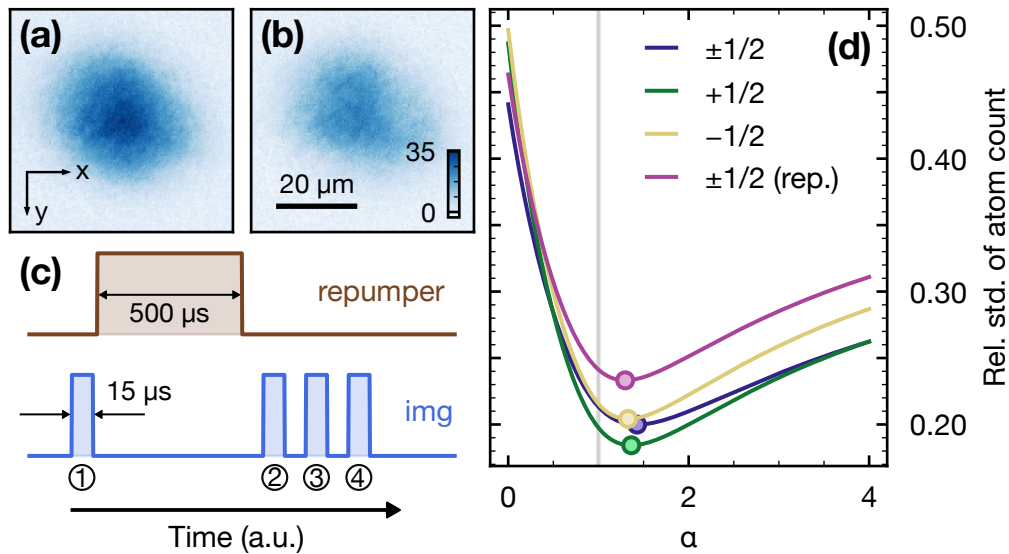
Figure 3.3 – **Strong saturation absorption imaging of ground- and clock- state atoms.** We show the atomic column density in a cubic optical lattice in units of $\mu\mathrm{m}^{-2}$ measured via absorption imaging of **(a)** ground-state and **(b)** clock-state atoms repumped back to the ground state, both imaged separately at the end of one experimental cycle. The total number of atoms in each state is obtained by summing up the column density in each pixel. **(c)** Schematic representation of the imaging sequence in our experiment (not to scale). A first imaging pulse ① is performed, addressing the atoms in the ground state. A $500\,\mu s$ repumper pulse subsequently brings about 70% of the clock-state atoms back to the ground state, which are imaged separately by a second imaging pulse ②. After that, two additional imaging pulses ③ and ④ are performed without atoms as reference. **(d)** High-intensity imaging calibration. The relative standard deviation of the atom number measured with various imaging light intensities is shown as a function of the parameter α in Eq. (3.4) (solid lines). The optimum value $\alpha = \alpha^*$ (circles) minimizes the standard deviation. We measure α^* for samples with nuclear spin $m_F = \pm 1/2, +1/2, -1/2$ and for repumped atoms. The gray vertical line indicates the uncorrected case $\alpha = 1$.

comparing the sum of repumped atoms detected after exciting all atoms to the clock state to the initial ground-state atom number.

The imaging sequence allowing for separate detection of $^1\mathrm{S}_0$ and $^3\mathrm{P}_0$ atoms in our experiment is sketched in Fig. 3.3(c). After detecting the ground-state atoms with a first imaging pulse, a $500\,\mu s$ repumper pulse is performed and the clock-state atoms are subsequently detected with a second imaging pulse. After that, a third and fourth imaging pulses are performed in the absence of atoms as reference $C_i(i,j)$. A single background image $C_{\mathrm{bg}}(i,j)$ in the absence of light is taken every day before taking data.

Experimental determination of the imaging parameter α

The parameter α in Eq. (3.4) is experimentally determined by requiring the total atom number to be independent of the imaging light intensity [167]. We take multiple images with different probe intensities and choose the value of $\alpha = \alpha^*$ that minimizes the atom number variance, as is shown in Fig. 3.3(d). We measure α^* for samples with $m_F = +1/2$, $m_F = -1/2$, $m_F = $

$\pm 1/2$ as well as for repumped clock-state atoms, and obtain $\alpha^* = 1.36$, $\alpha^* = 1.33$, $\alpha^* = 1.43$ and $\alpha^* = 1.30$, respectively. These values are significantly lower than for ^{173}Yb in our experiment [118], which can be attributed to the simpler hyperfine structure in ^{171}Yb.

Time-of-flight imaging

In addition to vertical in-situ imaging, our experimental setup also allows for the horizontal imaging of atoms after a given time of flight with all traps switched off, giving access to their momentum distribution. This technique is used in this work to determine the temperature of the sample and to perform optical Stern-Gerlach spin state detection (see Section 3.2.4).

3.2.3 Nuclear spin state preparation

In the experiments reported in this thesis, spin-balanced as well as spin-polarized samples are used. This requires an optical pumping scheme enabling the preparation of any desired nuclear spin state mixture. In the absence of optical pumping, the sample is fully spin-unpolarized at the end of the evaporation in the crossed dipole trap [152] and consists of atoms in the electronic ground state ^{1}S$_0$ in a balanced statistical mixture of both nuclear spin states $m_F = \pm 1/2$. This configuration is typically used when two-body interactions are probed, as for example interorbital interactions. On the other hand, it is advantageous to prepare spin-polarized samples when probing single-particle physics, such as bare clock transition lines, which are important references in our measurements. This allows for a clean sample with a well-identified nuclear spin state, removes interaction-induced effects and maximizes the signal-to-noise ratio since all atoms are addressed by the same clock laser frequency even at finite magnetic fields.

The optical pumping scheme used in our experiments is based on a single light pulse driving the $|^1$S$_0, F = 1/2\rangle \to |^3P_1, F' = 3/2\rangle$ transition. The degeneracy of the hyperfine states m_F in the $|^3$P$_1, F' = 3/2\rangle$ manifold is lifted by applying a bias magnetic field of $B = 50\,$G along the vertical axis, which is produced by both MOT coils running in Helmholtz configuration. One of the circularly polarized vertical MOT beams is then used to drive the transition, depending on the nuclear spin state to be prepared. To prepare a spin-polarized sample in the $m_F = +1/2$ state, we drive the $|^1$S$_0, m_F = -1/2\rangle \to |^3P_1, m_F = +1/2\rangle$ transition with σ^+-polarized light (top MOT beam), as illustrated on Fig. 3.4(a). Similarly, all atoms are prepared in the $m_F = -1/2$ state by driving the $|^1$S$_0, m_F = +1/2\rangle \to |^3P_1, m_F = -1/2\rangle$ with σ^--polarized light (bottom MOT beam), as shown on Fig. 3.4(b). The optical pumping pulse is performed at the beginning of the evaporation, before starting to ramp down the horizontal dipole trap, in order to ensure a minimal effect on the final sample temperature.

The response of the system to an optical pumping pulse as a function of the driving frequency is displayed in Fig. 3.4(c) for various magnetic fields, showing that the sample can be fully spin-polarized for resonant pulses. In particular, a magnetic field of $50\,$G ensures a sufficient hyperfine splitting to address single transitions. From Fig. 3.4(c), the linear Zeeman shift of atoms in the ^{3}P$_1$ state can be determined, as shown in Fig. 3.4(d), leading to a shift of $1.414(6)\,$MHz$/(\mathrm{G} \times m_F)$. This is in excellent agreement with the expected value
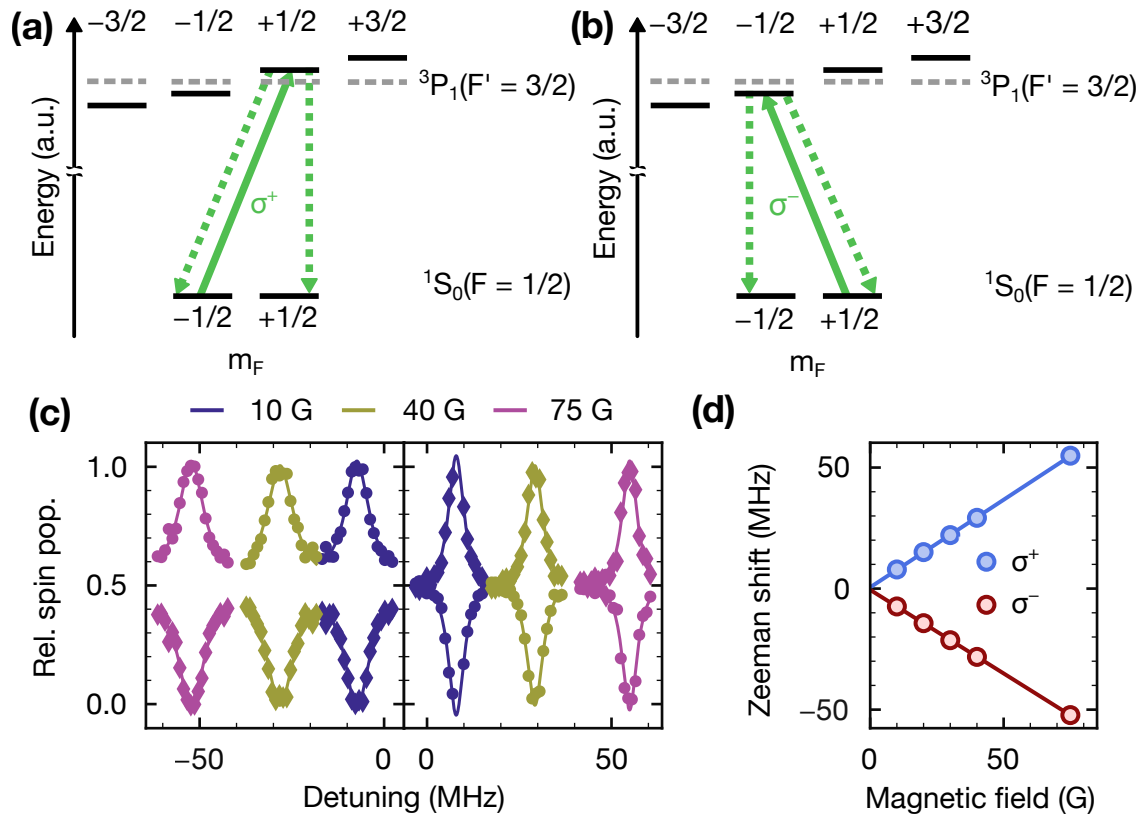
Figure 3.4 – **Nuclear spin state preparation with optical pumping. (a)-(b)** Optical pumping schemes for the preparation of spin-polarized samples with atoms in the states $|^1S_0, m_F = +1/2\rangle$ and $|^1S_0, m_F = -1/2\rangle$, respectively. The optical pumping pulses are performed with resonant σ^+ and σ^--polarized light on the $|^1S_0, F = 1/2\rangle \rightarrow |^3P_1, F' = 3/2\rangle$ transition, respectively (solid green lines). Dashed green lines denote possible decays via spontaneous emission. Solid black lines show the relevant hyperfine energy levels at finite magnetic fields B (not to scale), compared to the situation for $B = 0$ (dashed grey lines). The Zeeman shift for atoms in the electronic ground state $^1S_0$ is three orders of magnitudes smaller than in the $^3P_1$ state and is therefore omitted. **(c)** Relative population in the $m_F = +1/2$ (diamonds) and $m_F = -1/2$ (circles) spin states after a σ^+- (right panel) and σ^--polarized (left panel) optical pumping pulse as a function of the laser detuning with respect to the transition frequency at zero magnetic field. We show data taken at $B = 10\,$G, $40\,$G and $75\,$G. Solid lines denote Lorentzian fits to the data. The relative populations are measured using the optical Stern-Gerlach technique introduced in Section 3.2.4. **(d)** Shift of the σ^- (red) and σ^+ (blue) lines extracted from fits to data as shown in (c). Solid lines are linear fits to the data points, corresponding to a linear Zeeman shift of $\pm 707(3)\,$kHz$/$G for the $m_F = \pm 1/2$ states.

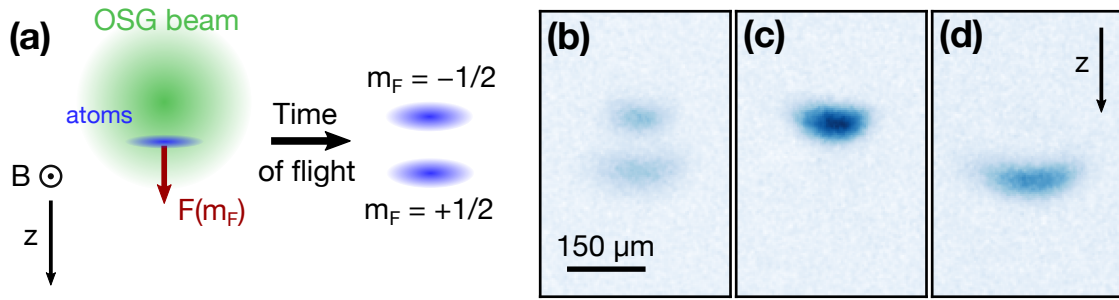**Figure 3.5** – **Optical Stern-Gerlach (OSG) nuclear spin state detection. (a)** Working principle of the OSG detection method. A σ^+-polarized horizontal laser beam blue-detuned with respect to the $|^1S_0, F = 1/2\rangle \to |^3P_1, F = 3/2\rangle$ transition is shone on the atoms in an external magnetic field B_{TV}. The center of the beam is shifted vertically with respect to the atoms to maximize the intensity gradient experienced by the atoms, which yields a spin-dependent vertical force $F(m_F)$. After a certain time of flight, this divides the cloud into two regions corresponding to both nuclear spin states that can then be separately detected. The z axis corresponds to the direction of gravity. **(b)** OSG detection image of a spin-unpolarized sample, showing a clear separation in two equally populated clouds corresponding to each nuclear spin state $m_F = \pm 1/2$. **(c)-(d)** OSG detection image of spin-polarized samples prepared in $m_F = -1/2$ and $m_F = +1/2$, respectively. No residual atoms are observed in the undesired spin state.

$\mu_B g_F = 1.4\,\text{MHz}/(\text{G} \times m_F)$, with the Landé g factor $g_F = 1$ for the $|^3P_1, F' = 3/2\rangle$ state and Bohr magneton μ_B. Here, the Zeeman shift of the ground state is neglected since it solely arises from the nuclear spin and is thus three orders of magnitude smaller.

3.2.4 Optical Stern-Gerlach nuclear spin state detection

With alkali atoms, a standard spin detection technique consists in time-of-flight imaging combined with a magnetic field gradient exerting a spin-dependent force on the atoms [165], using the Stern-Gerlach effect [170]. However, the very small angular momentum in the ground and clock state of alkaline-earth(-like) atoms due to the zero total electronic angular momentum requires extremely large magnetic field gradients to spatially separate the different spin states. Instead, an optical Stern-Gerlach (OSG) technique [171] is used to effectively detect the nuclear spin state m_F.

In our experiment, a m_F-dependent force is applied to the atoms by exposing them to a short horizontally propagating σ^+-polarized laser pulse with other traps switched off, as illustrated in Fig. 3.5(a). The pulse has a duration of 1.5 ms and is performed in a transverse magnetic field $B_{TV} = 20\,\text{G}$. The light is blue-detuned by 250 MHz with respect to the $|^1S_0, F = 1/2\rangle \to |^3P_1, F' = 3/2\rangle$ transition. A large and nearly-uniform light intensity gradient is achieved by vertically shifting the beam position with respect to the atoms. This induces a dipole force on the atoms, which depends monotonically on the light intensity gradient and on m_F [152]. The atoms are then imaged after a 12 ms time of flight to resolve the momentum kicks experienced by atoms in different m_F states. On Figs 3.5(b-d), spin detection images are displayed for spin-balanced as well as spin-polarized samples, representing all the relevant spin configurations for our experiments.

3.3   Clock-line spectroscopy in a magic-wavelength lattice

One of the most striking features of alkaline-earth(-like) atoms such as ytterbium or strontium arguably is their ultranarrow electronic clock transition, which currently lies at the heart of the most accurate clocks in the world [6, 99, 123]. In the experiments presented in this thesis, this transition always plays an essential role. On one hand, the narrow linewidth enables precise clock-line spectroscopy in an optical lattice, where the energy shifts caused by two-body interactions can be resolved. On the other hand, it allows for the reliable preparation of the system in any desired initial electronic state. In this section, we review the theoretical behavior of a two-level atom driven by a near-resonant monochromatic light field and demonstrate how this simple model can be readily applied to describe clock-line spectroscopy measurements in a magic-wavelength optical lattice. We also show how sideband-resolved clock spectroscopy can be used in combination with high-resolution in-situ imaging of the atoms for spatially-resolved lattice depth calibration.

3.3.1   Two-level atom driven by a near-resonant light field

The driving of an ytterbium atom from the electronic ground state $^{1}S_{0}$ to the clock state $^{3}P_{0}$ with near-resonant narrow-linewidth laser light can be readily described within the standard semi-classical framework of a two-level atom coupled to an external light field [172], also known as Rabi problem. Consider a single atom at rest with two states $|g\rangle$ and $|e\rangle$ which are the eigenstates of the two-level Hamiltonian $\hat{H}_{e}$ given by

$$\hat{H}_{e} = -\frac{\hbar\omega_{0}}{2}|g\rangle\langle g| + \frac{\hbar\omega_{0}}{2}|e\rangle\langle e| = \frac{\hbar\omega_{0}}{2}\hat{\sigma}_{z}, \tag{3.5}$$

defining the Pauli matrix $\hat{\sigma}_{z}$ and the energy splitting $\hbar\omega_{0}$ between $|g\rangle$ and $|e\rangle$. We now investigate the time evolution of the system in the presence of a monochromatic electromagnetic plane wave, with an electric field of the form

$$\mathbf{E}(\mathbf{r},t) = \frac{E_{0}\hat{\epsilon}}{2}\left[e^{i(\mathbf{k}\cdot\mathbf{r}-\omega t+\phi)} + e^{-i(\mathbf{k}\cdot\mathbf{r}-\omega t+\phi)}\right], \tag{3.6}$$

with $\omega = 2\pi c/\lambda$ and $|\mathbf{k}| = 2\pi/\lambda$, where λ is the wavelength of the electromagnetic wave, E_{0} its amplitude, $\hat{\epsilon}$ its polarization and ϕ an arbitrary phase shift. In ^{171}Yb, the laser driving the clock transition has a wavelength of $\lambda = 578$ nm whereas the atomic radius is estimated to be about $a \sim 0.175$ nm [173]. The electric field can therefore be treated as constant within the spatial extent of a single atom since $k \cdot a \sim 10^{-3} \ll 1$, an approximation known as dipole approximation. This allows us to drop the spatial dependence in Eq. (3.6) and write

$$\mathbf{E}(t) = \frac{E_{0}\hat{\epsilon}}{2}\left[e^{i(\omega t+\phi)} + e^{-i(\omega t+\phi)}\right]. \tag{3.7}$$

The electric dipole interaction between the atom and the field is given by [174]

$$\hat{H}_{I}(t) = -e\hat{\mathbf{r}}\cdot\mathbf{E}(t), \tag{3.8}$$

where $\hat{\mathbf{r}}$ is the position operator and e the elementary charge. With the help of Eq. (3.7) and dropping the phase ϕ for simplicity, we obtain

$$
\begin{aligned}
\hat{H}_I(t) &= \frac{\hbar\Omega_0}{2} \left(|e\rangle\langle g| + |g\rangle\langle e|\right)\left(e^{i\omega t} + e^{-i\omega t}\right) \\
&= \frac{\hbar\Omega_0}{2}\left(\hat{\sigma}_+ + \hat{\sigma}_-\right)\left(e^{i\omega t} + e^{-i\omega t}\right),
\end{aligned}
\tag{3.9}
$$

defining the ladder operators $\hat{\sigma}_\pm$ and the Rabi frequency

$$
\Omega_0 = \frac{\mathbf{d}_{ge}\cdot\hat{e}E_0}{\hbar},
\tag{3.10}
$$

where $\mathbf{d}_{ge} = \langle g|(-e\hat{\mathbf{r}})|e\rangle$ is the (real) transition dipole moment for the $|g\rangle \to |e\rangle$ transition. The full Hamiltonian of the system is then given by $\hat{H} = \hat{H}_e + \hat{H}_I$.

The problem is most conveniently solved in the interaction picture, performing the unitary transformation $\hat{H}_I'(t) = e^{i\hat{H}_e t/\hbar}\hat{H}_I(t)e^{-i\hat{H}_e t/\hbar}$. We obtain

$$
\hat{H}_I'(t) = \frac{\hbar\Omega_0}{2}\left(\hat{\sigma}_+ e^{-i\delta t + i(2\omega_0+\delta)t} + \hat{\sigma}_- e^{i\delta t - i(2\omega_0+\delta)t}\right),
\tag{3.11}
$$

where we have defined the detuning $\delta = \omega - \omega_0$ between the frequency of the driving laser and of the atomic transition. In our experiments, we typically work with detunings up to $\delta \sim 10^4\,$Hz, which are extremely small compared to the transition frequency $\omega_0 \sim 10^{17}\,$Hz. Terms proportional to $e^{\pm i(2\omega_0+\delta)t}$ therefore oscillate much faster than those proportional to $e^{\pm i\delta t}$ and effectively average out to zero since the time dynamics is essentially dominated by $e^{\pm i\delta t}$. We hence neglect these terms in Eq. (3.11). This is called the rotating wave approximation, under which the interaction Hamiltonian takes the simpler form

$$
\hat{H}_I'(t) = \frac{\hbar\Omega_0}{2}\left(\hat{\sigma}_+ e^{-i\delta t} + \hat{\sigma}_- e^{i\delta t}\right).
\tag{3.12}
$$

In general, we can express the state of the system as

$$
|\psi'(t)\rangle = c_g(t)|g\rangle + c_e(t)|e\rangle,
\tag{3.13}
$$

where $c_g(t)$ and $c_e(t)$ are complex coefficients obeying the normalization condition $\left|c_g(t)\right|^2 + |c_e(t)|^2 = 1$. The time evolution of the state is then given by $i\hbar\partial_t|\psi'(t)\rangle = \hat{H}_I'(t)|\psi'(t)\rangle$ and leads to the differential equations

$$
\begin{aligned}
\dot{c}_g(t) &= -\frac{i\Omega_0}{2}e^{i\delta t}c_e(t), \\
\dot{c}_e(t) &= -\frac{i\Omega_0}{2}e^{-i\delta t}c_g(t).
\end{aligned}
\tag{3.14}
$$

Let us consider an atom initially in the state $|g\rangle$ such that $c_g(t=0) = 1$ and $c_e(t=0) = 0$. We can then compute the probability $P_e(t,\Omega_0,\delta)$ for the atom to be in the state $|e\rangle$ as

$$
P_e(t,\Omega_0,\delta) = |c_e(t,\Omega_0,\delta)|^2 = \left(\frac{\Omega_0}{\Omega}\right)^2\sin^2\left(\frac{\Omega t}{2}\right),
\tag{3.15}
$$

where we have defined the generalized Rabi frequency $\Omega = \sqrt{\Omega_0^2 + \delta^2}$. Note that this result neglects the finite lifetime of the state $|e\rangle$ and decoherence effects. From Eq. (3.15), it is clear that an atom can be prepared in the state $|e\rangle$ when addressed with a resonant light pulse ($\delta = 0$) of duration $t_\pi = \pi/\Omega_0$ (or in general $t = (2n+1)\pi/\Omega_0$, with n a non-negative integer). Such a pulse is called π pulse since it drives the atom from $|g\rangle$ to $|e\rangle$, corresponding to a rotation of angle π on the Bloch sphere. When scanning the pulse time on resonance, the atom undergoes oscillations with frequency Ω_0 given by

$$P_e(t) = \sin^2\left(\frac{\Omega_0 t}{2}\right), \tag{3.16}$$

known as Rabi oscillations. On the other hand, scanning the detuning δ of a π pulse leads to a response

$$P_e(\delta) = \left(\frac{\pi}{2}\right)^2 \text{sinc}^2\left(\frac{\pi}{2}\sqrt{1 + \frac{\delta^2}{\Omega_0^2}}\right). \tag{3.17}$$

In our experiment, we do not work with single atoms but with larger samples consisting of $\sim 10^4$ atoms instead. In this case, the probability $P_e(t, \Omega_0, \delta)$ defined in Eq. (3.15) is equivalent to the fraction of atoms detected in the state $|e\rangle$. After driving atoms from the electronic ground state $^1S_0$ to the clock state $^3P_0$, we determine the fraction excited to $^3P_0$ by separately measuring the number of atoms in the $^1S_0$ and in the $^3P_0$ state as described in Section 3.2.2.

Typical clock-line spectroscopy measurements consist in varying the frequency of clock-laser pulses of duration t_π and fitting the response of the system to Eq. (3.17), gaining access to the transition frequency ω_0. In practice, the measured fraction of excited atoms is always smaller than one, even with resonant π pulses. This can be due to our clock laser beam profile being inhomogeneous, from the finite coherence time or linewidth of our clock laser or from the repumping efficiency of $^3P_0$ atoms to the $^1S_0$ state for imaging. We take this into account by adding a global multiplication factor < 1 to Eq. (3.17) as free fit parameter, and also add a global offset accounting for any residual background excited fraction measured. Two examples of such measurements including fits to the data are shown in Fig. 3.6(a) for different Rabi frequencies Ω_0. As expected from Eq. (3.17), the resonance becomes narrower for lower Rabi frequencies, which is desirable for the precise determination of the resonance position. The Rabi frequency can be tuned by varying the intensity I of the clock laser, since it scales as $\sqrt{I}$ as can be read from Eq. (3.10).

Similarly, the Rabi frequency Ω_0 for a given clock laser power is probed by scanning the duration of resonant laser pulses, driving the Rabi oscillations defined in Eq. (3.16). In Fig. 3.6(b), two examples of such measurements for different Rabi frequencies are shown. As expected from Eq. (3.16), larger Rabi frequencies, which correspond to larger light intensities I, lead to faster Rabi oscillations. By fitting the Rabi frequency for certain experimental parameters, the π pulse time t_π used in clock-line spectroscopy measurements such as the ones shown in Fig. 3.6(a) is calibrated.

Note that instead of π pulses, long resonant pulses exceeding the coherence time of the clock-excitation light can be used. In that case, the Rabi oscillations shown in Fig.3.6(b) are
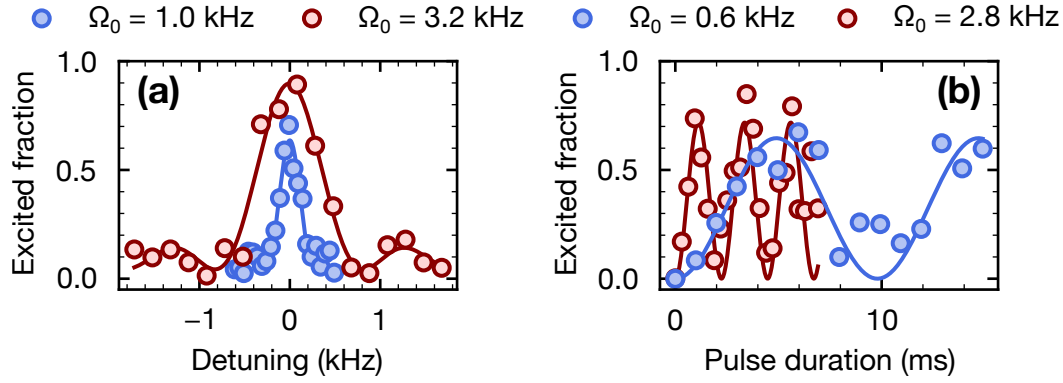
Figure 3.6 – **Clock-line spectroscopy and Rabi oscillations.** We measure the response of a spin-polarized sample in a 30 E_{rec} magic-wavelength cubic lattice by determining the fraction of atoms in the clock state after a laser excitation pulse. The excited fraction is computed after separately imaging the atoms in the ground and in the clock state, as described in Section 3.2.2. **(a)** Scan of the pulse frequency detuning δ with respect to the atomic transition for constant pulse duration t_π. We show two data sets with different Rabi frequencies Ω_0. The data is well-fitted with a Rabi lineshape of the form of Eq. (3.17) (solid lines), allowing us to extract the resonance frequency where $\delta = 0$. **(b)** Scan of the pulse duration on resonance. We again show two data sets with different Rabi frequencies. The data is well-fitted with Rabi oscillations of the form of Eq. (3.16), allowing us to extract the Rabi frequency.

damped and the excited fraction reaches the asymptotic value of $1/2$. These incoherent pulses are used in this work to address the molecular bound state associated with the orbital Feshbach resonance in ^{171}Yb in Chapters 5 and 6.

3.3.2   Clock-line spectroscopy in an optical lattice

The results presented in Section 3.3.1 are valid for atoms at rest. In real-life experiments, however, atoms possess a motional degree of freedom which affects the clock line through atomic interactions, Doppler shifts and photon recoil. To decouple the motional and internal degrees of freedom, a solution is to strongly confine the atoms in a tight trap, in the Lamb-Dicke regime [175] where the trap size is smaller than the wavelength of the trapping light. For neutral atoms, this can be achieved by the use of a deep one- or three-dimensional optical lattice which traps the atoms in a near-harmonic potential [176, 177]. This creates a situation similar to ions in Paul or Penning traps [178, 179]. In our experiments, another crucial advantage of a tight trapping potential is that it creates strongly confined pairs of atoms on the same lattice site, resolving interaction-induced energy shifts. Using Eq. (2.49) and assuming an s-wave scattering length of $a \sim 10^2 \, a_0$, where a_0 denotes the Bohr radius, a $30 \, E_{rec}$ deep three-dimensional lattice of wavelength $759 \, nm$ leads to an interaction shift of $\sim 10^3 \, Hz$, which is one order of magnitude larger than the linewidth $\sim 10^2 \, Hz$ of our clock laser.

The on-site potential in a deep optical lattice can be approximated to be harmonic, as

shown in Section 2.3.1. The motional Hamiltonian seen by an atom is then

$$\hat{H}_m = \frac{\hat{p}^2}{2m} + \frac{1}{2}m\omega_{\text{ho}}^2\hat{x}^2,$$

(3.18)

with the harmonic oscillator frequency ω_{ho} given by Eq. (2.39). The above equation can be rewritten in the standard form [180]

$$\hat{H}_m = \hbar\omega_{\text{ho}}\left(\hat{n} + \frac{1}{2}\right),$$

(3.19)

using the number operator $\hat{n} = \hat{a}^\dagger\hat{a}$, where $\hat{a} = \sqrt{m\omega_{\text{ho}}/2\hbar}(\hat{x} + i\hat{p}/m\omega_{\text{ho}})$ and $\hat{a}^\dagger$ denote the annihilation and creation operators, respectively. In such a potential, atoms experience a periodic motion. The position dependency in Eq. (3.6) must therefore be kept. Similarly to the case in Section 3.3.1, we compute the electric dipole interaction Hamiltonian in the interaction picture, using this time $\hat{H}_0 = \hat{H}_e + \hat{H}_m$ as non-interacting Hamiltonian. We obtain

$$H_I'(t) = \frac{\hbar\Omega_0}{2}\left\{\hat{\sigma}_+\exp\left[i\eta\left(\hat{a}e^{-i\omega_{\text{ho}}t} + \hat{a}^\dagger e^{+i\omega_{\text{ho}}t}\right) - i\delta t\right] + \text{h.c}\right\},$$

(3.20)

introducing the Lamb-Dicke parameter $\eta = kx_0$, where k is the wave vector of the laser driving the transition projected on the lattice axis and $x_0 = \sqrt{\hbar/2m\omega_{\text{ho}}}$ the harmonic oscillator length.

In the Lamb-Dicke regime, we have $\eta \ll 1$ and Eq. (3.20) can be expanded to first order, leading to

$$H_I'(t) = \frac{\hbar\Omega_0}{2}\left\{\hat{\sigma}_+e^{i\delta t}\left[1 + i\eta\left(\hat{a}e^{-i\omega_{\text{ho}}t} + \hat{a}^\dagger e^{+i\omega_{\text{ho}}t}\right)\right] + \text{h.c}\right\}.$$

(3.21)

This Hamiltonian basically consists of three contributions, and can be written as $H_I'(t) = H_c'(t) + H_{rs}'(t) + H_{bs}'(t)$. The carrier part of the Hamiltonian is given by

$$H_c'(t) = \frac{\hbar\Omega_0}{2}\hat{\sigma}_+e^{-i\delta t} + \text{h.c},$$

(3.22)

which is strictly identical to Eq. (3.12) since it is independent of the motional degree of freedom. It couples $|g,n\rangle \leftrightarrow |e,n\rangle$ states with a Rabi frequency Ω_0 and is resonant for $\delta = 0$, leading to a resonance with a shape given by Eq. (3.15). The red sideband part of the Hamiltonian is of the form

$$H_{rs}'(t) = \frac{\hbar\Omega_{rs}}{2}\hat{\sigma}_+\hat{a}e^{-i(\delta+\omega_{\text{ho}})} + \text{h.c},$$

(3.23)

which couples $|g,n\rangle \leftrightarrow |e,n-1\rangle$ states. It again leads to a resonance with a shape given by Eq. (3.15) but with a Rabi frequency $\Omega_{rs} = \Omega_0\eta\sqrt{n}$ and a resonance position $\delta = -\omega_{\text{ho}}$. Note that the Hamiltonian in Eq. (3.23) has the same form than the ubiquitous Jaynes-Cummings Hamiltonian in cavity QED [178, 181, 182]. Similarly, the blue sideband part of the Hamiltonian is of the form

$$H_{bs}'(t) = \frac{\hbar\Omega_{bs}}{2}\hat{\sigma}_+\hat{a}^\dagger e^{-i(\delta-\omega_{\text{ho}})} + \text{h.c},$$

(3.24)

which couples $|g,n\rangle \leftrightarrow |e,n+1\rangle$ states with Rabi frequency $\Omega_{bs} = \Omega_0\eta\sqrt{n+1}$ and resonance position $\delta = \omega_{\text{ho}}$. In Fig. 3.7(a), we show a sketch of the carrier, red sideband and blue sideband on the clock transition in an optical lattice. In an optical lattice of finite depth,
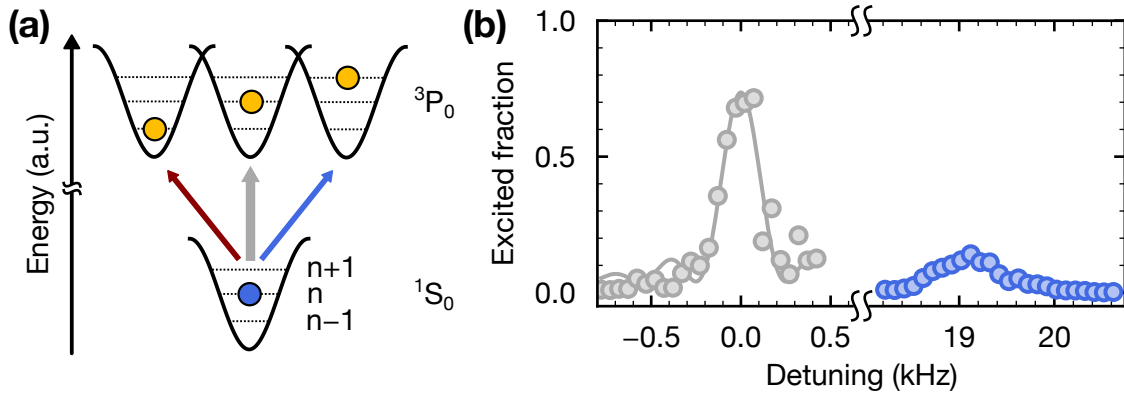
Figure 3.7 – **Sideband-resolved clock-line spectroscopy in the Lamb-Dicke regime in an optical lattice.**
(a) Clock transition sketched in a deep optical lattice, in the sideband-resolved regime. We show an atom in the energy band n driven to the band n (gray arrow, carrier), $n - 1$ (red arrow, red sideband) and $n + 1$ (blue arrow, blue sideband). The energy shifts with respect to the bare $^1S_0 \rightarrow ^3P_0$ transition are determined by the corresponding band gaps. Solid black lines represent the optical lattice trapping potential while dashed black lines indicate the energy level of each lattice band. **(b)** Clock-line spectroscopy measurement in a magic-wavelength optical lattice along the clock excitation pulse propagation direction, using a spin-polarized sample. We distinguish two peaks, corresponding to the carrier ($n : 0 \rightarrow 0$, gray dots) and first blue sideband ($n : 0 \rightarrow 1$, blue dots). Solid lines correspond to fits to the data using Eq. (3.17). The shift in energy between the carrier and the sideband is equal to the band gap and is $19.10(3)\,\text{kHz}$. This corresponds to a lattice depth of $28.14(7)\,E_{\text{rec}}$, where E_{rec} denotes the lattice photon recoil energy. In a separate measurement, we have verified that no feature corresponding to the first red sideband is observed, indicating that nearly all atoms are initially prepared in the lowest energy band $n = 0$ of the lattice.

the energy shift of the sidebands is not exactly given by ω_{ho}, but rather by the energy gap between the band n and $n \pm 1$. Furthermore, while strongly suppressed in the Lamb-Dicke regime, higher-order sideband transitions $|g, n\rangle \leftrightarrow |e, n \pm m\rangle$ with $m > 1$ are in practice still possible, with $\Omega_{n \leftrightarrow m} \propto \eta^{|n-m|}$ [183].

Using Eq. (2.39) to compute ω_{ho} allows us to greatly simplify the expression for the Lamb-Dicke parameter in our lattice to

$$\eta = \left(\frac{1}{4s}\right)^{1/4}, \tag{3.25}$$

which only depends on the lattice depth s in units of the lattice photon recoil energy, E_{rec}. In our experiments, we typically work with $s \approx 30$ along each lattice axis, corresponding to

$$\eta \approx 0.3, \tag{3.26}$$

which is well into the Lamb-Dicke regime. Furthermore, the energy gap between the ground and first excited lattice band can be numerically computed following the method shown in Section 2.3.1, leading to a value of $19.83\,\text{kHz}$ for $s = 30$. This can be very well resolved by means of clock-line spectroscopy, allowing us to work in the so-called resolved-sideband regime. A typical example of a clock-line spectroscopy measurement performed along one of our lattice axes is shown in Fig. 3.7(b). We observe two features corresponding to the carrier and first blue sideband resonances. The internal and motional degrees of freedom are

perfectly separated and both resonances can be readily described using the results derived in Section 3.3.1 up to the modified Rabi frequency for sidebands. No feature corresponding to the first red sideband resonance is observed, indicating that no significant amount of atoms is prepared in higher lattice bands with $n > 0$.

3.3.3 The magic wavelength

In Section 3.3.2, we have shown how to perform Doppler-free clock-line spectroscopy measurements by quantizing the motional degree of freedom of the atoms. This is done by subjecting them to an external optical lattice potential. In the derivation of the Rabi solution in Eq. (3.15), though, we only have taken into account the atomic internal energy levels as well as the near-resonant light field driving the transition. Considering the additional light field generating the optical lattice, atoms in an electronic state i experience an ac Stark shift [184]

$$U_{\mathrm{ac},i}(\mathbf{r}) = -\frac{1}{2\epsilon_0 c} \Re\left[\alpha_i(\lambda_L)\right] I_L(\mathbf{r}), \tag{3.27}$$

where $\Re\left[\alpha_i(\lambda_L)\right]$ is the real part of the dynamic polarizability of an atom for a given trapping light wavelength λ_L. In general, the intensity $I_L(\mathbf{r})$ of the trapping light is spatially inhomogeneous since it is generated by a laser beam, which usually exhibits a near-Gaussian profile. This directly leads to an inhomogeneous ac Stark shift, which is a desirable feature because it leads to the dipole force $\nabla U_{\mathrm{ac},i}(\mathbf{r})$ trapping the atoms.

If we now consider the clock transition ${}^1\mathrm{S}_0 \to {}^3\mathrm{P}_0$, we see from Eq. (3.27) that the difference in polarizabilities $\Re\left[\alpha_{{}^3\mathrm{P}_0}(\lambda_L) - \alpha_{{}^1\mathrm{S}_0}(\lambda_L)\right]$ induces a differential light shift

$$\Delta U_{\mathrm{ac}}(\mathbf{r}) = -\frac{1}{2\epsilon_0 c} \Re\left[\alpha_{{}^3\mathrm{P}_0}(\lambda_L) - \alpha_{{}^1\mathrm{S}_0}(\lambda_L)\right] I_L(\mathbf{r}) \tag{3.28}$$

between both states which has two main unfavourable consequences. First, it shifts the frequency of the clock transition by an amount $\Delta U_{\mathrm{ac}}(\mathbf{r})/2\pi\hbar$, which has to be taken into account for a correct addressing of the transition. Second, the inhomogeneity of the light shift broadens the line since the atomic cloud samples a large enough region of the trap to experience a significant variation in $I(\mathbf{r})$. This is harmful to the precision of clock-line spectroscopy measurements and furthermore leads to the dephasing of both states because of atomic motion in the trap, which couples the atomic internal and external degrees of freedom since the light field is inhomogeneous [6].

A solution to this problem is to design a trap where both states shift equally in energy, making it state-insensitive. A straightforward way to achieve this is to find a wavelength λ_{m} at which both states have equal polarizabilities, such that

$$\Re\left[\alpha_{{}^3\mathrm{P}_0}(\lambda_{\mathrm{m}})\right] = \Re\left[\alpha_{{}^1\mathrm{S}_0}(\lambda_{\mathrm{m}})\right]. \tag{3.29}$$

Such a wavelength is called magic wavelength [177, 185] and is a fundamental building block of state-of-the-art optical atomic clocks [6]. For ${}^{171}\mathrm{Yb}$, a magic wavelength has been reported in Ref. [186] with the value

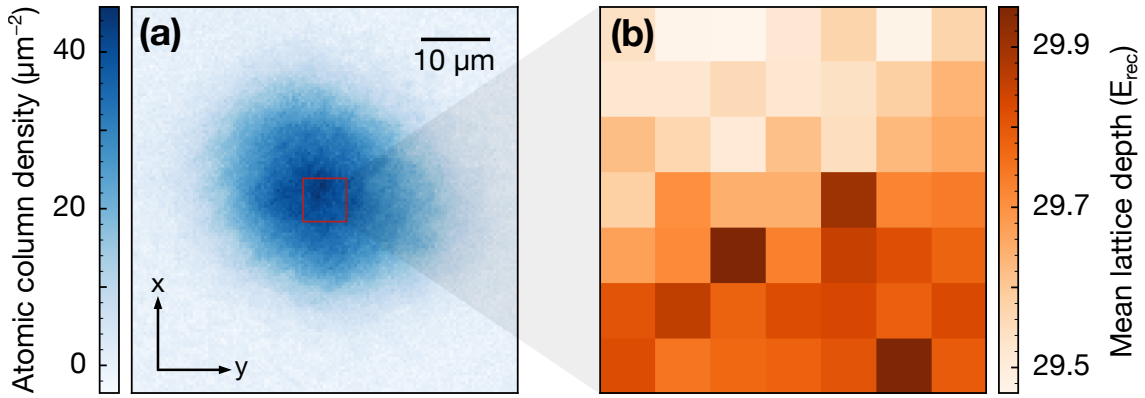$$\lambda_{\mathrm{m}} = 759.355944\,(19)\ \mathrm{nm}. \tag{3.30}$$

Figure 3.8 – **Spatially-resolved lattice depth calibration with clock-line sideband spectroscopy. (a)** In-situ column density of ^{171}Yb atoms in a cubic optical lattice measured with absorption imaging. The central red square denotes the $6.58\,\mu\text{m} \times 6.58\,\mu\text{m}$ (14×14 pixels) region of interest (ROI) in which the lattice depth is calibrated. **(b)** Mean lattice depth in units of the lattice photon recoil energy E_{rec} inside the ROI. It is computed after measuring the band gap along all three lattice axes via clock-line sideband spectroscopy. We show the value obtained in each $0.94\,\mu\text{m} \times 0.94\,\mu\text{m}$ (2×2 pixels) square inside the ROI. The lattice depth variation inside the ROI is about 1%. Adapted from Ref. [188].

In our experiments, we therefore always operate the optical lattice beams at the above mentioned wavelength λ_{m} unless stated otherwise, using a wavemeter as reference with a precision of $\sim 10\,\text{MHz}$. In such a lattice, the results from Sections 3.3.1 and 3.3.2 can be applied to evaluate our data without further considerations.

3.3.4 Spatially-resolved lattice depth calibration

When performing clock-line sideband spectroscopy, we typically measure the frequency of the carrier and of the first blue sideband. The difference between both frequencies is equal to the lowest lattice band gap. The energy band calculation presented in Section 2.3.1 can therefore be inverted to obtain the lattice depth. This provides us with an alternative procedure to calibrate our optical lattice compared to the standard method relying on parametric excitations via periodic lattice depth modulation [187], with the noticeable advantage that the high spatial resolution of our in-situ imaging system as well as the narrow linewidth of our clock laser can be exploited. The precision of the measurement is limited by the spatial inhomogeneity of the lattice depth over the cloud size, which effectively broadens the blue sideband line as visible in Fig. 3.7(b).

To reduce the effect of lattice inhomogeneity, we restrict our data evaluation to small sub-regions within our absorption images, as shown in Fig. 3.8(a). In the cloud center, where the atomic column density is the largest, we are able to determine the lattice depth in areas as small as $0.94\,\mu\text{m} \times 0.94\,\mu\text{m}$, corresponding to 2×2 pixels on our camera sensor. We can therefore perform a spatially-resolved lattice depth calibration with a resolution solely limited by our imaging system. Each axis $i = x, y, z$ of our cubic lattice is characterized by means

of clock-line sideband spectroscopy using a clock laser pulse propagating along i, leading to a lattice depth V_i. The mean lattice depth $\bar{V} = \left(V_x V_y V_z\right)^{1/3}$, which is a crucial experimental parameter in our experiments since it determines the on-site pair interaction energy in the lattice, is then obtained by combining the measurements along all axes. In Fig. 3.8(b), we show an example of a spatially-resolved lattice depth calibration in the center of our atomic cloud. The lattice inhomogeneity can clearly be seen, highlighting the relevance of this calibration method.

This technique is used to calibrate the optical lattice in all experiments presented in the following chapters. It is particularly relevant for the precise measurement of the interorbital scattering lengths presented in Section 4.2. On one hand, only considering small areas in the cloud center as shown in Fig. 3.8(b) narrows down the $|gg\rangle \rightarrow |eg\rangle$ lines, improving for instance the measurement precision of the on-site interaction energies $U_{eg}^{\pm}$. On the other hand, this improves the signal-to-noise ratio of pair-state spectroscopic features, owing to the larger fraction of doubly-occupied lattice sites. In fact, while the absolute temperature T can be considered constant over the entire sample, the Fermi temperature T_F is larger in the cloud center owing to the larger atomic density. The doublon fraction, which depends on the ratio T/T_F in a cubic lattice [189], is therefore larger in the cloud center.

3.4   Differential and quadratic Zeeman shifts

In general, the hyperfine states m_F of an alkaline-earth(-like) atom in the electronic ground state $^1S_0$ or clock state $^3P_0$ are shifted in energy at finite magnetic fields, owing to the Zeeman effect. For fermionic isotopes, the Landé g factor in $^1S_0$ atoms is different from the one in $^3P_0$ atoms, causing atoms in both electronic states to undergo different first-order Zeeman shifts. The clock transition frequency is therefore sensitive to the external magnetic field, which involves a splitting of the different $|^1S_0, m_F\rangle \rightarrow |^3P_0, m_F'\rangle$ transition frequencies. This defines the so-called differential Zeeman shift, which is a crucial effect to take into account when performing clock-line spectroscopy, in particular for the operation of state-of-the-art atomic clock experiments. When the differential Zeeman shift is large compared to the linewidth, the different spin components of a gas can be individually addressed. This provides an advantageous tool to state-selectively prepare and probe experimental samples. The differential Zeeman shift also plays a critical role in the interorbital interactions since it mixes the pair states $|eg^{\pm}\rangle$ defined in Eq. (2.17) and lies at the heart of the orbital Feshbach resonance mechanism described in Section 2.2.4. In addition to the (linear) differential Zeeman shift, the second-order Zeeman shift also has to be considered for precise clock-line spectroscopy at larger magnetic fields.

In this section, we explain the working principle of the differential and quadratic Zeeman shifts and precisely characterize them in ^{171}Yb by means of clock-line spectroscopy measurements in a magic-wavelength optical lattice.

3.4.1   Differential Zeeman shift

To first order, the energy of an atom in the state m_F undergoes a magnetic field-induced shift $\Delta E(B)$ given by

$$\Delta E(B) = \mu_B g m_F B, \tag{3.31}$$

where μ_B is the Bohr magneton, B the external magnetic field and g the Landé g-factor of the atom. For atoms in the electronic ground state $^1S_0$, the g-factor is given by the nuclear g-factor $g_I = \mu \mu_N / |I| \mu_B$, where μ is the nuclear magnetic moment, μ_N the nuclear magneton and I the nuclear spin quantum number. In the particular case of ^{171}Yb, $I = 1/2$ and $\mu = 0.4919 \mu_N$ [190], leading to $g_I = 749.91 \, h \, \text{Hz}/(G\mu_B)$. For fermionic isotopes, which have finite nuclear spin, however, the wavefunction in the clock state $^3P_0$ is modified by the hyperfine interaction-induced mixing with the $^3P_1$ and $^1P_1$ states [140, 191]. This causes a modification of the $^3P_0$ g-factor and defines the differential Zeeman shift

$$\delta g = g_{^3P_0} - g_{^1S_0} \tag{3.32}$$

as the difference between the g-factor of atoms in the $^3P_0$ and $^1S_0$ state, respectively. The key consequence of the existence of a differential Zeeman shift $\delta g \neq 0$ is that the clock transition frequency undergoes a linear shift $\Delta \nu^{(1)}(B) = \left(\Delta E_{^3P_0}(B) - \Delta E_{^1S_0}(B) \right) / 2\pi\hbar$ at finite magnetic fields B, as can be read from Eq. (3.31). For π transitions driven with a linearly polarized light field ($m_F \rightarrow m_F$), the shift is given by

$$\Delta \nu^{(1)}(B, m_F \rightarrow m_F) = \frac{\mu_B B}{2\pi\hbar} m_F \delta g, \tag{3.33}$$

whereas for $\sigma^\pm$ transitions driven with circularly polarized light ($m_F \rightarrow m_F \pm 1$), the shift is given by

$$\Delta \nu^{(1)}(B, m_F \rightarrow m_F \pm 1) = \frac{\mu_B B}{2\pi\hbar} \left[(m_F \pm 1)\delta g \pm g_I \right]. \tag{3.34}$$

Combining Eqs. (3.33) and (3.34), the result can be generalized to a transition from a hyperfine state m_F to $m_{F'}$ where the differential (linear) shift can be expressed as

$$\Delta \nu^{(1)}(B, m_F \rightarrow m_{F'}) = \frac{\mu_B B}{2\pi\hbar} \left[(m_F - m_{F'})g_I + m_{F'}\delta g \right]. \tag{3.35}$$

Eq. (3.35) shows that the differential Zeeman shift lifts the degeneracy of the transition frequency between different hyperfine states m_F at finite magnetic fields.

3.4.2   Quadratic Zeeman shift

To accurately address the clock transition at larger magnetic fields, the second-order Zeeman shift also needs to be considered. For the clock transition in alkaline-earth(-like) atoms involving states with $J = 0$, there is no contribution to the quadratic Zeeman shift from nearby hyperfine states. Instead, the shift arises from states separated in energy by fine-structure splitting, with a dominant contribution from the $^3P_0$ and $^3P_1$ states since the ground state

is separated from all other states by optical frequencies [6, 140]. In general, the resulting quadratic frequency shift of the clock transition takes the form [192]

$$\Delta \nu^{(2)}(B) = \beta B^2, \tag{3.36}$$

which is independent of the hyperfine states involved in the transition and defines the quadratic shift coefficient β. In particular, unlike the differential Zeeman shift, the quadratic Zeeman shift leaves the energy splitting between different hyperfine states unchanged. Summing up the first and second-order Zeeman shift contributions in Eq. (3.35) and Eq. (3.36) yields the total magnetic field-dependent frequency shift of the clock transition

$$\Delta \nu(B, m_F \rightarrow m_{F'}) = \frac{\mu_B B}{2\pi\hbar} \left[(m_F - m_{F'}) g_I + m_{F'} \delta g \right] + \beta B^2, \tag{3.37}$$

where δg and β are the two coefficients that have to be determined experimentally.

3.4.3 Measurement of the differential and quadratic Zeeman shifts

Since both electronic states $^1S_0$ and $^3P_0$ in ^{171}Yb have $F = 1/2$, there only are four different clock transitions with frequency $\nu(B, m_F \rightarrow m_{F'})$. We define for simplicity

$$
\begin{aligned}
\nu_1(B) &\equiv \nu(B, +1/2 \rightarrow +1/2), &\quad \nu_2(B) &\equiv \nu(B, -1/2 \rightarrow -1/2), \\
\nu_3(B) &\equiv \nu(B, +1/2 \rightarrow -1/2), &\quad \nu_4(B) &\equiv \nu(B, -1/2 \rightarrow +1/2),
\end{aligned}
\tag{3.38}
$$

which are illustrated in Fig. 3.9(a). To experimentally determine the coefficients δg and β in Eq. (3.37), we measure the frequency of each single-particle transition $\nu_i(B)$ at various magnetic fields up to $B = 600\,$G, see Fig. 3.9(b). A spin-polarized sample in the electronic ground state $^1S_0$ and initial hyperfine state m_F is first prepared by means of optical pumping. The atoms are then loaded into the ground band of a $\approx 30\,E_{\text{rec}}$ deep cubic optical lattice operating at the magic wavelength and the external magnetic field B is ramped to the desired value. Atoms are then directly driven from $|^1S_0, m_F\rangle$ to $|^3P_0, m_{F'}\rangle$ and the response of the system as a function of the driving frequency is probed. We fit individual Rabi lineshapes [see Eq. (3.17)] to extract the frequency of each transition $\nu_i(B)$ at various magnetic fields, as shown in Fig. 3.9(b).

Differential Zeeman shift

The main motivation behind measuring both π and $\sigma^{\pm}$ transitions is that it allows for the determination of the differential Zeeman shift without any prior calibration of the magnetic field [6, 140]. First, we get access to the purely linear differential Zeeman shift by using $\Delta^{(1)}\nu_{1,2} = \nu_{1,2} - (\nu_1 + \nu_2)/2$ and $\Delta^{(1)}\nu_{3,4} = \nu_{3,4} - (\nu_3 + \nu_4)/2$, which removes all non-linear shifts and cancels long-term drifts of the clock laser. Combining all transition frequencies and with the help of Eq. (3.35), the magnetic field can be self-calibrated by computing

$$B = \frac{\pi\hbar}{\mu_B g_I} \left[\Delta^{(1)}\nu_1(B) + \Delta^{(1)}\nu_3(B) - \Delta^{(1)}\nu_2(B) - \Delta^{(1)}\nu_4(B) \right], \tag{3.39}$$
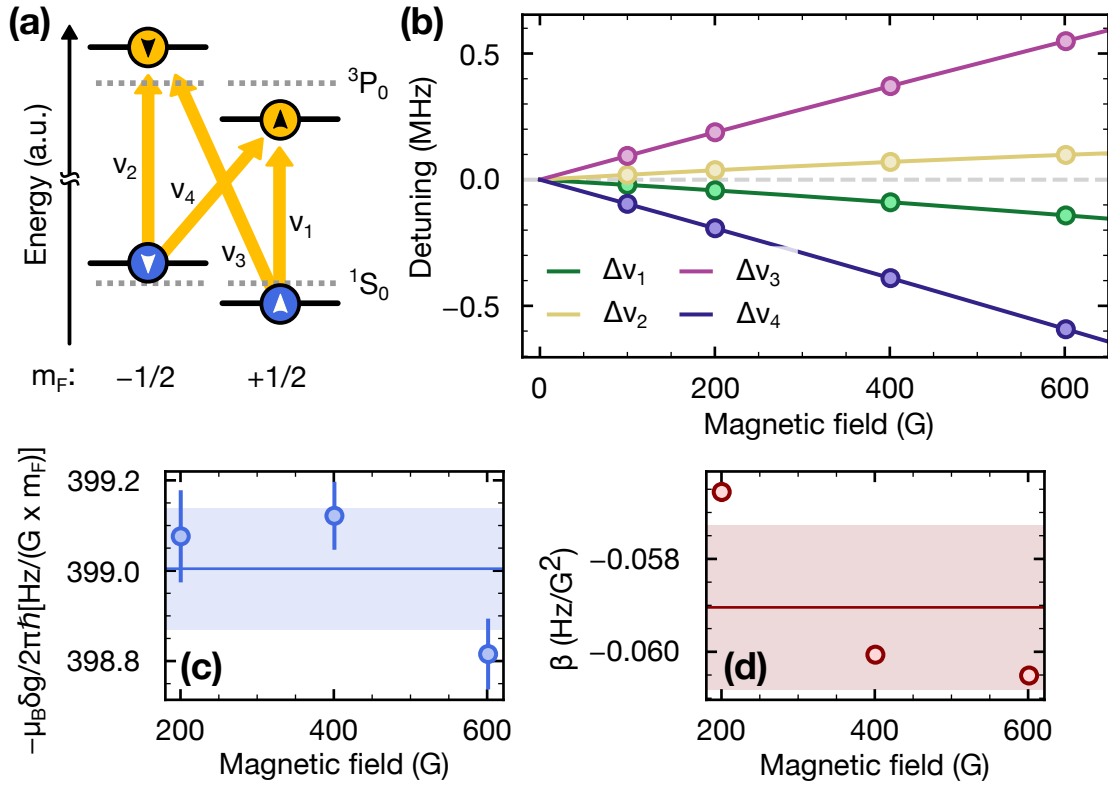
Figure 3.9 – **Differential and quadratic Zeeman shifts on the ^{171}Yb clock transition. (a)** Relevant energy levels for the clock transition sketched at zero (dotted grey lines) and finite magnetic field (solid black lines) (not to scale). The yellow arrows illustrate the four transitions ν_i defined in Eq. (3.38). **(b)** Detuning $\Delta\nu_i(B)$ of each clock transition $\nu_i(B)$ with respect to the $B = 0$ case (dashed grey line). All data points are obtained by fits to clock-line spectroscopy measurements described in the main text. The error bars denote the fit uncertainty of individual lineshapes and are much smaller than the marker size. We use Eq. (3.39) to determine the magnetic field B independently of any prior calibration. Solid lines represent the detunings obtained via Eq. (3.37), using the differential and quadratic Zeeman shifts obtained in (c) and (d). **(c)-(d)** Characterization of the first- and second-order Zeeman shift, respectively. For each magnetic field B, we extract the detunings $\Delta\nu_i(B)$ and use Eqs. (3.40) and (3.42) to compute δg and β, respectively. The error bars are computed using the fit uncertainty on $\Delta\nu_i(B)$. The horizontal lines denote the mean value of the three data points while the colored area spans over their standard deviation. Adapted from [188].

assuming all transitions frequencies have been measured at the exact same magnetic field. The differential Zeeman shift δg is finally computed using Eqs. (3.35) and (3.39), leading to

$$\delta g = \frac{2\pi\hbar}{\mu_B B} \left[\Delta^{(1)} \nu_1(B) - \Delta^{(1)} \nu_2(B) \right] = \frac{2g_I}{1 + \left[\dfrac{\Delta^{(1)} \nu_3(B) - \Delta^{(1)} \nu_4(B)}{\Delta^{(1)} \nu_1(B) - \Delta^{(1)} \nu_2(B)} \right]}, \tag{3.40}$$

which is indeed independent from the explicit value B of the magnetic field. This method has been successfully applied to determine the differential Zeeman shift in [87]Sr [140], [171]Yb [193] and [173]Yb [118]. We compute the differential Zeeman shift using Eq. (3.40) for $B = 200$, 400 and 600 G using our experimental data, see Fig. 3.9(c). Taking the mean and standard deviation of all three values, we find

$$\delta g = -399.0\,(1)\,h\,\mathrm{Hz}/\left(\mathrm{G}\mu_B m_F\right), \tag{3.41}$$

which induces a magnetic field-dependent linear frequency splitting of $\delta(B) = 399\,(1) \times B$ Hz between both π transitions $|^1S_0, m_F\rangle \rightarrow |^3P_0, m_F\rangle$. This value is in good agreement with previous results obtained for [171]Yb [193, 194].

Quadratic Zeeman shift

We also determine the quadratic Zeeman shift in a fashion similar to the differential shift. Using $\Delta \nu_i(B) = \nu_i(B) - \nu_i(B = 0)$ and Eq. (3.37), one obtains

$$\beta = \frac{\Delta \nu_1(B) + \Delta \nu_2(B) + \Delta \nu_3(B) + \Delta \nu_4(B)}{B^2}, \tag{3.42}$$

where the magnetic field B is computed via Eq. (3.39). This expression neglects higher-order contributions to the Zeeman shift as well as long-term drifts of the clock laser. We compute the quadratic Zeeman shift using Eq. (3.42) for again $B = 200$, 400 and 600 G using our experimental data, see 3.9(d). Taking the mean and standard deviation of all three values, we obtain

$$\beta = -0.059\,(2)\,\mathrm{Hz}/\mathrm{G}^2, \tag{3.43}$$

which is in good agreement with theoretical predictions [192] as well as previous measurements [186, 195] for Yb.

Knowing δg and β, we have used Eq. (3.37) to calibrate the magnetic field B generated by our coils as a function of the output current I of our power supplies. In particular, we have verified that the magnetic field is proportional to the current and have extracted the proportionality factor for each relevant combination of coils and power supplies, using data sets such as the one shown in Fig. 3.9(b).

Characterization of interorbital interactions in ^{171}Yb

When considering two-orbital Fermi-Hubbard models realized with ^{171}Yb atoms featuring orbital as well as nuclear spin degrees of freedom in optical lattices, two-body interactions between different atomic pairs play a key role. Of particular importance is the elastic scattering between interorbital pair states, which gives rise to spin-exchange interactions. These interactions lie at the heart of orbital quantum magnetism, which includes iconic models such as the Kondo lattice model [64, 98] or the Kugel-Khomskii model [196]. Alkaline-earth(-like) atoms such as ^{171}Yb therefore appear as promising potential candidates for the investigation of these models [69, 82–84, 197]. In that case, inelastic scattering processes are also critical, since they can limit the lifetime of certain states in the experimental sample, leading to a detrimental loss of atoms.

In this chapter, we report on the full characterization of intra- as well as interorbital interactions in ^{171}Yb by probing pair states on individual sites of a magic-wavelength optical lattice. We precisely measure the s-wave scattering lengths associated with the intraorbital superposition states as well as the interorbital scattering length associated with pairs of atoms in the clock state by means of clock-line spectroscopy, similarly to the method introduced in Ref. [73]. Furthermore, we investigate the effect of inelastic scattering in these states by extracting the associated two-body loss coefficients from lifetime measurements.

4.1 Experimental configuration and sequence

Most of the experiments presented throughout this thesis are performed in a three-dimensional isotropic cubic optical lattice operating at the magic wavelength $\lambda_{\mathrm{m}} = 759\,\mathrm{nm}$, as illustrated in Fig. 4.1(a). The three lattice axes are generated by three retroreflected orthogonal laser beams, each with a typical lattice depth of $30\,E_{\mathrm{rec}}$. Here $E_{\mathrm{rec}} = (2\pi\hbar)^2/2m\lambda_{\mathrm{m}}$ denotes the lattice photon recoil energy, with m the atomic mass. In our experiments, we typically work with either spin-balanced samples ($m_F = \pm 1/2$) or spin-polarized gases ($m_F = -1/2$ or $m_F = +1/2$). Our samples generally have a temperature $T \approx 0.25\,T_F$ before loading them from the optical dipole trap into the lattice, where T_F denotes the Fermi temperature of the gas. We therefore work in the deeply quantum degenerate regime, where all atoms can be assumed to be in the

lowest energy band of the lattice. Since there are two different possible nuclear spin states $m_F \in \{-1/2, +1/2\}$, every lattice site can only be populated with zero (hole), one (singlon) or two (doublon) atoms, owing to the Pauli exclusion principle. A yellow clock-excitation pulse is performed along the lattice axis L_1 in a vertical bias magnetic field B to drive singlons to $|e\rangle$ or doublons to the interorbital states $|\psi_{eg}^{\pm}(B)\rangle$ defined in Eq. (2.22). The clock laser is linearly polarized with a polarization aligned along B, such that only π transitions are driven.

A typical experimental sequence is sketched in Fig. 4.1(b). First, the atoms are transferred from the crossed optical dipole trap (xODT) into the optical lattice after having performed forced evaporative cooling (see Sec. 3.1.3). The HDT and the VDT are ramped down while the vertical lattice L_3 is ramped up to its final depth within 120 ms following an s-shaped ramp. The horizontal lattices L_1 and L_2 are subsequently ramped up to $3\,E_{\text{rec}}$ within 120 ms, and after that to their final depth within 150 ms. Such a sequence is designed to keep the lattice loading as adiabatic as possible by minimizing the mass redistribution during the ramp [153], and is identical to the one used to prepare ^{173}Yb atoms in the Mott-insulating phase at temperatures < $0.1\,T_F$ [89] with our apparatus. From clock-line spectroscopy measurements, we estimate that about 25% of the atoms are on doubly-occupied lattice sites, corresponding to a temperature in the lattice $\approx 0.8\,T_F$ and therefore a temperature $\lesssim 0.4\,T_F$ in the dipole trap before loading into the lattice [189]. The magnetic field B is then ramped up within 75 ms to the the desired value and the sample is probed or prepared with a coherent clock-laser π-pulse after a 500 ms hold time used to allow the magnetic field to stabilize. Finally, the population in $|g\rangle$ and in $|e\rangle$ are separately imaged in situ, following the procedure described in Section 3.2.2.

Throughout this chapter, we mainly probe four different clock-line transitions, namely both single-particle transitions

$$
\begin{aligned}
|g\downarrow\rangle &\rightarrow |e\downarrow\rangle \\
|g\uparrow\rangle &\rightarrow |e\uparrow\rangle
\end{aligned}
\tag{4.1}
$$

as well as both two-particle transitions[1]

$$
\begin{aligned}
|gg\rangle &\rightarrow |\psi_{eg}^{-}(B)\rangle \\
|gg\rangle &\rightarrow |\psi_{eg}^{+}(B)\rangle,
\end{aligned}
\tag{4.2}
$$

as illustrated in Fig. 4.1(c). Here, we have used the notations $|^1S_0\rangle \equiv |g\rangle$, $|^3P_0\rangle \equiv |e\rangle$, $|m_F = -1/2\rangle \equiv |\downarrow\rangle$ and $|m_F = +1/2\rangle \equiv |\uparrow\rangle$ to describe the internal state of single atoms.

At $B = 0$, the interorbital states are given by $|eg^{\pm}\rangle$ defined in Eq. (2.17) while in the limit $|\delta(B)| \gg |V_{\text{ex}}|$ they are given by $|e\uparrow g\downarrow\rangle$ and $|e\downarrow g\uparrow\rangle$ defined in Eq. (2.23). Here, $\delta(B) = -399.0(1)\,\text{Hz/G} \times m_F B$ is the differential Zeeman shift determined in Section 3.4 and V_{ex} the spin-exchange interaction energy defined in Eq. (2.20). While single-particle transitions are driven with a Rabi frequency Ω_0, the coupling to the interorbital states $|\psi_{eg}^{\pm}(B)\rangle$ shows super-

---

[1]Note that since we use linearly polarized light to drive the clock transition, only the $|t\rangle = (|\uparrow\downarrow\rangle + |\downarrow\uparrow\rangle)/\sqrt{2}$ triplet spin state of $|eg^-\rangle$ is addressed, with the other two possible spin states $|\uparrow\uparrow\rangle$ and $|\downarrow\downarrow\rangle$ remaining inaccessible.
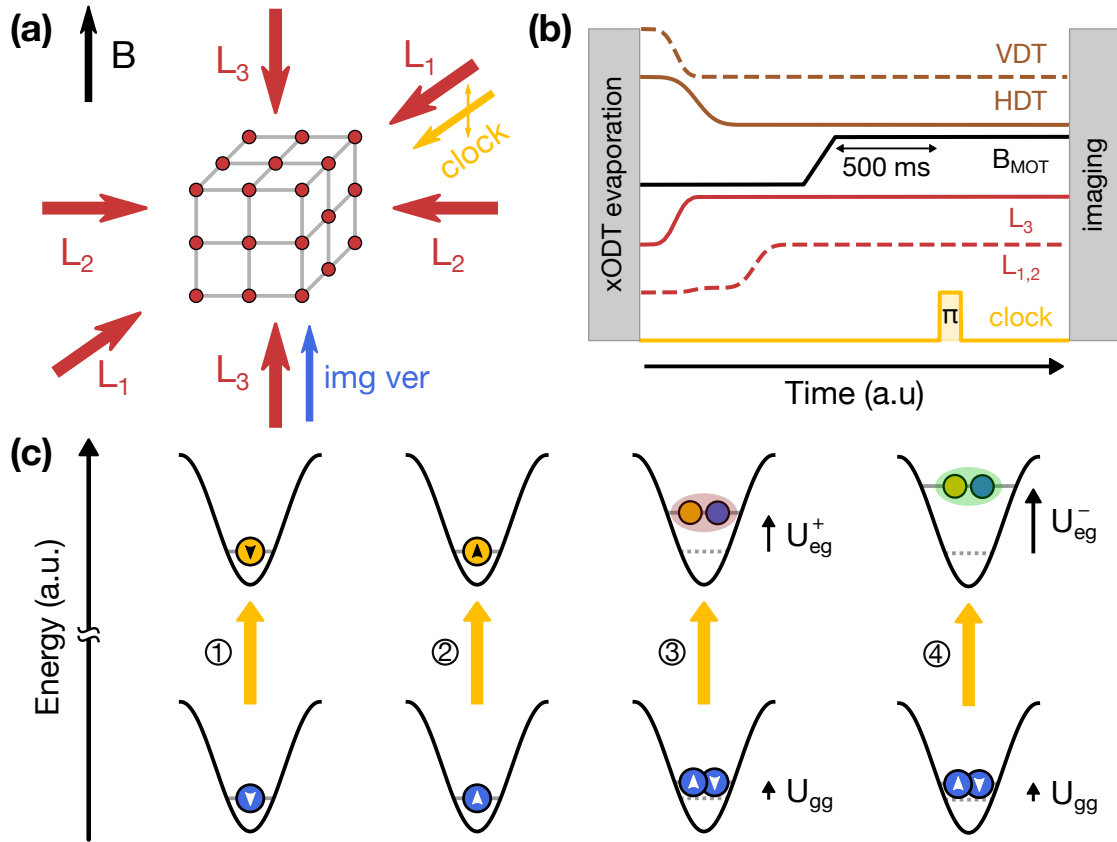
Figure 4.1 – **Experimental sequence and geometry. (a)** Sketch of the experimental geometry. We prepare a spin-balanced quantum degenerate Fermi gas of ^{171}Yb in a magic-wavelength isotropic cubic optical lattice and vertical bias magnetic field B. The lattice potential is generated by the three perpendicular retroreflected laser beams L_1, L_2 and L_3, as introduced in Fig. 3.1. Red circles represent individual lattice sites while gray lines denote nearest-neighbor tunnel links. Each lattice site can be populated with a maximum of two atoms in the ground band, owing to the Pauli exclusion principle and the presence of two different spin states. The laser employed to drive ground-state atoms to the clock state is co-propagating with L_1 and linearly polarized along B. At the end of each experimental cycle, in-situ imaging of the atoms is performed using a vertical imaging laser beam. **(b)** Experimental sequence. After forced evaporation in the xODT [see Fig. 3.2(b)], atoms are first transferred into the vertical lattice planes in L_3 before ramping up the horizontal lattices L_1 and L_2. The bias magnetic field B is subsequently ramped up to the desired value, after which a clock-excitation π-pulse is performed to probe or prepare the sample. The atoms are finally imaged following the sequence described in Fig. 3.3(c). **(c)** Relevant single- and two-particle transitions on the clock line represented for $B = 0$ G. We either drive the single-particle transitions ①: $|g\downarrow\rangle \rightarrow |e\downarrow\rangle$ and ②: $|g\uparrow\rangle \rightarrow |e\uparrow\rangle$ or the two-particle transitions ③: $|gg\rangle \rightarrow |eg^+\rangle$ and ④: $|gg\rangle \rightarrow |eg^-\rangle$. Solid black lines represent the on-site lattice potential while solid gray lines denote the energy of each state. Two-particle states are shifted in energy with respect to single-particle states by the on-site interaction energies U_{gg} and $U_{eg}^{\pm}$. At finite magnetic fields, the various transition energies are shifted with respect to the $B = 0$ case.

and subradiant behavior, with effective Rabi frequencies [152]

$$\frac{\Omega_{\text{eg}}^{\pm}(B)}{\Omega_0} = \frac{\mp 1 + C(B)}{C(B)}\sqrt{1 + \frac{V_{\text{ex}}^2}{\delta(B)^2}\left[1 \pm C(B)\right]}, \tag{4.3}$$

where $C(B) = \sqrt{1 + \delta(B)^2/V_{\text{ex}}^2}$. At $B = 0$, the coupling to $|eg^-\rangle$ is therefore enhanced by a factor $\sqrt{2}$ compared to the single-particle transition, while the coupling to $|eg^+\rangle$ vanishes. At finite magnetic fields, however, the mixing between $|eg^-\rangle$ and $|eg^+\rangle$ leads to a finite coupling to both interorbital states, with the limit $\Omega_{\text{eg}}^{\pm}(B)/\Omega_0 \to 1$ for large fields where $|\delta(B)| \gg |V_{\text{ex}}|$. In our experiments, we always take the modified coupling to $|\psi_{\text{eg}}^{\pm}(B)\rangle$ into account to choose the correct π-pulse time t_π.

4.2   Interorbital scattering lengths

In order to experimentally determine the interorbital scattering lengths $a_{\text{eg}}^{\pm}$ in ^{171}Yb, which are among the most critical parameters for the study of two-orbital Fermi-Hubbard Hamiltonians, we first measure the on-site interaction energies $U_{\text{eg}}^{\pm}$ associated with both interorbital states $|eg^{\pm}\rangle$ in a magic-wavelength optical lattice of mean depth $\bar{V} = 29.71\,(5)\,E_{\text{rec}}$. The experimental geometry and sequence correspond to the description in Section 4.1.

We perform clock-line spectroscopy measurements at various magnetic fields $B = \{1.1, \ldots, 50\}\,\text{G}$ on both pair transitions $|gg\rangle \to |\psi_{\text{eg}}^{\pm}(B)\rangle$ in spin-balanced samples, as shown in Fig. 4.2. The response of the system is probed as a function of the clock-laser detuning with respect to the single-particle transition frequency at zero magnetic field. This leads to the eigenenergies $E_{\pm}(B)$ of the interorbital states defined in Eq. (2.19) relatively to the initial-state on-site interaction energy U_{gg}. As a reference, we also measure in spin-polarized samples both single-particle transitions $|g\downarrow\rangle \to |e\downarrow\rangle$ and $|g\uparrow\rangle \to |e\uparrow\rangle$, which are affected by the differential Zeeman shift at finite magnetic fields. All four transitions are probed in an interleaved fashion at each magnetic field in order to keep track of clock laser drifts. The single-particle transitions are driven with coherent π-pulses of power $P = 15\,\mu\text{W}$ (corresponding to an intensity $I \approx 24\,\text{mW/cm}^2$) and duration $t_\pi = 3.972\,\text{ms}$. To keep the exact same coupling strength for the pair-state transitions, we adjust the clock-laser power P such that $P \to P\left[\Omega_0/\Omega_{\text{eg}}^{\pm}(B)\right]^2$, where Ω_0 is the single-particle transition Rabi frequency and $\Omega_{\text{eg}}^{\pm}(B)$ the two-particle transition Rabi frequencies defined in Eq. (4.3), ensuring a constant π-pulse time throughout our measurements. The only exceptions are the $|gg\rangle \to |\psi_{\text{eg}}^+\rangle$ transitions at $B = 1.1\,\text{G}$ and $B = 2.5\,\text{G}$ where longer pulse times have been used since available laser power was lacking to fully adjust the coupling strength.

We restrict the evaluation of our in-situ absorption images to a small region of interest (ROI) of $14\,\text{px} \times 14\,\text{px}$ (corresponding to $6.58\,\mu\text{m} \times 6.58\,\mu\text{m}$, or 17.33×17.33 lattice sites) in the center of the atomic cloud. We evaluate our data in each $2\,\text{px} \times 2\,\text{px}$ (corresponding to $0.94\,\mu\text{m} \times 0.94\,\mu\text{m}$) binned superpixel within the ROI, leading to a total of 49 independent measurements. At each magnetic field, every resonance is individually fitted with a Lorentzian profile, leading to the energy branches shown in Fig. 4.3. Using the resonance frequencies ex-
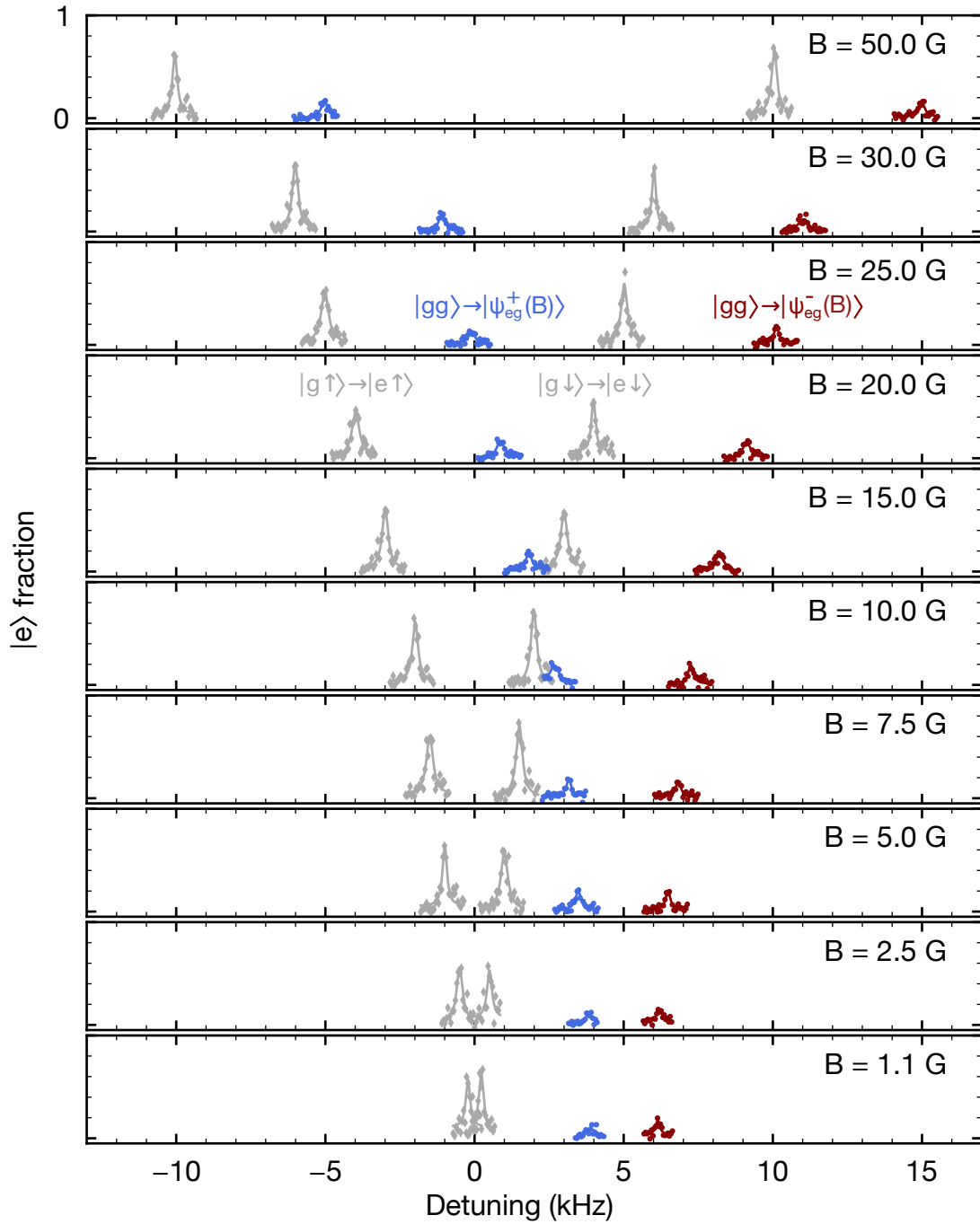
Figure 4.2 – Low-field interaction spectroscopy in ^{171}Yb. Clock-line spectroscopy measurements performed at multiple magnetic fields $B = \{1.1, \ldots 50\}$ G and evaluated in a $0.94\,\mu\text{m} \times 0.94\,\mu\text{m}$ large region of interest inside our in-situ absorption images. For each magnetic field, we show the fraction of atoms detected in the clock state as a function of the detuning of the driving laser with respect to the single-particle transition frequency at zero magnetic field. In addition to both single-particle transitions (gray diamonds), we observe two features corresponding to both two-particle transitions $|gg\rangle \to |\psi_{\text{eg}}^{+}(B)\rangle$ (blue circles) and $|gg\rangle \to |\psi_{\text{eg}}^{-}(B)\rangle$ (red circles). Solid lines denote Lorentzian fits to the data.

Figure 4.3 – **Interorbital interaction energies in ^{171}Yb.** We show the resonance position of both single-particle transitions (gray diamonds) and both two-particle transitions (circles) as a function of the magnetic field, extracted from fits to the data displayed i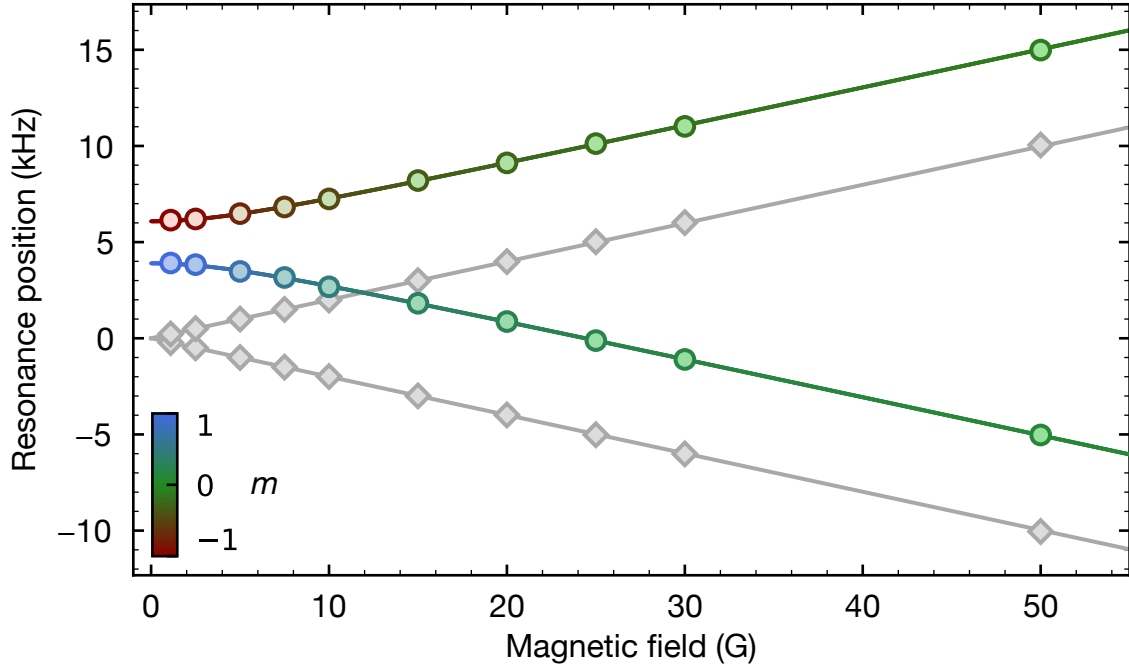n Fig. 4.2. The color of data corresponding to the interorbital interaction states is given at each magnetic field B by the parameter $m(B) = \left|\langle eg^+|\psi_{eg}^\pm(B)\rangle\right|^2 - \left|\langle eg^-|\psi_{eg}^\pm(B)\rangle\right|^2$. Using this definition, $m = -1$ corresponds to a pure $|eg^-\rangle$ state, $m = 1$ to a pure $|eg^+\rangle$ state and $m = 0$ to a perfect superposition state. Solid lines correspond to either the differential Zeeman shift computed using the values reported in Section 3.4 (gray) or to fits of Eq. (2.19) to the data (color). Error bars are smaller than the marker size. Adapted from Ref. [188].

tracted from the fits, we shift the clock-laser detuning such that the mean of both single-particle transition frequencies is set to zero. This cancels clock-laser drifts as well as contributions from the quadratic Zeeman shift. We notice that the pair-state energy corresponding to $|\psi_{eg}^-(B)\rangle$ is always larger than the one corresponding to $|\psi_{eg}^+(B)\rangle$. This implies a negative spin-exchange interaction energy $V_{ex} < 0$ as a consequence of Eq. (2.19) and demonstrates antiferromagnetic interorbital spin-exchange in ^{171}Yb, in agreement with similar measurements [194, 198].

In each superpixel inside the ROI, we fit the obtained energy branches $E_\pm(B)$ with

$$E_-(B) + E_+(B) = 2V$$
$$E_-(B) - E_+(B) = 2\sqrt{V_{ex}^2 + \delta(B)^2}, \tag{4.4}$$

which immediately follows from Eq. (2.19) and $V_{ex} < 0$, using V and V_{ex} as free fit parameters. Here, V denotes the direct interaction energy defined in Eq. (2.21) and $\delta(B)$ the differential Zeeman shift. Using Eqs. (2.20) and (2.21), the on-site interaction energies are then given by

$$U_{eg}^+ = V + V_{ex}$$
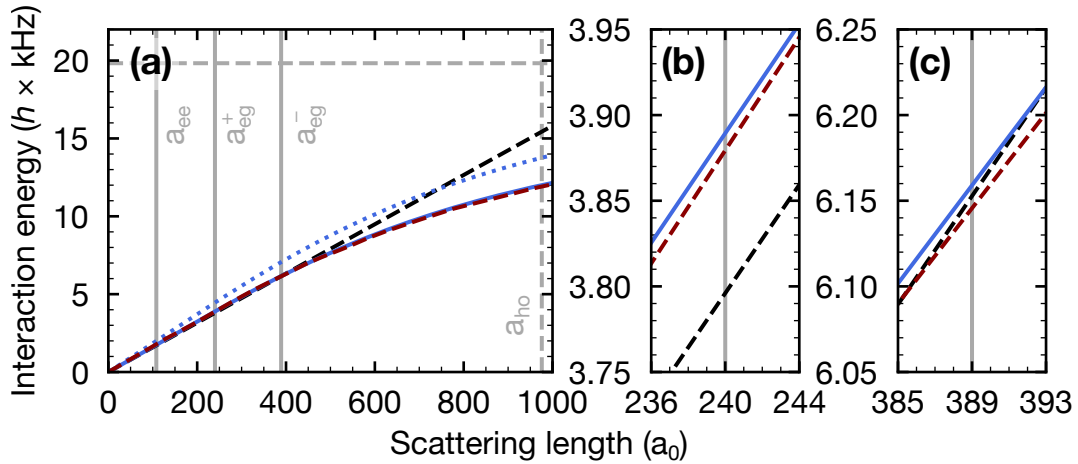$$U_{eg}^- = V - V_{ex}. \tag{4.5}$$

Figure 4.4 – **Comparison of models for the on-site interaction energy. (a)** We compare the on-site pair interaction energy as a function of the s-wave scattering length a in a $30\,E_\mathrm{rec}$ deep optical lattice using the various interaction models introduced in Section 2.4, where E_rec denotes the lattice photon recoil energy. The different lines represent the results obtained using: Eq. (2.49) with ground-band Wannier wavefunctions (black dashed line) as well as the harmonic oscillator solutions in Eq. (2.54) without (blue dotted line) and with (solid blue line) correction of the slope at $a = 0$ (see main text). The exact diagonalization solution computed in Ref. [74] applied to our data is shown as well for reference (red dashed line). Solid vertical gray lines correspond to the scattering lengths $a_\mathrm{eg}^{\pm}$ determined in this section and a_ee probed in Section 4.3. The dashed horizontal gray line denotes the lattice band gap and the dashed vertical gray line the corresponding harmonic oscillator length a_ho computed via Eq. (2.40). We also show detailed plots around **(b)** $a = 240\,a_0$ and **(c)** $a = 389\,a_0$, which correspond to the values of a_eg^{+} and a_eg^{-} determined in this section, respectively.

The final step is to compute the interorbital scattering lengths $a_\mathrm{eg}^{\pm}$ from the on-site interaction energies $U_\mathrm{eg}^{\pm}$ and lattice parameters. In Fig. 4.4, a comparison between the various models introduced in Section 2.4 to describe the pair-state interaction energy as a function of the s-wave scattering length is shown for a lattice of depth $30\,E_\mathrm{rec}$, where E_rec represents the lattice photon recoil energy.

A first approach consists in considering two indistinguishable particles on a single lattice site interacting via the pseudopotential $V(\mathbf{r}) = \left(4\pi\hbar^2 a/m\right)\delta^{(3)}(\mathbf{r})$, where $\mathbf{r}$ is the interparticle distance, a the s-wave scattering length and m the atomic mass. This leads to the Hubbard on-site interaction energy U defined in Eq. (2.49). In a simple approximation, one could assume that the atomic wavefunction in Eq. (2.49) is given by the lowest-lattice-band Wannier function $w_0(r)$, yielding the model used in Refs. [194, 198] to compute the interorbital scattering lengths from the measured on-site interaction energies (dashed black lines in Fig. 4.4). This is however only valid in the limit of deep lattices and small scattering lengths, where contributions from higher bands are negligible. In order to better account for these contributions, we instead use the exact energy solution for two atoms in a harmonic trap, see Eq. (2.54) (dotted blue line in Fig. 4.4). The anharmonicity of the on-site trapping potential is accounted for by matching the slope of the obtained energy branch at $a = 0$ with the slope obtained from using Eq. (2.49) with ground-band Wannier functions (solid blue lines in Fig. 4.4). This leads to results in excellent agreement with an exact diagonalization of the Hamiltonian describing
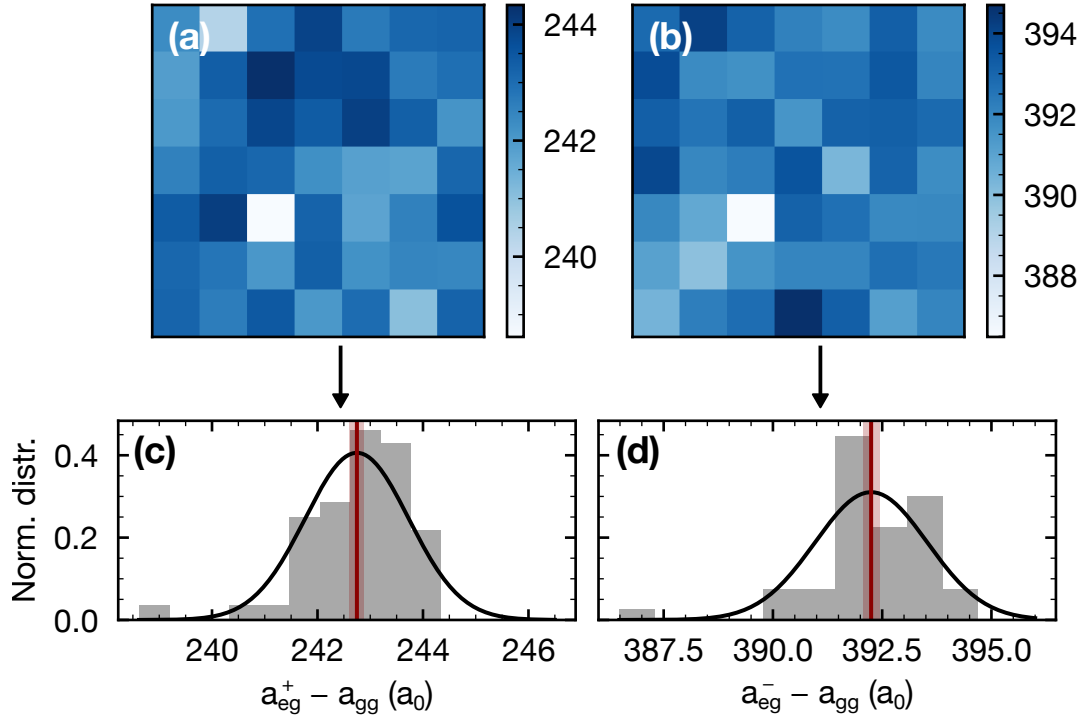
Figure 4.5 – Interorbital scattering lengths distribution in the cloud center. From the spatially-resolved measurement of the on-site interaction energies $U_{\text{eg}}^{\pm} - U_{\text{gg}}$ and of the mean lattice depth [see Fig. 3.8(b)], we compute the relative interorbital scattering lengths **(a)** $a_{\text{eg}}^{+} - a_{\text{gg}}$ and **(b)** $a_{\text{eg}}^{-} - a_{\text{gg}}$ in each $0.94\,\mu\text{m} \times 0.94\,\mu\text{m}$ binned superpixel within our region of interest using the method described in the main text. **(c-d)** Normalized weighted distribution of the relative interorbital scattering lengths displayed in **(a)** and **(b)**, respectively. We use the number of atoms in each superpixel as weights. Solid black lines represent Gaussian fits to the distribution, while solid red lines denote the mean of the distribution, leading to the values reported in the main text. The red shaded area coincides with the standard error of the mean. Adapted from Ref. [188].

two interacting atoms in a lattice, expanding the lattice potential to 10th order [74] (dashed red lines in Fig. 4.4).

In each binned superpixel inside the ROI, we compute the relative interorbital scattering lengths $a_{\text{eg}}^{\pm} - a_{\text{gg}}$ using the measured relative on-site interaction energies $U_{\text{eg}}^{\pm} - U_{\text{gg}}$ and the spatially-resolved mean lattice depth calibration shown in Fig. 3.8(b). The obtained $a_{\text{eg}}^{\pm}$ are displayed in Figs. 4.5(a-b) and show as expected no apparent spatial dependence, in contrast to $U_{\text{eg}}^{\pm} - U_{\text{gg}}$ or the mean lattice depth. This effectively leads to multiple independent measurements of $a_{\text{eg}}^{\pm}$ with outcomes following a distribution which we assume to be Gaussian, as shown in Figs. 4.5(c-d). Taking the mean value of the distribution leads to the relative scattering lengths

$$a_{\text{eg}}^{+} - a_{\text{gg}} = 242.7\,(1)\,a_0$$
$$a_{\text{eg}}^{-} - a_{\text{gg}} = 392.2\,(2)\,a_0,$$

(4.6)

where a_0 denotes the Bohr radius. The error is given by the fit uncertainty on the position of the mean. Using the previously measured value $a_{\text{gg}} = -2.8\,(3.6)$ [96] for the $|gg\rangle$ scattering

length, we finally obtain the absolute interorbital scattering lengths

$$
\begin{aligned}
a_{\text{eg}}^+ &= 240\,(4)\, a_0 \\
a_{\text{eg}}^- &= 389\,(4)\, a_0,
\end{aligned}
\tag{4.7}
$$

with an uncertainty dominated by the uncertainty on a_{gg} since the relative values in Eq. (4.6) exhibit uncertainties smaller by one order of magnitude. A measurement of a_{gg} with enhanced precision could therefore significantly reduce the uncertainties of $a_{\text{eg}}^\pm$. Note that using Eq. (2.49) with ground-band Wannier functions to extract the scattering lengths leads to $a_{\text{eg}}^+ - a_{\text{gg}} = 248.2\,(1)\, a_0$ and $a_{\text{eg}}^- - a_{\text{gg}} = 391.7\,(2)\, a_0$.

In particular, we find that $a_{\text{eg}}^+ < a_{\text{eg}}^-$, involving antiferromagnetic spin-exchange interactions with $V_{\text{ex}} < 0$, in qualitative agreement with similar measurements performed in ^{171}Yb [194, 198]. Considering the vanishingly small s-wave scattering length associated with $|gg\rangle$ pairs as well, this makes ^{171}Yb a very promising platform for the study of the antiferromagnetic Kondo and Kondo lattice models in particular [69, 78–84].

4.3 Intraorbital scattering length in the clock state

In order to complete the characterization of $^1\text{S}_0$–$^3\text{P}_0$ elastic scattering in ^{171}Yb, we measure the scattering length a_{ee} associated with the $|ee\rangle$ interaction channel, which has not yet been determined in this isotope. In principle, a_{ee} could be probed by directly driving the $|gg\rangle \rightarrow |ee\rangle$ transition in an optical lattice via two-photon excitations, in analogy to the measurement performed to determine a_{ee} in ^{173}Yb [73]. In this case, two clock-laser photons of identical frequencies are simultaneously absorbed, with a resonance frequency detuned by $\left(U_{\text{ee}} - U_{\text{gg}}\right)/2$ compared to the bare $|g\rangle \rightarrow |e\rangle$ transition frequency at zero magnetic field, where U_{gg} and U_{ee} denote the on-site interaction energy of $|gg\rangle$ and $|ee\rangle$ pairs, respectively.

In our experiment, we instead determine a_{ee} by performing two successive clock-excitation pulses of power $P = 1.5\,\text{mW}$ (corresponding to an intensity $I = 240\,\text{mW/cm}^2$) and duration $t_\pi = 1.26\,\text{ms}$ in a cubic optical lattice of mean depth $\bar{V} = 35.5\,(1)\, E_{\text{rec}}$, where E_{rec} denotes the lattice photon recoil energy, and magnetic field B. After coherently driving all $|gg\rangle$ pairs to the interorbital state $|\psi_{\text{eg}}^-(B)\rangle$, we scan the frequency of a second pulse addressing the $|\psi_{\text{eg}}^-(B)\rangle \rightarrow |ee\rangle$ transition, as illustrated in Fig. 4.6(a). The first pulse is resonant for a detuning $h \times \left[E_-(B) - U_{\text{gg}}\right]$ with respect to the bare $|g\rangle \rightarrow |e\rangle$ transition frequency at zero magnetic field while the second pulse is resonant for a detuning $h \times [U_{\text{ee}} - E_-(B)]$. From both detunings, the magnetic-field-independent relative interaction energy $U_{\text{ee}} - U_{\text{gg}}$ is directly obtained. To improve signal-to-noise ratio, we restrict our data evaluation to one single $5\,\text{px} \times 5\,\text{px}$ region of interest (corresponding to $2.35\,\mu\text{m} \times 2.35\,\mu\text{m}$) in the center of our absorption images. In Fig. 4.6(b-d), the number of clock-state atoms in the sample is shown as a function of the second clock-excitation pulse detuning in three different magnetic fields $B = \{1.1, 10, 25\}$ G, exhibiting two distinct features. A first peak of positive amplitude is observed, corresponding to the creation of $|e\rangle$ atoms via the single-particle $|g\uparrow\rangle \rightarrow |e\uparrow\rangle$ transition[2]. We attribute the

---

[2]At $B = 1.1\,\text{G}$, both single-particle transitions $|g\uparrow\rangle \rightarrow |e\uparrow\rangle$ and $|g\downarrow\rangle \rightarrow |e\downarrow\rangle$ are driven in the observed feature
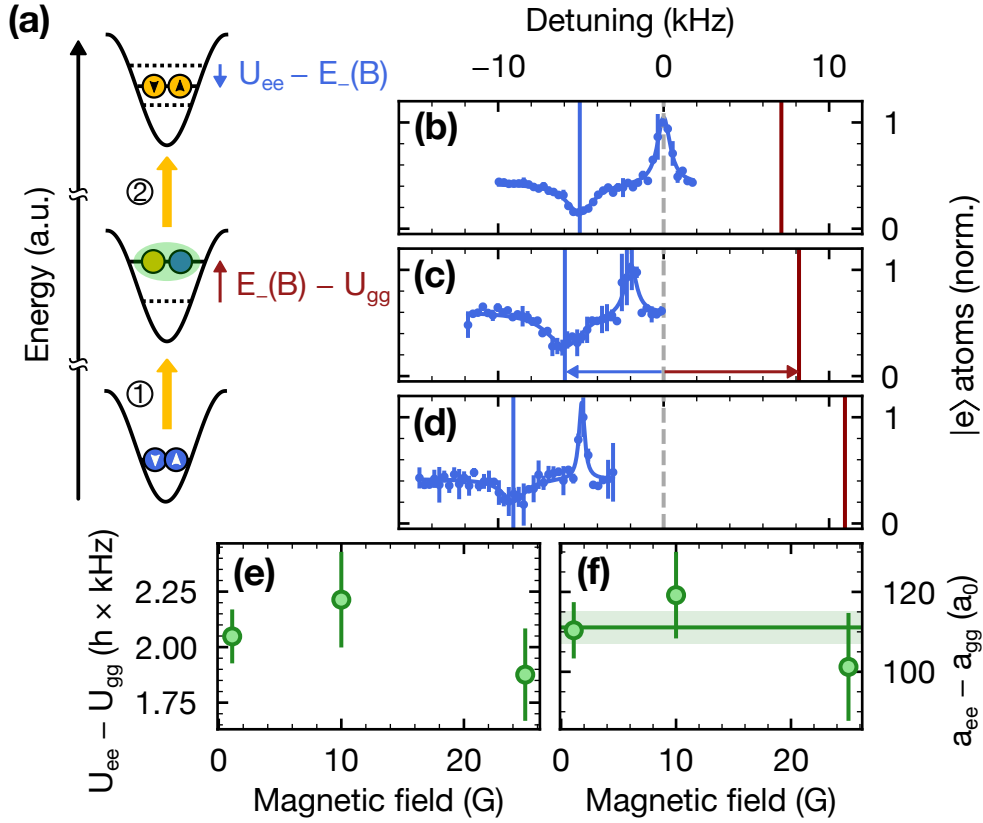
Figure 4.6 – Intraorbital ^{3}P$_0$ scattering length in ^{171}Yb. **(a)** Two-pulse sequence used to probe the s-wave scattering length a_{ee} associated with the $|ee\rangle$ state. After a first clock-laser pulse ① driving the $|gg\rangle \rightarrow |\psi_{eg}^-(B)\rangle$ transition, a subsequent pulse ② driving the $|\psi_{eg}^-(B)\rangle \rightarrow |ee\rangle$ transition is performed in a magnetic field B. The interaction shift of the first transition is $E_-(B) - U_{gg}$ while it is $U_{ee} - E_-(B)$ for the second transition, ultimately leading to $U_{ee} - U_{gg}$. We show the number of detected atoms in $|e\rangle$ as a function of the detuning of the second clock-laser pulse ② with respect to the zero-field single-particle transition frequency (dashed vertical gray lines) for **(b)** $B = 1.1\,$G, **(c)** $B = 10\,$G and **(d)** $B = 25\,$G (blue circles). Error bars are given by the standard deviation of two consecutive measurements. We fit the data with a sum of two Lorentzians, where the peak of positive amplitude represents single-particle clock transitions and the loss feature corresponds to the $|gg\rangle \rightarrow |\psi_{eg}^-(B)\rangle$ transition ②. Red vertical lines denote the position of the first transition ① while blue vertical lines represent the fitted position of ②. **(e)** Magnetic-field-independent on-site interaction energies $U_{ee} - U_{gg}$ extracted from the data. **(f)** Corresponding relative s-wave scattering lengths $a_{ee} - a_{gg}$ computed from the on-site interaction energies similarly to the interorbital scattering lengths (see Section 4.2). The green horizontal line denotes the weighted average of $a_{ee} - a_{gg}$, which is the value reported in the main text, while the green shaded area represents the uncertainty. Adapted from Ref. [188].

second feature, which corresponds to a loss of $|e\rangle$ atoms compared to the $|\psi_{\text{eg}}^-(B)\rangle$ baseline, to the formation of $|ee\rangle$ pairs. Indeed, given the extremely short lifetime of $|ee\rangle$ states in the lattice ($\sim 100\,\mu\text{s}$), these pairs leave the trap far before they are imaged (see Section 4.5). The large width of the $|ee\rangle$ loss feature, which limits our measurement precision, further hints at a short lifetime of this state.

We fit a sum of two Lorentzians to the data shown in Fig. 4.6(b-d) and determine the relative on-site interaction energy $U_{\text{ee}} - E_-(B)$ from the position of the $|ee\rangle$ peak. The interaction energy $E_-(B) - U_{\text{gg}}$ is obtained via Eq. (2.19), with the on-site interorbital interaction energies $U_{\text{eg}}^\pm$ computed from the associated scattering lengths $a_{\text{eg}}^\pm$ determined in Section 4.2 and the mean lattice depth $\bar{V}$. This leads to the values for $U_{\text{ee}} - U_{\text{gg}}$ shown in Fig. 4.6(e). We extract the associated s-wave scattering length in the same fashion as in Section 4.2, leading to the values displayed in Fig. 4.6(f). Taking the weighted average of the values obtained at each magnetic field yields

$$a_{\text{ee}} - a_{\text{gg}} = 111\,(4)\,a_0, \tag{4.8}$$

where a_0 denotes the Bohr radius. Using the known value $a_{\text{gg}} = -2.8\,(3.6)\,a_0$ [96], we finally obtain

$$a_{\text{ee}} = 108\,(8)\,a_0, \tag{4.9}$$

which is comparable to the value measured in ^{173}Yb [73].

4.4 Interorbital pair states lifetimes

A crucial parameter for the implementation of two-orbital many-body Hamiltonians in addition to the s-wave scattering lengths measured in Sections 4.2 and 4.3 is the lifetime of the interorbital states, which should ideally be much larger than all other relevant timescales governing the dynamics in the experiment. Here, we extract the two-body loss coefficient $\beta_{\text{eg}}^\pm$ associated with both interorbital states $|eg^\pm\rangle$ by measuring the lifetime of clock-state atoms in $|eg^\pm\rangle$ samples.

The experiment starts with a spin-balanced sample in a magic-wavelength cubic lattice of mean depth $\bar{V}$, containing singlons ($|g\downarrow\rangle$, $|g\uparrow\rangle$) as well as doublons ($|gg\rangle$). Doublons are subsequently excited to the interorbital states $|eg^\pm\rangle$ by means of a single coherent clock-laser pulse addressing one of the $|gg\rangle \rightarrow |\psi_{\text{eg}}^\pm(B)\rangle$ transitions in a bias magnetic field $B = 25\,\text{G}$, after which the magnetic field is ramped down to $B = 1\,\text{G}$. The pulse time $t_\pi = 397\,\mu\text{s}$ is much shorter than the lifetime of $|eg^\pm\rangle$ and bare $|e\rangle$ states and is performed with a laser power of $1.5\,\text{mW}$ corresponding to an intensity $I \approx 2.4\,\text{W/cm}^2$. Similarly to the protocol described in Section 4.2, the clock-laser pulse intensity I is slightly adjusted to ensure a constant coupling strength (and thereby pulse time t_π) throughout the measurements. After preparing the sample in the interorbital states $|eg^\pm\rangle$, the atoms are held in the lattice for a given time t_{h} and subsequently imaged. To improve the signal-to-noise ratio, a single $10\,\text{px} \times 10\,\text{px}$ ($4.7\,\mu\text{m} \times 4.7\,\mu\text{m}$) area in the center of our in-situ images is considered. The decay of a spin-polarized sample of

---

since the energy splitting between both transitions is smaller than our resolution in this experiment.
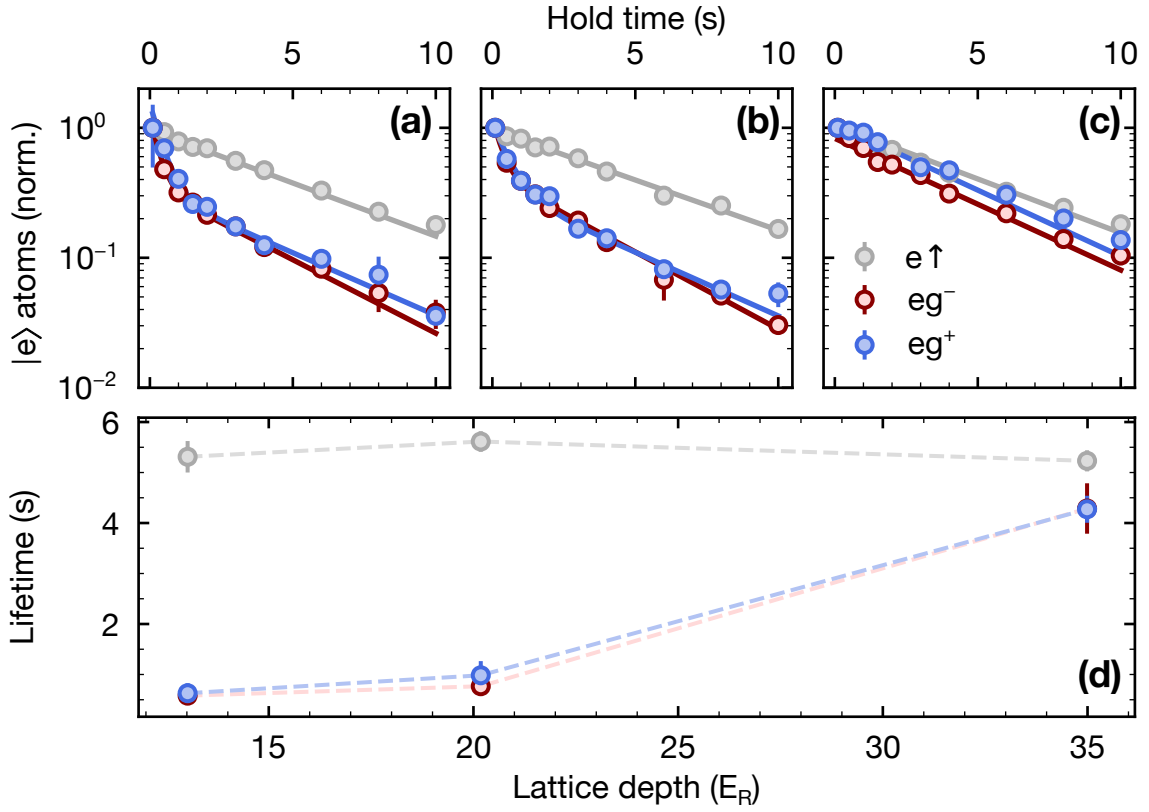
Figure 4.7 – **Lifetimes of interorbital states in ^{171}Yb.** We measure the number of atoms remaining in the clock state after a given hold time in a cubic lattice of mean depth **(a)** 13.02(9) E_{rec}, **(b)** 20.18(5) E_{rec} and **(c)** 34.99(6) E_{rec}. A spin-polarized sample prepared in $|e \uparrow\rangle$ (grey circles) is compared to spin-balanced samples prepared in the $|eg^-\rangle$ (red circles) and $|eg^+\rangle$ (blue circles) states. Solid lines correspond to fits to the data as described in the main text. The measurements are performed in a bias magnetic field of 1 G. **(d)** Corresponding $1/e$ lifetimes extracted for each lattice depth. The dashed lines serve as a guide to the eye. Adapted from Ref. [188].

$|e \uparrow\rangle$ atoms prepared with a single $|g \uparrow\rangle \rightarrow |e \uparrow\rangle$ clock-laser pulse is measured as well to serve as reference.

In Figs. 4.7(a-c), the number of clock-state atoms remaining in the trap is shown as a function of t_h for $\bar{V} = 13.02\,(9)\,E_{rec}$, $\bar{V} = 20.18\,(5)\,E_{rec}$ and $\bar{V} = 34.99\,(6)\,E_{rec}$ respectively, where E_{rec} denotes the lattice photon recoil energy. In shallower lattices with $\bar{V} = 13.02\,(9)\,E_{rec}$ and $\bar{V} = 20.18\,(5)\,E_{rec}$, the $|e\rangle$ population $P_e\,(t_h)$ in $|eg^\pm\rangle$ samples is best described by a sum of two exponentials, indicating that the decay is following two distinct time scales. In deep lattices such as $\bar{V} = 34.99\,(6)\,E_{rec}$, on the other hand, the data is well-described with a simple exponential decay of the form

$$P_e\,(t_h) = P_{e,0}e^{-t_h/\tau_{eg}^{\pm}} + \mathrm{bg}, \qquad (4.10)$$

where $P_{e,0}$ is the initial population in the clock state $|e\rangle$, $\tau_{eg}^{\pm}$ the lifetime associated with both interorbital states $|eg^\pm\rangle$ and bg accounts for background counts. Note that Eq. (4.10) accurately fits the data for spin-polarized $|e \uparrow\rangle$ samples at all lattice depths.

The resulting $1/e$ lifetimes are shown in Fig. 4.7(d). While lattice-depth independent for spin-polarized $|e\uparrow\rangle$ samples, they are significantly reduced in shallower lattices for interorbital $|eg^\pm\rangle$ samples, hinting at a tunneling-induced effect. Indeed, tunneling leads to the formation of $|ee\rangle$ pairs, which have an extremely short on-site lifetime because of the large associated two-body loss coefficient β_{ee} (see Section 4.5). In contrast, such a process is suppressed in a spin-polarized sample in $|e\uparrow\rangle$ prepared in the lowest lattice band, owing to the Pauli exclusion principle. We have verified that the decay of ground-state atoms in the same measurements is not affected by the lattice depth, further indicating that the increased loss of clock-state atoms observed in shallower lattices is not intrinsically related to two-body collisions in the $|eg^\pm\rangle$ channels.

In a deep $\bar{V} = 34.99\,(6)\,E_{\mathrm{rec}}$ lattice, tunneling is strongly suppressed, with a hopping rate $\lesssim 0.5\,\mathrm{Hz}$. Here, the $|eg^\pm\rangle$ lifetimes are not limited by tunneling and are comparable to the bare $|e\uparrow\rangle$ lifetime. This makes these states very suitable for the implementation of two-orbital Hamiltonians with ^{171}Yb atoms in optical lattices with the requirement to work in the limit of few $|e\rangle$ atoms or in a lattice which strongly suppresses the tunneling of $|e\rangle$ atoms, such as state-dependent lattices [75]. Assuming both ground- and clock-state atoms forming the $|eg^\pm\rangle$ pairs to be in the same ground lattice band, Eq. (2.51) leads to

$$\left(\tau_{\mathrm{eg}}^\pm\right)^{-1} = 2\beta_{\mathrm{eg}}^\pm \int \mathrm{d}^3\mathbf{r}\,|w_0\,(\mathbf{r})|^4, \tag{4.11}$$

where $w_0\,(\mathbf{r})$ is the ground-band Wannier function determining the on-site atomic density. Fitting Eq. (4.10) to the data gives $\tau_{\mathrm{eg}}^\pm = 4.3\,(4)\,\mathrm{s}$, which ultimately leads to the two-body loss coefficient

$$\beta_{\mathrm{eg}}^\pm \leq 2.6\,(3) \times 10^{-16}\,\mathrm{cm}^3/\mathrm{s}. \tag{4.12}$$

Here, we only specify an upper bound for $\beta_{\mathrm{eg}}^\pm$ since the $|eg^\pm\rangle$ lifetimes are comparable to the $|e\uparrow\rangle$ lifetime and residual tunneling of $|e\rangle$ atoms still takes place. We therefore overestimate $\beta_{\mathrm{eg}}^\pm$ since our value also contains the single-particle decay of $|e\rangle$ atoms and tunnel-induced $|ee\rangle$ losses. Our value is comparable to the one obtained in ^{173}Yb via a similar method [73], but is multiple orders of magnitude lower than the value $\beta_{\mathrm{eg}} = 3 \times 10^{-11}\,\mathrm{cm}^3/\mathrm{s}$ previously reported in non-degenerate ^{171}Yb gases [199].

4.5   Intraorbital pair state lifetime in the clock state

To complete the full description of intra- and interorbital interactions in ^{171}Yb, we investigate the lifetime of $|ee\rangle$ pairs as well. Collisions between two $^3P_0$ atoms are expected to be strongly inelastic in alkaline-earth(-like) elements, leading to a rapid loss through the decay of one atom to the ground state [69, 200]. It is therefore important to characterize the associated two-body loss coefficient β_{ee} since it represents a potential limitation for quantum simulation experiments involving these states.

In our experiment, the lifetime of $|ee\rangle$ states could not be measured in a cubic optical lattice, in analogy to the measurement of the $|eg^\pm\rangle$ lifetimes reported in Section 4.4. Indeed, in such
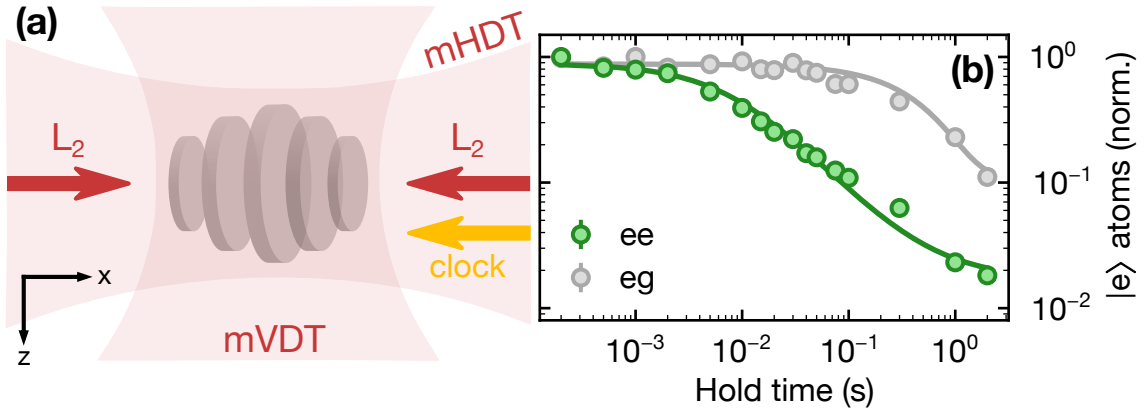
Figure 4.8 – **Lifetime of clock-state ^{171}Yb atomic pairs in two-dimensional planes.** **(a)** Sketch of the experimental geometry (not to scale). A spin-balanced sample is trapped in a magic-wavelength crossed optical dipole trap consisting of a horizontal (mHDT) and a vertical (mVDT) laser beam. A one-dimensional magic-wavelength optical lattice is additionally generated along the x axis using a single retroreflected laser beam (L2). The atoms are excited to the $^3P_0$ state by means of two consecutive clock-laser pulses addressing both $|g \uparrow\rangle \rightarrow |e \downarrow\rangle$ and $|g \downarrow\rangle \rightarrow |e \uparrow\rangle$ transitions in a bias magnetic field $B = 30$ G. The clock laser beam propagates along the lattice axis to be operating in the Lamb-Dicke regime. **(b)** Number of $|e\rangle$ atoms remaining in the sample as a function of the hold time in the traps after the clock excitation pulses, normalized by the initial atom number. We show the lifetime of $|e\rangle$ atoms in a $|e \downarrow\rangle$-$|e \uparrow\rangle$ sample (green circles) and in a $|g \downarrow\rangle$-$|e \downarrow\rangle$ sample (gray circles) for comparison. Solid lines correspond to a fit to the data using the two-body decay in Eq. (4.14) (green) or an exponential decay (gray). The depth of the optical lattice is $V_x = 31.2\,(8)\ E_{\mathrm{rec}}$, where E_{rec} is the lattice photon recoil energy. Adapted from Ref. [188].

an experimental configuration, the loss of $|ee\rangle$ pairs is occurring at timescales < 1 ms comparable with the shortest achievable clock excitation pulse duration in the experiment. The measurement geometry therefore needs to be modified to reduce the confinement of atomic pairs, as is shown in Fig. 4.8(a). A spin-balanced sample is prepared and trapped in a single-axis optical lattice of depth $V_x = 31.2\,(8)\ E_{\mathrm{rec}}$ (where E_{rec} denotes the lattice photon recoil energy) with an additional confinement provided by a magic-wavelength crossed optical dipole trap, which also holds the atoms against gravity. This prepares the atoms in quasi-two-dimensional planes, similar to the measurement reported in Ref. [73]. Two successive coherent clock-laser pulses of duration $t_\pi = 264\,\mu$s are subsequently performed along the lattice axis to drive both $|g \uparrow\rangle \rightarrow |e \downarrow\rangle$ and $|g \downarrow\rangle \rightarrow |e \uparrow\rangle$ transitions[3] in a bias magnetic field $B = 30$ G, thereby preparing the sample in a balanced statistical mixture of $|e \downarrow\rangle$ and $|e \uparrow\rangle$ atoms. The atoms are then held in the traps for a given time t_{h} and imaged. In Fig. 4.8(b), the number of remaining $|e\rangle$ atoms is shown as a function of t_{h}. The decay is significantly faster in the $|e \downarrow\rangle$-$|e \uparrow\rangle$ mixture than in a $|g \downarrow\rangle$-$|e \downarrow\rangle$ mixture prepared as comparison by only performing one single clock excitation pulse.

Since the loss of $|ee\rangle$ pairs is dominant in the decay of clock-state atoms, it can be readily

---

[3]Here we use the clock laser along the lattice axis L_2, which is circularly polarized in a vertical magnetic field and thereby drives $\sigma^\pm$ transitions. This is in contrast to all other experiments which have been performed along the lattice axis L_1 with a linearly polarized clock laser driving π transitions.

described as a two-body loss process. Assuming a perfectly spin-balanced $|e\downarrow\rangle$-$|e\uparrow\rangle$ sample, the loss of $|e\rangle$ atoms can be described by the rate equation [199]

$$\dot{n}_e(t) = -\beta_{ee}n(t)^2, \tag{4.13}$$

where $n_e(t)$ denotes the density of $|e\rangle$ atoms and β_{ee} the two-body loss coefficient between two $|e\rangle$ atoms. The solution of Eq. (4.13) is

$$n_e(t) = \frac{n_{e,0}}{1 + n_{e,0}\beta_{ee}t}, \tag{4.14}$$

defining $n_{e,0} = n_e(0)$ as the initial atomic density. While we use Eq. (4.14) to fit the data shown in Fig. 4.8(b), the two-body loss coefficient β_{ee} can only be determined if the initial atomic distribution $n_{e,0}$ is known.

To compute the initial atomic density, we model the optical lattice potential as an array of quasi-two-dimensional traps. Along the strongly-confined lattice axis x, the potential can be considered to be harmonic, with an oscillator frequency $\omega_x = 2\sqrt{s}E_{rec}/\hbar$, where E_{rec} denotes the lattice photon recoil energy and s the lattice depth in units of E_{rec} [see Eq. (2.39)]. For $s = 31.2(8)$, one obtains $\omega_x = 2\pi \times 22.6(3)$ kHz. Assuming all atoms are in the vibrational ground state of the harmonic potential, the density profile $n(z)$ along the lattice axis is given by

$$n(x) = \sqrt{\frac{m\omega_x}{\pi\hbar}}\exp\left(-\frac{m\omega_x x^2}{\hbar}\right), \tag{4.15}$$

where m is the atomic mass. Within each optical lattice plane, the distribution function in phase space $f(\mathbf{r},\mathbf{p})$ is given in the semi-classical approximation by [201]

$$f(\mathbf{r},\mathbf{p}) = \frac{2}{\mathcal{Z}^{-1}e^{\beta\left(p^2/2m+\omega_y y^2/2+\omega_z z^2/2\right)}+1}, \tag{4.16}$$

where $\mathcal{Z}$ is the fugacity of the gas and $\omega_{y,z}$ the in-plane trapping frequencies along the weakly confined axes y and z. The factor of 2 accounts for the two spin components in the sample. The density distribution $n(\mathbf{r})$ in real space is then obtained by integrating $f(\mathbf{r},\mathbf{p})$ over momentum space,

$$n(y,z) = \frac{1}{(2\pi\hbar)^2}\int d\mathbf{p}\,f(\mathbf{r},\mathbf{p}), \tag{4.17}$$

leading to a two-dimensional Thomas-Fermi density distribution

$$\begin{aligned}
n(y,z) &= -\left(\frac{m}{\pi\hbar^2\beta}\right)\mathrm{Li}_1\left\{-\mathcal{Z}\exp\left[-\frac{m\beta}{2}\left(\omega_y^2 y^2 + \omega_z^2 z^2\right)\right]\right\} \\
&= \left(\frac{m}{\pi\hbar^2\beta}\right)\ln\left\{1 + \mathcal{Z}\exp\left[-\frac{m\beta}{2}\left(\omega_y^2 y^2 + \omega_z^2 z^2\right)\right]\right\},
\end{aligned} \tag{4.18}$$

using the polylogarithm function $-\mathrm{Li}_s(-x) = \left[\int_0^\infty du\, u^{s-1}/\left(x^{-1}e^u+1\right)\right]/\Gamma(s)$ with the property $\mathrm{Li}_1(x) = -\ln(1-x)$. Here, $\Gamma(x)$ denotes the gamma function and $\beta = 1/k_B T$, with k_B the Boltzmann constant and T the temperature of the gas. We determine the trap frequencies by measuring the period of center-of-mass oscillations along y and z after a sudden trap

	s-wave scattering lengths (a_0)				Two-body loss coefficients (cm^3/s)	
	a_{gg}	a_{eg}^+	a_{eg}^-	a_{ee}	$\beta_{\text{eg}}^\pm$	β_{ee}
Kitagawa et al. [96]	$-2.8(3.6)$	–	–	–	–	–
Ono et al. [194]	–	225(13)	355(6)	–	–	–
Abeln et al. [198]	–	203(5)	308(6)	–	–	–
This thesis	–	240(4)	389(4)	108(8)	$\leq 2.6(3) \times 10^{-16}$	$4.8(2.1) \times 10^{-12}$

Table 4.1 – Summary of the $^1S_0$–$^3P_0$ intra- and interorbital s-wave scattering lengths and two-body loss coefficients in ^{171}Yb obtained in this chapter or reported by other research groups. The s-wave scattering lengths are given in units of a_0, which represents the Bohr radius.

displacement, and obtain $\omega_y = 2\pi \times 53.7\,(8.1)$ Hz as well as $\omega_z = 2\pi \times 262.6\,(2.8)$ Hz. The temperature is obtained by directly fitting the in-situ integrated column density distribution $n_c(y) = \int \mathrm{d}z\, n(y,z)$, leading to $T = 117\,(41)$ nK.

The total density distribution is then obtained by combining Eqs. (4.15) and (4.18) and is given by $n(x,y,z) = n(x)\,n(y,z)$. We find a weighted average initial density

$$\bar{n} = \frac{\int \mathrm{d}\mathbf{r}\, n(x,y,z)^2}{\int \mathrm{d}\mathbf{r}\, n(x,y,z)} = 2.0\,(7) \times 10^{13}\,\text{cm}^{-3}, \tag{4.19}$$

which we use as value for $n_{\text{e},0}$ in Eq. (4.14). A fit to the data shown in Fig. 4.8(b) then leads to a two-body loss coefficient

$$\beta_{\text{ee}} = 4.8\,(2.1) \times 10^{-12}\,\text{cm}^3/\text{s}, \tag{4.20}$$

which is comparable to a similar measurement performed with ^{171}Yb in the high-temperature regime [199] and to previous results obtained with ^{173}Yb [73] and ^{88}Sr [200] atoms. It is much larger than the two-body loss coefficient $\beta_{\text{eg}}^\pm$ associated with the interorbital states. In any quantum simulation experiment involving clock-state atoms, it is therefore essential to isolate $|e\rangle$ atoms to prevent lossy *e-e* collisions. This can be achieved by working in the limit of very few $|e\rangle$ atoms or by using deep optical lattice potentials for $|e\rangle$ atoms, for instance via a state-dependent lattice in which $|g\rangle$ atoms are mobile and $|e\rangle$ atoms are strongly localized [75].

4.6   Discussion

Together with the previously known ground-state intraorbital scattering length a_{gg} measured via two-color photoassociation spectroscopy on the intercombination line [96], the various measurements reported in this chapter fully characterize the $^1S_0$–$^3P_0$ intra- and interorbital interactions in ^{171}Yb. In Table 4.1, we give an overview of the currently known elastic and inelastic interaction parameters, including the values obtained in this chapter as well as results from other research groups.

In particular, two other groups have recently reported values for the interorbital scattering lengths $a_{\text{eg}}^\pm$ [194, 198] which differ by up to $\approx 20\%$ from our measurements, far outside the

	s-wave scattering lengths (a_0)		Spin-exchange interactions
	a_{eg}^+	a_{eg}^-	
^{87}Sr [87]	169(8)	68(22)	Ferromagnetic
^{173}Yb [73]	$\approx 4 \times 10^3$	220(3)	Ferromagnetic
^{171}Yb (This thesis)	240(4)	389(4)	Antiferromagnetic

Table 4.2 – Comparison of the $^1S_0$–$^3P_0$ interorbital scattering lengths in different alkaline-earth(-like) elements, using this thesis as reference for ^{171}Yb. The s-wave scattering lengths are given in units of a_0, which represents the Bohr radius.

range defined by the reported uncertainties. The reasons behind these discrepancies are currently unknown to us. In Ref. [194], the measurement is performed in a similar geometry but only the pair-state energy branch $E_-(B)$ is probed, which could lead to a less accurate determination of the on-site interaction energies $U_{\mathrm{eg}}^{\pm}$. In Ref. [198], the measurement is performed in a triangular lattice and this geometry is taken into account when computing $a_{\mathrm{eg}}^{\pm}$ from $U_{\mathrm{eg}}^{\pm}$. Both references use Eq. (2.49) with ground-band Wannier functions as wavefunctions to model on-site interactions, which is slightly different from the model we have used. This however only leads to small discrepancies, since using Eq. (2.49) with ground-band Wannier functions to extract the scattering lengths leads to $a_{\mathrm{eg}}^+ = 245(4)\,a_0$ and $a_{\mathrm{eg}}^- = 389(4)\,a_0$ using our data, which still differ from the other values reported in Table 4.1.

A central consequence resulting from the interorbital scattering lengths reported in this thesis is that $a_{\mathrm{eg}}^+ - a_{\mathrm{eg}}^- < 0$, in qualitative agreement with Refs [194, 198]. This implies antiferromagnetic spin-exchange interactions $V_{\mathrm{ex}} < 0$ in ^{171}Yb, in strong contrast with the situation in ^{87}Sr and in ^{173}Yb, where ferromagnetic spin-exchange interactions have been reported [73, 87], see Tab. 4.2. This opens the way for the study of the antiferromagnetic Kondo and Kondo lattice models [69, 78–84] with ultracold ^{171}Yb atoms in state-dependent optical lattices [75].

Finally, the very small two-body loss coefficient $\beta_{\mathrm{eg}}^{\pm}$ associated with the $|eg^{\pm}\rangle$ states leads to their long lifetime in optical lattices, which are comparable to the lifetime of single $|e\rangle$ atoms. This makes these states suitable for uses in quantum simulation experiments. On the other hand, the very short lifetime of $|ee\rangle$ states arising from strongly inelastic collisions is an inevitable limitation that needs to be taken into consideration when designing experiments. This fact is expected in alkaline-earth(-like) atoms [69] and has also been observed in ^{88}Sr [200] and ^{173}Yb [73], which feature similar clock-state two-body loss coefficients. To circumvent this issue and prevent the formation of $|ee\rangle$ pairs during experiments, a lattice in which $|e\rangle$ atoms are strongly localized must be used, such as a state-dependent lattice for $|g\rangle$ and $|e\rangle$ atoms [75]. Alternatively, experiments could be performed in the limit of very few $|e\rangle$ atoms, which is relevant for the investigation of impurity physics [118]. Overall, the unique combination of antiferromagnetic spin-exchange interactions, long-lived interorbital pair states and almost vanishing ground-state scattering length a_{gg} makes ^{171}Yb an ideal candidate for the quantum simulation in optical lattices and in the limit of zero magnetic fields of two-orbital

models based on spin-exchange interactions.

Observation of an orbital Feshbach resonance in ^{171}Yb

Despite the absence of magnetic Feshbach resonances in alkaline-earth(-like) atoms, these elements potentially feature so-called orbital Feshbach resonances (OFRs) [103] between atoms in the electronic ground and clock states. While so far only observed in ^{173}Yb [105, 106], the elastic interorbital scattering parameters determined in Chapter 4 hint at an OFR occuring at an experimentally accessible magnetic field in ^{171}Yb as well, as discussed in Section 2.2.4.

In this chapter, we report on the observation and characterization of the OFR in ^{171}Yb. We measure the binding energy of the molecular dimer state associated with the resonance as well as the repulsive interaction energy of the open-channel pair state via clock-line spectroscopy at large magnetic fields. The obtained data is well-described by an effective open-channel model, allowing to extract the resonance position, resonance width and background scattering length. In a second measurement, we precisely determine the scattering length zero-crossing position by measuring the dimer state binding energy in a narrow magnetic field range.

5.1   Experimental configuration and sequence

The experimental configuration and sequence used for the measurements reported in this chapter are practically identical to the detailed description given in Section 4.1. The main difference is that significantly larger magnetic fields up to $1600\,\text{G}$ are probed here. Throughout this chapter, we mainly probe three different clock-line transitions which are the single-particle transition

$$|g\uparrow\rangle \rightarrow |e\uparrow\rangle \tag{5.1}$$

as well as the two-particle transitions

$$|gg\rangle \rightarrow |o\rangle \tag{5.2}$$

and

$$|gg\rangle \rightarrow |b_\text{c}\rangle. \tag{5.3}$$

These three transitions are illustrated in Fig. 5.1(a). Here, $|o\rangle$ denotes the energetically accessible open interaction channel, which is given by the state $|eg\uparrow\downarrow\rangle$ defined in Eq. (2.23) in the

limit of large interparticle distances and at large magnetic fields where the differential Zeeman shift is large compared to the spin-exchange interaction energy. The state $|b_\mathrm{c}\rangle$ represents the least-bound state supported by the closed-channel interatomic potential $|c\rangle$[1]. Note that we again use the notations $|g\rangle \equiv |^1\mathrm{S}_0\rangle$, $|e\rangle \equiv |^3\mathrm{P}_0\rangle$, $|\downarrow\rangle \equiv |m_F = -1/2\rangle$ and $|\uparrow\rangle \equiv |m_F = +1/2\rangle$ to describe the internal state of single atoms.

5.2 Large-field lattice interaction spectroscopy

Two ultracold atoms in an isotropic harmonic trap with an interaction described using a regularized pseudopotential follow an exactly solvable Schrödinger equation [150], as described in Section 2.4.2. In particular, the eigenenergies can be computed exactly and depend only on the s-wave scattering length a, the harmonic trapping frequency ω_ho and the atomic mass m, leading to the energy branches shown in Fig. 2.4. As clearly visible in Fig. 2.4(b), these eigenenergies exhibit a strong dependence on $1/a$ around $1/a = 0$. Measuring these energy branches with interorbital pairs of ^{171}Yb atoms in various external magnetic fields therefore represents an advantageous method to probe the magnetic field dependence of the interorbital scattering length a, in particular the resonant behavior expected in the vicinity of the OFR.

In order to observe and characterize the OFR in ^{171}Yb, we probe the interaction energy of the pair states $|b_\mathrm{c}\rangle$ and $|o\rangle$, which correspond to both energetically lowest-lying states displayed in Fig. 2.4(b). All measurements are performed in a magic-wavelength isotropic cubic optical lattice of mean depth $\bar{V} = 30.36\,(5)\,E_\mathrm{rec}$, where $E_\mathrm{rec} = (2\pi\hbar)^2/2m\lambda_\mathrm{m}$ denotes the lattice photon recoil energy, with m the atomic mass and $\lambda_\mathrm{m} = 759.4\,\mathrm{nm}$ the lattice wavelength. In such a deep lattice, the on-site trapping potential can be assumed to be approximately harmonic, with an harmonic trapping frequency $\omega_\mathrm{ho} = 2\pi \times 22.31\,(2)\,\mathrm{kHz}$ [see Eq. (2.39)].

We perform clock-line spectroscopy measurements at large magnetic fields $B = \{5, \dots, 1600\}\,\mathrm{G}$ on both pair transitions $|gg\rangle \to |b_\mathrm{c}\rangle$ and $|gg\rangle \to |o\rangle$ in spin-balanced samples. As a reference, we also measure the single-particle transition $|g\uparrow\rangle \to |e\uparrow\rangle$ in spin-polarized samples. The $|g\uparrow\rangle \to |e\uparrow\rangle$ and $|gg\rangle \to |o\rangle$ transitions are driven with coherent π-pulses of power $P = 20\,\mu\mathrm{W}$ (corresponding to an intensity $I \approx 32\,\mathrm{mW/cm}^2$) and duration $t_\pi = 3.44\,\mathrm{ms}$. The $|gg\rangle \to |b_\mathrm{c}\rangle$ transitions are on the other hand driven with long incoherent pulses of power $P = 150\,\mathrm{nW}$ ($I \approx 240\,\mu\mathrm{W/cm}^2$) and duration $t = 250\,\mathrm{ms}$ at magnetic fields $B \in [1350, 1600]\,\mathrm{G}$ and of power $P = 1.5\,\mu\mathrm{W}$ ($I \approx 2.4\,\mathrm{mW/cm}^2$) and duration $t = 250\,\mathrm{ms}$ at magnetic fields $B \in [1000, 1200]\,\mathrm{G}$. At magnetic fields below $1000\,\mathrm{G}$, the transition into the bound state is driven with short pulses of power $P = 10\,\mathrm{mW}$ ($I \approx 1.6\,\mathrm{W/cm}^2$) and duration $t = 490\,\mu\mathrm{s}$. To improve the signal-to-noise ratio, we restrict the evaluation of our in-situ absorption images to a small region of interest (ROI) of $6\,\mathrm{px} \times 6\,\mathrm{px}$ (corresponding to $2.82\,\mu\mathrm{m} \times 2.82\,\mu\mathrm{m}$) in the center of the atomic cloud.

At each magnetic field, every resonance is individually fitted with a Lorentzian profile, as shown for $B = 1000\,\mathrm{G}$ in Fig. 5.1(b-c). Here, the single-particle transition frequency is used as

---

[1]In the limit of large interparticle distances and at large magnetic fields, the closed interaction channel $|c\rangle$ is given by the state $|eg\downarrow\uparrow\rangle$ defined in Eq. (2.23).
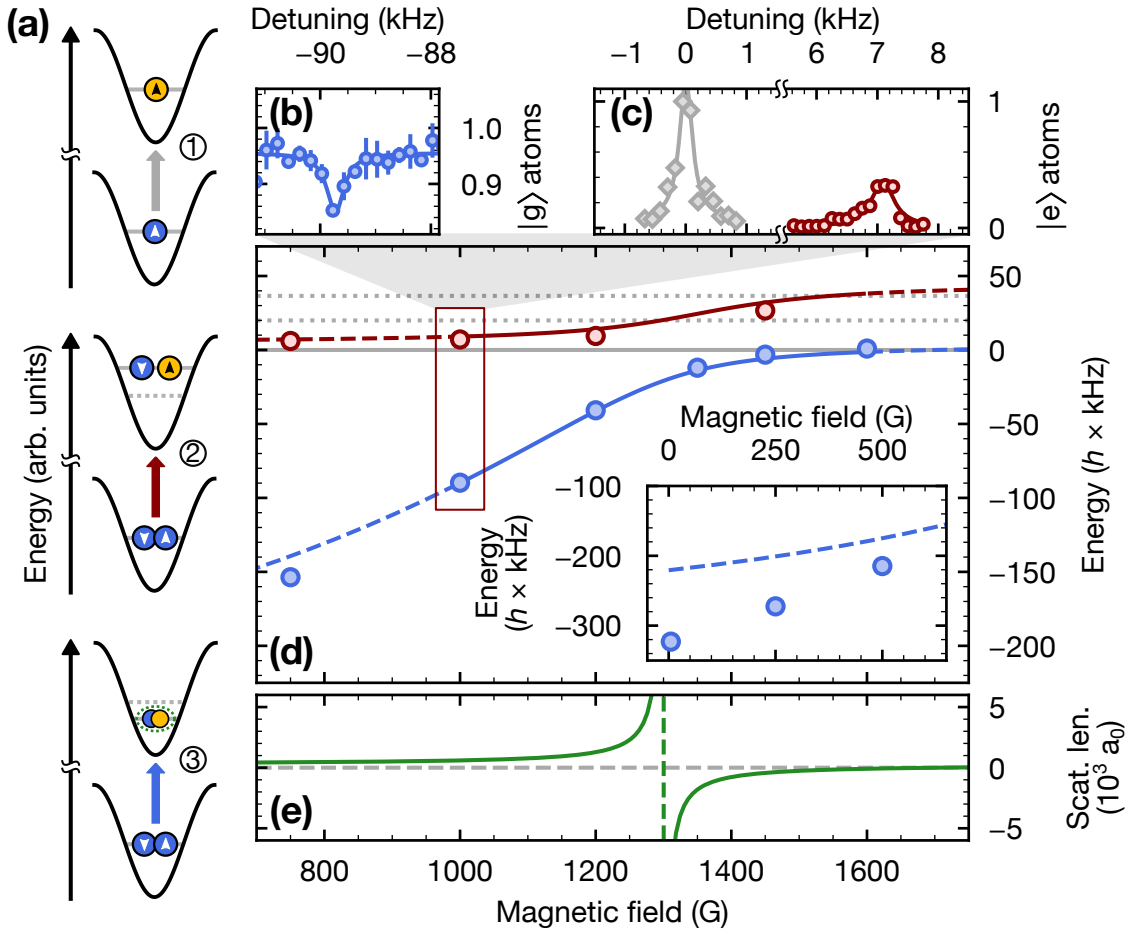
Figure 5.1 – Orbital Feshbach resonance in ^{171}Yb. (a) Relevant single- and two-particle transitions on the clock line in a deep cubic optical lattice. We drive the single-particle transition ①: $|g\uparrow\rangle \rightarrow |e\uparrow\rangle$ as well as the two-particle transitions into the repulsively interacting open-channel pair state ②: $|gg\rangle \rightarrow |o\rangle$ and into the closed-channel molecular bound state ③: $|gg\rangle \rightarrow |b_c\rangle$. Solid black lines represent the on-site lattice potential while solid gray lines denote the energy of each state compared to the single-particle state energy (dotted gray lines). Here, the very small on-site pair interaction energy in the ground state U_{gg} is omitted. **(b-c)** Raw clock-line spectroscopy measurements at a magnetic field $B = 1000$ G. To maximize the signal, the transition frequency into the bound state ③ is determined using the loss of ground-state atoms (blue circles) while the transition frequency into the open-channel pair state ② (red circles) as well as the single-particle transition frequency ① (gray diamonds) are obtained from the detection of clock-state atoms. The detuning is defined with respect to the single-particle transition frequency. Solid lines denote Lorentzian fits to the data. **(d)** Energy of the open-channel pair state $|o\rangle$ (red circles) and closed-channel dimer state $|b_c\rangle$ (blue circles) relative to the single-particle state energy (solid gray line) at large variable magnetic fields. The data points are obtained from fits to clock-line spectroscopy data such as shown in (b-c). The inset shows the bound-state energy at lower magnetic fields. We fit the data to the theoretical model described in the main text between 1000 G and 1600 G (solid lines), where the universal Feshbach relations hold well for the bound state. Outside this magnetic field range, we show the fitted model as dashed lines. Both horizontal dotted gray lines denote the first and second lattice band excitations. **(e)** Interorbital scattering length as a function of the magnetic field (solid lines) extracted from the fitted model in (d). The dashed vertical line at $B = 1300$ G marks the OFR position. Adapted from Ref. [188].

reference for both two-particle transitions. The resulting pair interaction energies are shown in Fig. 5.1(d) and exhibit a behavior typically corresponding to a divergence of the interorbital scattering length around 1300 G where the binding energy of $|b_{\rm c}\rangle$ vanishes as it approaches the threshold. We note a strong loss of contrast on the transition into $|o\rangle$ between 1250 G and 1400 G, in the vicinity of the OFR. We currently do not have a clear explanation for this observation, which could possibly be related to avoided crossings with other two-body states occuring at these magnetic fields.

To theoretically describe the data, we use the energy solutions $E(1/a)$ for two ultracold atoms in a harmonic potential [150] defined by [see Eq. (2.54)]

$$\sqrt{2}\frac{\Gamma(-E/2\hbar\omega_{\rm ho}+3/4)}{\Gamma(-E/2\hbar\omega_{\rm ho}+1/4)}=\frac{a_{\rm ho}}{a}, \tag{5.4}$$

where $a_{\rm ho}=\sqrt{\hbar/m\omega_{\rm ho}}$ denotes the harmonic oscillator length. We account for the on-site lattice potential anharmonicity by means of first-order perturbation theory corrections to the eigenergies computed using Eq. (5.4), as described in Section 2.4.2. Here, the potential is expanded up to 8$^{\rm th}$ order around each lattice site. Around the OFR, where the universal Feshbach relations hold well for the bound state, the magnetic field dependence of the interorbital scattering length is well-described by an effective open-channel model given by the simple expression [33, 202]

$$a(B)=a_{\rm bg}\left(1-\frac{\Delta}{B-B_0}\right), \tag{5.5}$$

where B_0 is the resonance position, Δ the resonance width and $a_{\rm bg}$ the background scattering length. Fitting Eqs. (5.4) and (5.5) to the data shown in Fig. 5.1(d) between 1000 G and 1600 G leads to the resonance parameters $B_0 = 1300(44)$ G, $\Delta = 402(169)$ G and $a_{\rm bg} = 255(24)\,a_0$ in ^{171}Yb, where a_0 denotes the Bohr radius. Using these parameters, Eq. (5.5) leads to the interorbital scattering lengths $a(B)$ shown in Fig. 5.1(e) as function of the magnetic field. As can be seen in Fig. 5.1(e), the OFR occurs at an accessible magnetic field and enables the tuning of $a(B)$ over a broad range. The fairly large resonance width Δ is convenient for the experimental investigation of the strongly interacting regime, which does not require overly stringent conditions for the stability of the magnetic field.

A useful additional quantity to describe the resonance is the strength parameter $s_{\rm res}$ defined in Eq. (2.29). In the context of the OFR, the differential magnetic moment $\delta\mu = 399.0(1)\,h\,{\rm Hz/G}$ is given by the differential Zeeman shift and has been determined in Section 3.4 for ^{171}Yb. Using Eq. (2.29) together with Eqs. (2.12) and (2.14) leads to

$$s_{\rm res}=0.16(8) \tag{5.6}$$

for the OFR in ^{171}Yb, a value comparable to the one obtained in ^{173}Yb [154]. Here we have used the C_6 van der Waals coefficient $C_6 = 2561$ computed in Ref. [68] for $^1{\rm S}_0 + ^3{\rm P}_0$ ytterbium dimers using configuration interaction together with coupled-cluster all-order calculations. The uncertainty on $s_{\rm res}$ is dominated by the rather large uncertainty on the resonance width Δ.

5.3 Two-channel on-site interaction model

The open-channel theoretical model used in Section 5.2 accurately describes the magnetic field dependence of the scattering length in the universal regime in the vicinity of the OFR. In Fig. 5.1(d), it is apparent that the open-channel model fails at magnetic fields outside this range, where contributions from the closed channel become significant. Here, we therefore make an attempt at describing our experimental data with the two-channel interaction model that has been successfully used for the OFR in ^{173}Yb [105, 154].

The problem of two ^{171}Yb atoms in a three-dimensional harmonic trap can be separated into center-of-mass and relative coordinates, see Section 2.4.2. The total Hamiltonian in the relative basis considering both interaction channels $|o\rangle$ and $|c\rangle$ is the sum of the non-interacting Hamiltonian

$$\hat{H}_0 = \sum_n \epsilon_n |o,n\rangle \langle o,n| + \sum_n (\epsilon_n + \delta) |c,n\rangle \langle c,n| \tag{5.7}$$

and interacting Hamiltonian

$$\hat{V} = \sum_{n,n'} \varphi_n(0)\,\varphi_{n'}(0) \Big[U_{\text{eg}}^+ |eg^+,n\rangle \langle eg^+,n| + U_{\text{eg}}^- |eg^-,n\rangle \langle eg^-,n| \Big], \tag{5.8}$$

where n denotes the harmonic oscillator state with angular momentum $l = 0$, $\varphi_n(0)$ the harmonic oscillator wavefunction at position $r = 0$, $\delta(B) = 399.0(1) \times B$ Hz the magnetic field-dependent differential Zeeman shift and $|eg^\pm\rangle$ the interorbital pair states defined in Eq. (2.17) with on-site interaction energies $U_{\text{eg}}^\pm$.

Using the general wavefunction $|\psi\rangle$ in the $\{|eg^-\rangle, |eg^+\rangle\}$ basis given by

$$|\psi\rangle = \sum_n c_n^+ |eg^+,n\rangle + c_n^- |eg^-,n\rangle \tag{5.9}$$

allows for the derivation of the eigenenergies E in the T-matrix formalism, which are defined by the equation [154]

$$\left[\frac{2a_{\text{ho}}}{a_{\text{eg}}^-} - \mathscr{F}_0\left(\frac{-E}{\hbar\omega_{\text{ho}}}\right) - \mathscr{F}_0\left(\frac{-E+\delta}{\hbar\omega_{\text{ho}}}\right) \right] \left[\frac{2a_{\text{ho}}}{a_{\text{eg}}^+} - \mathscr{F}_0\left(\frac{-E}{\hbar\omega_{\text{ho}}}\right) - \mathscr{F}_0\left(\frac{-E+\delta}{\hbar\omega_{\text{ho}}}\right) \right]$$
$$- \left[\mathscr{F}_0\left(\frac{-E}{\hbar\omega_{\text{ho}}}\right) - \mathscr{F}_0\left(\frac{-E+\delta}{\hbar\omega_{\text{ho}}}\right) \right]^2 = 0. \tag{5.10}$$

Here we have introduced the harmonic oscillator frequency ω_{ho} defined in Eq. (2.39), the harmonic oscillator length $a_{\text{ho}} = \sqrt{\hbar/m\omega_{\text{ho}}}$ and $\mathscr{F}_0(x) = \sqrt{2}\Gamma(x/2 + 3/4)/\Gamma(x/2 + 1/4)$, where $\Gamma(x)$ denotes the Gamma function. In a deep optical lattice, ω_{ho} can be computed using Eq. (2.39), leading to $\omega_{\text{ho}} = 2\pi \times 22.3$ kHz in our case. While Eq. (5.10) is valid for zero-range interactions, finite-range corrections can be readily added by making the replacement [105]

$$\frac{1}{a_{\text{eg}}^\pm} \to \frac{1}{a_{\text{eg}}^\pm} - \frac{1}{2} \frac{m r_{\text{eff}}^\pm}{\hbar^2} \left(E - \frac{\delta}{2} + \frac{3}{2}\hbar\omega_{\text{ho}} \right), \tag{5.11}$$

where $r_{\text{eff}}^+ = 130.0(9)\,a_0$ and $r_{\text{eff}}^- = 157.6(6)\,a_0$ are the effective ranges that can be analytically computed using Eq. (2.15).
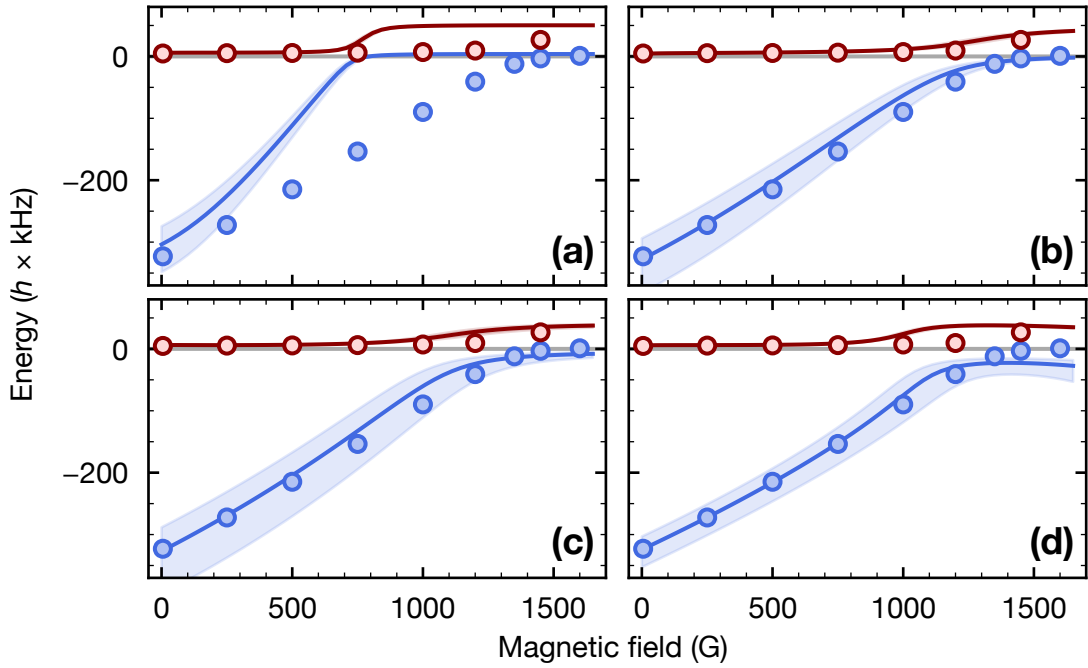
Figure 5.2 – **Two-channel model for the OFR in ^{171}Yb.** We show the energy of the open-channel pair state $|o\rangle$ (red circles) and closed-channel dimer state $|b_c\rangle$ (blue circles) relative to the single-particle transition energy (horizontal gray line). The data is identical to Fig. 5.1(d). Solid colored lines correspond to the energy branches obtained by using the two-channel model described in the main text with **(a)** scattering lengths $a_{eg}^{\pm}$ determined in Section 4.2 and analytically calculated effective ranges $r_{eff}^{\pm}$, **(b)** fitted $a_{eg}^{\pm}$ and analytically calculated $r_{eff}^{\pm}$ from the fitted $a_{eg}^{\pm}$, **(c)** $a_{eg}^{\pm}$ determined in Section 4.2 and fitted $r_{eff}^{\pm}$, **(d)** $a_{eg}^{\pm}$ determined in Section 4.2, analytically calculated $r_{eff}^{\pm}$ and higher-order energy contribution $\propto k^4$ fitted to the data. The colored areas represent a variation of $\pm 10\%$ of the singlet effective range r_{eff}^{-}, showing an important sensitivity of the resulting energy branches to small changes of r_{eff}^{-}.

The obtained energy branches using the scattering lengths $a_{eg}^{\pm}$ determined in Section 4.2 are shown in Fig. 5.2(a). While the zero-field bound-state energy is predicted well by the model, it fails to describe our data at larger fields and implies an OFR occuring at a magnetic field much lower than the experimentally observed one.

To gain further insight, we use the interorbital scattering lengths as free parameters and fit the two-channel model to our data. The result is shown in Fig. 5.2(b) and describes the data well. However, while the fitted scattering length $a_{eg}^{-} \approx 378\,a_0$ is in fair agreement with the measured value, the other fitted scattering length $a_{eg}^{+} \approx 138\,a_0$ is clearly inconsistent with the value measured in Section 4.2. Another option is to use the effective ranges $r_{eff}^{\pm}$ as free parameters while using the experimentally determined interorbital scattering lengths. The resulting fit is shown in Fig. 5.2(c). Here, while the fitted $r_{eff}^{-} \approx 166\,a_0$ corresponds well to the analytically calculated value, we obtain a very large $r_{eff}^{+} \approx 654\,a_0$ in disagreement with our prediction.

In an additional attempt at capturing the large-field energy behavior, we add a higher-order

term $\mathcal{O}\left(k^4\right)$ in the low-energy expansion in Eq. (5.11), yielding

$$\frac{1}{a_{\mathrm{eg}}^\pm} \rightarrow \frac{1}{a_{\mathrm{eg}}^\pm} - \frac{1}{2}\frac{mr_{\mathrm{eff}}^\pm}{\hbar^2}\left(E - \frac{\delta}{2} + \frac{3}{2}\hbar\omega_{\mathrm{ho}}\right) + \beta\left(E - \frac{\delta}{2} + \frac{3}{2}\hbar\omega_{\mathrm{ho}}\right)^2, \qquad (5.12)$$

where we use β as a free fit parameter while using the measured and analytically calculated $a_{\mathrm{eg}}^\pm$ and $r_{\mathrm{eff}}^\pm$. The resulting energy branches are displayed in Fig. 5.2(d) and show an overcompensation arising from the additional $\mathcal{O}\left(k^4\right)$ term at larger fields leading to a non-monotonous behavior.

A significant difference between the situation in ^{173}Yb and in ^{171}Yb is the resonance position, which occurs around $B_0 \approx 40\,\mathrm{G}$ in ^{173}Yb [103, 105, 106] and $B_0 \approx 1300\,\mathrm{G}$ in ^{171}Yb. In the vicinity of the resonance in ^{171}Yb, the differential Zeeman shift $\delta\left(B\right) \approx 0.25\,\mathrm{MHz}$ is much larger than in ^{173}Yb and makes the scattering amplitude particularly sensitive to finite-range effects [203]. This can be seen in Fig. 5.2(a), where the model captures the low-field behavior well but fails at larger fields. The above measurement spans a very large range of energy scales, and it is therefore challenging to engineer a low-energy model covering this entire range.

5.4 Interorbital scattering length zero crossing

Since the strength parameter of the OFR in ^{171}Yb is very small, i.e. $s_{\mathrm{res}} \ll 1$, the resonance is narrow and the model used in Section 5.2 is only expected to hold well within a small range $\left|(B - B_0)/\Delta\right| \ll 1$ [33]. In particular, this means that the scattering length zero-crossing position $B_{\mathrm{zc}} = B_0 + \Delta = 1702\,(175)\,\mathrm{G}$ is not accurately determined by the measurement reported in Section 5.2, mainly because of the inaccurate calculation of Δ. However, the zero-crossing position is a crucial parameter to implement interorbital mixtures of ^{171}Yb in the non-interacting regime, such as in the measurements reported in Ref. [119].

We precisely probe the zero-crossing position B_{zc} of the OFR in ^{171}Yb by repeating the measurement presented in Section 5.2 in a narrow range of magnetic fields $B = \{1400, \ldots, 1600\}\,\mathrm{G}$ around B_{zc} in a $30.7\,(8)\,E_{\mathrm{rec}}$ deep lattice. Here, we only perform clock-line spectroscopy on the free-to-bound transition $|gg\rangle \rightarrow |b_{\mathrm{c}}\rangle$ and on the single-particle transition $|g\uparrow\rangle \rightarrow |e\uparrow\rangle$. The resulting interaction energies relative to the single-particle transition are shown in Fig. 5.3(a). The data is fitted using the same on-site interaction model as in Section 5.2, using the expression

$$a\left(B\right) = a_{\mathrm{bg}}\left(\frac{B - B_{\mathrm{zc}}}{B - B_0}\right) \qquad (5.13)$$

for the magnetic field dependence of the scattering length around B_{zc}. This equation is equivalent to Eq. (5.5) using $B_{\mathrm{zc}} = B_0 + \Delta$ in order to introduce an explicit dependence on B_{zc}. As can be seen in Fig. 5.3(a), the data is very well described by our theoretical model within this narrow magnetic field range, leading to the parameters $B_{\mathrm{zc}} = 1538.3\,(2)\,\mathrm{G}$, $B_0 = 1316.9\,(2)\,\mathrm{G}$ and $a_{\mathrm{bg}} = 285\,(2)\,a_0$. Using the resonance position determined in Section 5.2 and the zero-crossing position obtained above leads to a resonance width $\Delta = 238\,(44)\,\mathrm{G}$ and strength
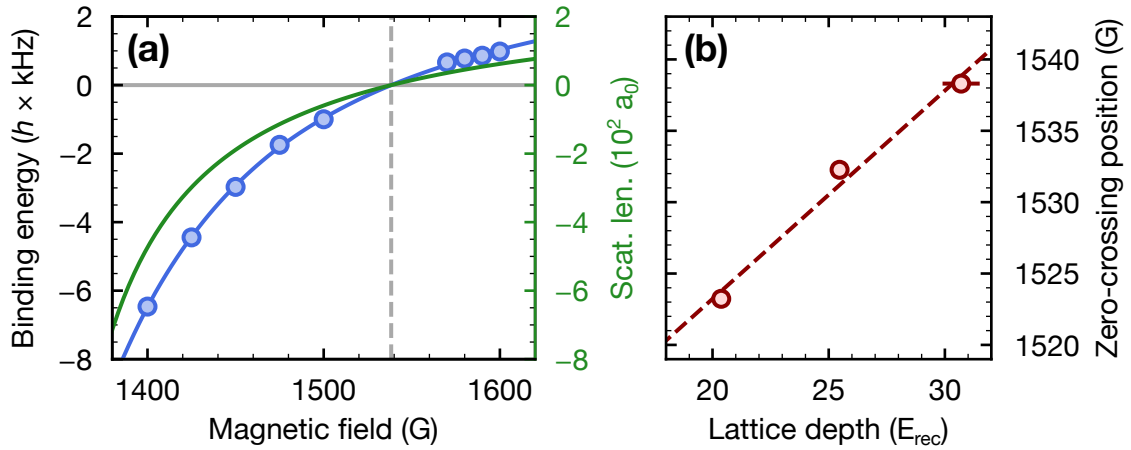
Figure 5.3 – **Orbital Feshbach resonance zero crossing in ^{171}Yb. (a)** Energy of the closed-channel dimer state $|b_c\rangle$ (blue circles) relative to the single-particle state energy (solid horizontal gray line) around the OFR zero crossing, measured via clock-line spectroscopy. The solid blue line corresponds to a fit to the data using Eqs. (5.4) and (5.13) while the dashed vertical gray line denotes the position of the OFR zero crossing from the fit. The interorbital scattering length given by Eq. (5.13) is shown as well (solid green line). **(b)** Position of the OFR zero crossing as a function of the mean lattice depth. The data point at $30.7\,(8)\,E_{\rm rec}$ corresponds to the measurement shown in (a). The dashed red line corresponds to a linear fit to the data.

parameter $s_{\rm res} = 0.09\,(3)$, which corresponds to a very narrow resonance. Here, we have used the background scattering length $a_{\rm bg}$ determined in Section 5.2.

All resonance parameters reported above have been obtained at a given mean lattice depth $\bar{V} = 30.7\,(8)\,E_{\rm rec}$. However, we have observed that the zero-crossing position significantly depends on the lattice depth, see Fig. 5.3(b), with a slope of $1.5\,(2)\,{\rm G}/E_{\rm rec}$. This in an important point that needs to be taken into account when using the OFR to prepare non-interacting interorbital mixtures. We consider this shift to be a finite- range effect. Indeed, it can be seen from Eq. (5.11) that the effective range $r_{\rm eff}^{\pm}$ introduces an explicit energy dependence of the interorbital scattering lengths $a_{\rm eg}^{\pm}$. Here, a change in the lattice zero-point motion energy calls for a modified differential Zeeman shift $\delta\,(B)$ to yield the same scattering cross-section, effectively shifting the OFR zero-crossing position.

5.5   Discussion

This chapter reports on the first experimental observation and characterization of an OFR in ^{171}Yb occuring between interorbital atomic pairs at $B_0 = 1300\,(44)$ G, which had so far only been observed in ^{173}Yb [105, 106]. In Table 5.1, the resonance parameters obtained from clock-line spectroscopy measurements both for a wide magnetic field range around the resonance position and for a narrow magnetic field range around the zero-crossing position are summarized.

Near the resonance, the measured closed-channel bound state and open-channel pair-state

	B_0 (G)	Δ (G)	B_{zc} (G)	a_{bg} (a_0)
Measurement I (Section 5.2)	1300(44)	402(169)	–	255(24)
Measurement II (Section 5.4)	1316.9(2)	–	1538.3(2)	285(2)
Combined	1300(44)	238(44)	1538.3(2)	255(24)

Table 5.1 – Orbital Feshbach resonance parameters. We give the resonance position B_0, width Δ and zero crossing B_{zc} as well as the background scattering length a_{bg} obtained from clock-line spectroscopy measurements in a large magnetic field range around the resonance (Measurement I) and in a narrow range around the zero crossing, in a 30.7(8) E_{rec} deep cubic lattice (Measurement II). We also show the values obtained when combining B_0 and a_{bg} extracted from Measurement I with B_{zc} extracted from Measurement II, yielding $\Delta = B_{zc} - B_0$.

energies shown in Fig. 5.1(d) are accurately described by the energy solutions of Eq. (2.54) combined with an effective open-channel model given by Eq. (2.24) for the interorbital scattering length, yielding credible values for the resonance position and for the background scattering length. However, this theoretical description fails when moving away from the open channel dominated universal regime and leads here to an inaccurate resonance width or zero crossing. A second measurement around the OFR zero-crossing position is therefore required to obtain a complete set of meaningful resonance parameters, which is shown in Table 5.1. From this, we find a very small value for the resonance strength parameter $s_{res} = 0.09(3)$, indicating a very narrow resonance similarly to the situation in ^{173}Yb [154].

The two-channel model which has been highly successful in describing the on-site interactions energies in the vicinity of the OFR in ^{173}Yb [105] fails to cover the full energy range of the interaction spectroscopy measurement in Fig. 5.1(d) and to reliably predict the OFR position. Leaving the interorbital scattering lengths or the effective ranges as free fit parameters leads to values inconsistent with the measurements described in Section 4.2. We attribute this to the large energy range of our results which is difficult to entirely cover with a low-energy model and to the large linear Zeeman shift on resonance, which makes the scattering amplitude highly sensitive to finite range effects. The accurate theoretical description of our results therefore remains a challenging and interesting open problem.

Overall, the OFR in ^{171}Yb allows to fully control interorbital interactions with an external magnetic field and therefore makes this isotope a promising platform for the quantum simulation of multiorbital many-body systems in the strongly-interacting regime.

A strongly-bound interorbital dimer on the clock transition

In Chapter 5, the orbital Feshbach resonance (OFR) in ^{171}Yb is observed and characterized by measuring the binding energy of the least-bound state supported by the closed-channel interorbital molecular interaction potential as a function of the external magnetic field. In strong contrast to the bound state associated with the OFR in ^{173}Yb, the one in ^{171}Yb has a large binding energy at zero magnetic field far exceeding all other relevant energy scales in typical experiments with ultracold atoms. This state could therefore be of interest in the context of optical molecular clocks.

In this chapter, after determining the zero-field binding energy of the above mentioned interorbital dimer state, we show that the free-to-bound transition into the dimer can be made first-order insensitive to the trap depth by an appropriate choice of the lattice wavelength, a first step towards high-resolution spectroscopy of the molecular bound state energy on the ^{171}Yb clock line. In addition, we demonstrate the direct formation of this dimer state by photoassociation in two-dimensional pancake-shaped traps as well.

6.1 Strongly-bound dimer state in a cubic lattice

The transition $|gg\rangle \rightarrow |b_{\mathrm{c}}\rangle$ from a free ground-state atomic pair into the interorbital closed-channel bound state associated with the OFR is measured in Section 5.2 in a cubic lattice within a large magnetic field range between $5\,\mathrm{G}$ and $1600\,\mathrm{G}$. In Fig. 6.1(a), we show a raw spectroscopy measurement adressing the free-to-bound transition at $5\,\mathrm{G}$. The data can be fitted with a Lorentzian profile to extract the free-to-bound transition frequency $\delta_0 = -324.0\,(1)$ kHz with respect to the zero-field single-particle transition $|g\uparrow\rangle \rightarrow |e\uparrow\rangle$. In order to determine the bare molecular binding energy ϵ_{b} from δ_0, the contribution of the single-particle zero-point
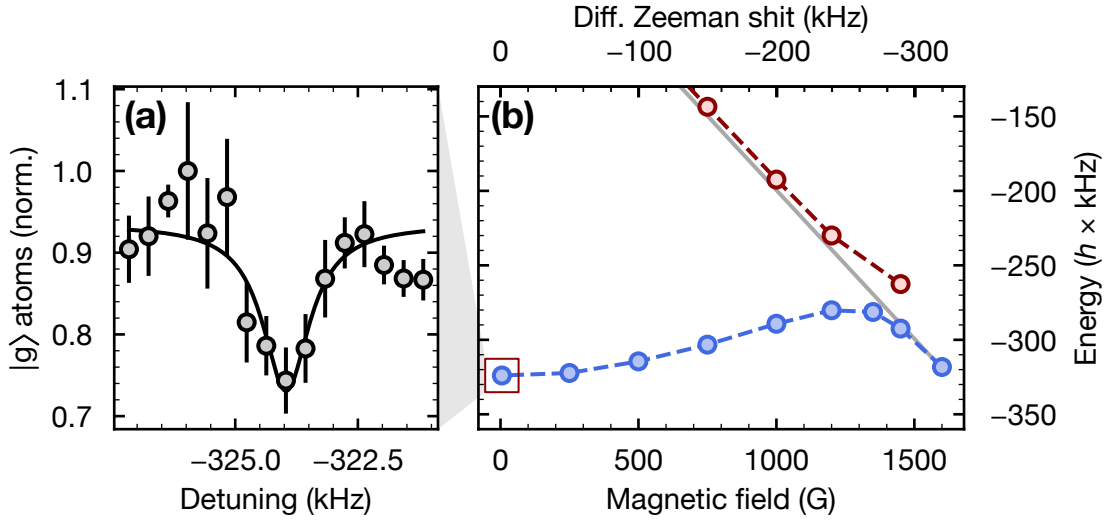
Figure 6.1 – **Interorbital dimer state with large binding energy in a cubic lattice.** **(a)** Raw clock-line spectroscopy measurement into the interorbital bound state [corresponding to the transition ③ sketched in Fig. 5.1(a)] shown at a 5 G magnetic field. Error bars denote the standard error of two consecutive measurements and the black solid line refers to a Lorentzian fit to the data, yielding a transition frequency detuned by $-324.0\,(1)$ kHz with respect to the single-particle clock transition at zero magnetic field. This corresponds to a binding energy $\epsilon_\mathrm{b} = h \times 292.1\,(2)$ kHz after removing the zero-point energy of one particle in the trapping potential (see main text). **(b)** Energy of the closed-channel dimer state (blue circles) relative to the zero-field single-particle transition energy, showing a weak magnetic field dependence for differential Zeeman shifts $\lesssim 50$ kHz. Red circles represent the energy of the transition into the open-channel pair state $|eg\uparrow\downarrow\rangle$. The data is identical to the one shown in Fig. 5.1(d). The solid gray line denotes the energy of the single-particle transition $|g\uparrow\rangle \to |e\downarrow\rangle$ sketched in Fig. 5.1(a). Dashed lines serve as a guide to the eye.

energy $\epsilon_{0,i}$ along a lattice axis $i = \{x, y, z\}$ needs to be taken into account[1], leading to

$$\epsilon_\mathrm{b} = -\left(h\delta_0 + \sum_i \epsilon_{0,i} \right).$$

(6.1)

Using the zero-point energies $\epsilon_{0,i}$ obtained after full diagonalization of the lattice Hamiltonian (see Section 2.3.1), we obtain a molecular binding energy $\epsilon_\mathrm{b} = h \times 292.1\,(2)$ kHz which is very large compared to the situation in ^{173}Yb [105]. We also note that this value is significantly larger than the estimate $\epsilon_\mathrm{b,th} = h \times 213\,(5)$ kHz obtained using Eq. (2.27) together with the elastic interorbital s-wave scattering lengths $a_\mathrm{eg}^\pm$ determined in Section 4.2, indicating that the bound state is far outside the universal regime at low magnetic fields. On the other hand, the dimer binding energy is predicted with good accuracy by the two-channel model described in Section 5.3 using the interorbital scattering lengths obtained in Section 4.2, see Fig. 5.2(a).

In Fig. 5.1(d), the different energies are represented with respect to the single-particle transition energy at each magnetic field in order to make the energy branches defined by

---

[1]The energy of the initial state $|gg\rangle$ with two free ground-state particles contains two zero-point contributions, while the energy of the final dimer state $|b_c\rangle$ contains a single zero-point contribution since both atoms form a strongly-bound molecule. This leads to an additional shift of the free-to-bound transition frequency which needs to be taken into account for the calculation of the binding energy.

Eq. (5.4) apparent. However, it is also instructive to plot these energy branches with respect to the zero-field single-particle transition energy. The result is shown in Fig. 6.1(b) and clearly indicates that the dimer binding energy is almost magnetic-field independent for magnetic fields $B \lesssim 200\,\text{G}$ corresponding to a differential Zeeman shift $\delta \lesssim 50\,\text{kHz}$ of the single-particle transition. This is expected for a strongly-bound molecular state where the binding energy dominates the Zeeman energy. At larger magnetic fields, the Zeeman energy becomes comparable to the binding energy and induces a magnetic field dependence for the dimer binding energy.

6.2 Strongly-bound dimer state in pancake-shaped traps

In Section 6.1, the on-site clock-line photoassociation of interorbital dimers is discussed in the case of a deep cubic lattice. Here, we demonstrate that such dimers can be similarly produced in a bulk gas confined in strongly elliptical traps.

The experimental geometry is similar to the one used in Section 4.5 to characterize inelastic scattering in $|ee\rangle$ states [also see Fig. 4.8(a)]. A single-axis magic-wavelength optical lattice (L_1) of depth $25.2\,(1)\,E_{\text{rec}}$ generates pancake-shaped two-dimensional traps along the axis y, where E_{rec} denotes the recoil energy of a lattice photon. At the same time, a magic-wavelength crossed-beam optical dipole trap (mHDT and mVDT) provides additional confinement against gravity. The trapping frequencies $\omega_x = 53.7\,(8.1)\,\text{Hz}$ and $\omega_z = 262.6\,(2.8)\,\text{Hz}$ along the weakly-confined axes x and z are determined by measuring the period of center-of-mass oscillations along these axes after a sudden trap displacement. To improve the signal-to-noise ratio, we restrict the evaluation of our in-situ absorption images to a small region of interest (ROI) of $6\,\text{px} \times 6\,\text{px}$ (corresponding to $2.82\,\mu\text{m} \times 2.82\,\mu\text{m}$) in the center of the atomic cloud. The free-to-bound transition is driven with long incoherent clock-laser pulses of power $P = 1\,\text{mW}$ (intensity $I \approx 160\,\text{mW/cm}^2$) and duration $t = 75\,\text{ms}$ propagating along L_1.

We perform clock-line spectroscopy measurements at three different magnetic fields $B = \{1.1, 5, 50\}\,\text{G}$, a range where the dimer binding energy $\epsilon_\text{b} = h \times 292.1\,(2)\,\text{kHz}$ is almost constant [see Fig. 6.1(b)]. The obtained energy spectra are shown in Fig. 6.2 and exhibit a clear resonant feature corresponding to the production of dimers on the free-to-bound transition. In contrast to the situation in a cubic lattice, however, the obtained lineshapes are asymmetric because of the continuous momentum distribution within the sample and cannot be fitted with a simple Lorentzian function. A straightforward way to describe the data shown in Fig. 6.2 is to consider the convolution of a Lorentzian (accounting for the zero-momentum spectral response) and a Fermi-Dirac distribution (accounting for the momentum distribution within the sample). Taking into account the fact that the positive atomic kinetic energies in the sample lead to negative shifts of the transition frequency, the response of the system as a function of the detuning δ can therefore be written as

$$f(\delta, \delta_0, \Gamma, \textit{z}, \beta, A, C) = \left\{ A \int_{-\infty}^{0} \frac{\mathrm{d}x}{\left[x^2/\Gamma^2 + 1\right]\left[\textit{z}^{-1}e^{\beta h(-\delta + \delta_0 - x)} + 1\right]} \right\} + C, \qquad (6.2)$$
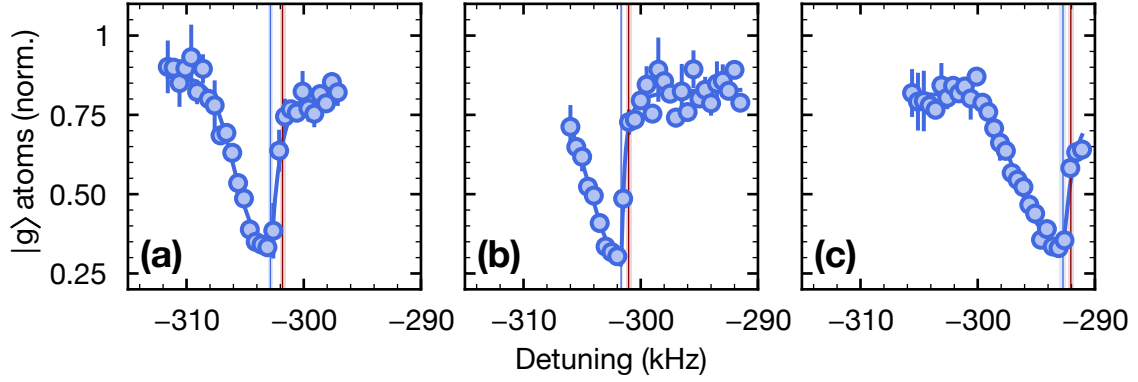
Figure 6.2 – **Interorbital dimer state binding energy in two-dimensional free-space.** Raw clock-line spectroscopy measurements into the interorbital dimer state at magnetic field **(a)** 1.1 G, **(b)** 5 G and **(c)** 50 G. The measurements are performed in a $25.2\,(1)\,E_{\mathrm{rec}}$ deep single-axis optical lattice and the frequency detuning is defined with respect to the single-particle transition $|g\uparrow\rangle \rightarrow |e\uparrow\rangle$. Error bars denote the standard error of two consecutive measurements. The solid blue lines represent fits of Eq. (6.2) to the data, with the blue vertical lines indicating the fitted transition frequencies. The red vertical lines represent the predicted transition frequency using Eq. (6.3). Adapted from Ref. [188].

where the zero-momentum resonance detuning δ_0 with respect to the $|g\uparrow\rangle \rightarrow |e\uparrow\rangle$ transition, resonance linewidth Γ, fugacity $\mathcal{Z}$, inverse temperature β, amplitude A and offset C are considered free fit parameters. Our data is very well described by Eq. (6.2) as can be seen in Fig. 6.2, allowing to reliably extract the resonance position (blue vertical lines).

The detuning on resonance $\delta_0\,(B)$ can also be directly predicted from the bare dimer binding energy, the trap parameters and the differential Zeeman shift. We can write

$$\delta_0\,(B) = -\frac{1}{h}\left[\epsilon_{\mathrm{b}} + \epsilon_{0,y} + \hbar\,(\omega_x + \omega_z) + \delta\,(B)\right], \tag{6.3}$$

where $\epsilon_{0,y} = 9.62\,(2)\,\mathrm{kHz}$ denotes the zero-point energy along the strongly-confined lattice axis y computed numerically from the diagonalization of the lattice Hamiltonian (see Section 2.3.1) and $\delta\,(B) = -hB/2{\times}399.0\,(1)\,\mathrm{Hz}$ the differential Zeeman shift of the single-particle transition $|g\uparrow\rangle \rightarrow |e\uparrow\rangle$. The obtained resonance positions are represented as red vertical lines in Fig. 6.2 and are in excellent agreement with the resonance position extracted from the fit of Eq. (6.2) to our data. The small relative discrepancy up to 0.3% between both positions can be explained by systematical errors in the determination of the lattice depth such as drifts occuring between the lattice calibration and the measurement, or drifts of the clock excitation laser.

6.3   Trap-depth-insensitive free-to-bound transition

The measurements discussed in Sections 6.1 and 6.2 have all been performed in trapping potentials operating at the magic wavelength $\lambda_{\mathrm{m}} = 759.4\,\mathrm{nm}$ of the single-particle transition. This choice of wavelength is appropriate for the two-particle transition $|gg\rangle \rightarrow |eg\uparrow\downarrow\rangle$
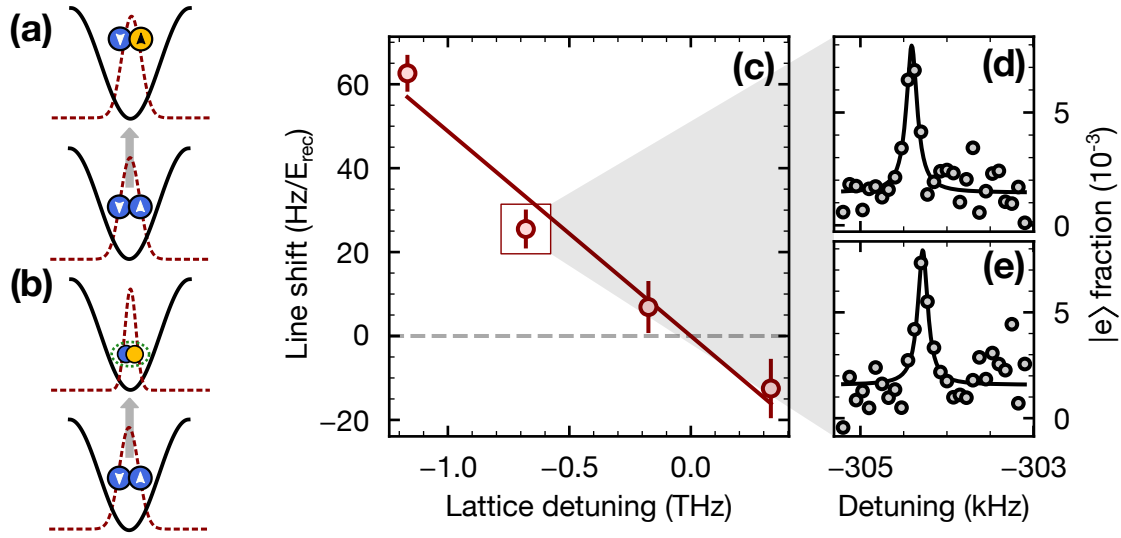
Figure 6.3 – **Trapping potential with depth-independent free-to-bound transition into the dimer.** We show a sketch of the **(a)** free-to-free $|gg\rangle \rightarrow |eg\uparrow\downarrow\rangle$ and **(b)** free-to-bound $|gg\rangle \rightarrow |b_c\rangle$ transitions in an optical lattice. Solid black lines denote the trapping potential and dashed red lines represent the pair-state spatial wavefunction in the lowest lattice energy band. While the wavefunction is not significantly modified in the free-to-free transition (a), it samples a smaller region of the trapping potential after the transition into the dimer (b). **(c)** First-order linear shift of the free-to-bound transition in a cubic lattice, relative to the lattice depth. Each shift is determined from two consecutive clock-line spectroscopy measurements in a $25E_{\text{rec}}$ and $30E_{\text{rec}}$ deep lattice such as shown in (d) and (e). The shift is shown for various detunings of the lattice laser frequency with respect to the value $f_0 = 386.0\,(1)$ THz that cancels the linear shift. This frequency corresponds to a wavelength $\lambda_0 = 776.6\,(2)$ nm. The solid red line denotes a linear fit to the data with a slope of $-49\,(5)\ \text{Hz}/\left(E_{\text{rec}}\text{THz}\right)$. **(d)-(e)** Clock-line spectroscopy of the free-to-bound transition (b) in a $25E_{\text{rec}}$ and $30E_{\text{rec}}$ lattice of wavelength 778 nm (385.3 THz), respectively. Solid lines denote Lorentzian fits to the data. Adapted from Ref. [188].

into the repulsively-interacting pair state since the pair-state wavefunction is not significantly modified during the transition, see Fig. 6.3(a). The situation is different when driving the free-to-bound transition $|gg\rangle \rightarrow |b_c\rangle$ since the dimer wavefunction features a smaller fraction of the trapping potential than the initial free pair wavefunction owing to its large binding energy, see Fig. 6.3(b). As a consequence, the frequency of the transition into the dimer depends on the local lattice depth. Since the laser beams generating the trapping potentials have a nearly Gaussian intensity profile, this leads to an inhomogeneous free-to-bound transition frequency, effectively broadening the transition line and leading to dephasing of both states. This is analogous to addressing the single-particle clock transition at a non-magic wavelength, see Section 3.3.3, and is an important obstacle to using the free-to-bound transition for precision spectroscopy.

A straightforward strategy to make the transition frequency independent of the trap depth is to introduce a suitable differential ac Stark shift $\Delta U_{\text{ac}}(\mathbf{r})$ [see Eq. (3.28)] between the ground and the excited state which exactly cancels the light shift caused by the modified pair state wavefunction. Since the dimer wavefunction samples a smaller region around the

trap minimum than the free pair wavefunction, the induced shift of the free-to-bound line $\partial \delta_0/\partial V < 0$ is negative, where δ_0 denotes the detuning of the line with respect to the single-particle transition $|g \uparrow\rangle \rightarrow |e \uparrow\rangle$ and V the potential depth. A positive ac Stark shift should therefore be introduced by increasing the wavelength of the trapping potential with respect to the magic wavelength λ_{m}, see Fig. 2.2.

We implement this approach by comparing the free-to-bound transition frequency in a deep cubic optical lattice of depth $30.03\,(6)\,E_{\mathrm{rec}}$ and $25.03\,(5)\,E_{\mathrm{rec}}$ for different lattice laser wavelengths from 776 nm to 779 nm, see Fig. 6.3(d-e). The free-to-bound transition is driven at a magnetic field $B = 1.1\,\mathrm{G}$ with long incoherent clock-laser pulses of power $P = 2.5\,\mu\mathrm{W}$ (intensity $I \approx 4\,\mathrm{mW/cm^2}$) and duration $t = 250\,\mathrm{ms}$. For each lattice wavelength, we compare the free-to-bound transition frequency at both lattice depths to determine the line shift and find a linear dependence, as can be seen in Fig. 6.3(c). In particular, we notice that the line shift is canceled for a lattice wavelength $\lambda_0 = 776.6\,(2)$ nm corresponding to a frequency of $386.0\,(1)$ THz. At this wavelength, the transition into the dimer state is independent of the trap depth and we observe narrow lines $\sim 100\,\mathrm{Hz}$, which are limited by the linewidth of the clock laser. It is important to note that the obtained wavelength is not universal, in contrast to the single-particle transition magic wavelength. Here, the wavelength canceling the free-to-bound line shift is only valid to first order for a specific choice of magnetic field and lattice depth.

6.4   Discussion

In this chapter, the stronlgy-bound molecular state associated with the OFR in ^{171}Yb is investigated. This state is nearly independent of the magnetic field B for $B \lesssim 200\,\mathrm{G}$ (or small differential Zeeman shifts $\lesssim 50\,\mathrm{kHz}$). Using the data obtained in Chapter 5, we find a zero-field binding energy $\epsilon_{\mathrm{b}} = h \times 292.1\,(2)$ kHz which is significantly larger than the value expected from a simple calculation using the interorbital scattering lengths $a_{\mathrm{eg}}^{\pm}$ determined in Section 4.2, which indicates that the bound state is outside the purely universal regime [33]. The measured value, while still close to the regime of a universal halo dimer [204], is larger by at least one order of magnitude than other relevant energy scales in cold atomic ensembles. Indeed, values for the lattice band gap or zero-point energy, the Fermi energy, the temperatures or the level spacing between neighboring optical lattice traps do typically not exceed $\sim 10\,\mathrm{kHz}$ levels. The dimer wavefunction is therefore only weakly perturbed by the external confinement, which opens the way for the direct photoassociation of interorbital dimers on a unique and particularly well-defined optical transition on the ultranarrow clock line. This is in strong contrast with the weakly-bound dimer state associated with the OFR in ^{173}Yb [105], which is intrinsically in the resonant regime and strongly depends on the trap parameters.

The above properties could make the dimer state in ^{171}Yb interesting in the context of optical molecular clocks, which have to this day only been realized on the intercombination line in ^{88}Sr [133]. These clocks have been proposed as sensitive probes for precision tests of fundamental physics such as variations of constants or gravitation on microscopic scales [134,

135, 205]. In particular, the free-to-bound transition into the dimer state in ^{171}Yb could enable an optical molecular clock operating directly on the ultranarrow $^{1}S_0 \rightarrow {}^{3}P_0$ line, similar to the implementation proposed in Ref. [135] using ^{174}Yb atoms.

The proof-of-principle demonstration reported in Section 6.3 of a lattice wavelength making the transition into the dimer insensitive to the trap depth is an important first step towards precision spectroscopy on the $|gg\rangle \rightarrow |b_c\rangle$ line. In our experiment, this has enabled the observation of narrow molecular lineshapes limited by the finite driving laser linewidth $\sim 100\,\text{Hz}$. This wavelength is non-trivial since it differs from the magic wavelength canceling the differential ac Stark shift between the ground and excited electronic states. Indeed, the line shift induced by the modification of the pair state wavefunction during the free-to-bound transition calls for a suitable ac Stark shift to cancel this effect to first order. However, the obtained wavelength is not universal but only valid for a given set of magnetic field and lattice depth. The measurement presented in Section 6.3 would therefore need to be performed for every specific experimental configuration.

All measurements reported in this chapter have used long incoherent clock-excitation pulses to produce the interorbital dimers. A promising next experimental milestone would be the observation of coherent oscillations between the free pair and the interorbital dimer states $|gg\rangle \leftrightarrow |b_c\rangle$, similarly to the Rabi oscillations observed in Ref. [206] on the transition into the bound state associated with the OFR in ^{173}Yb.

Conclusions and outlook

The work presented in this thesis provides a substantial characterization of interactions between ultracold ^{171}Yb atoms in the electronic ground and clock state at small and large magnetic fields.

In a first set of measurements, we have extensively probed elastic as well as inelastic scattering in interorbital mixtures of ^{171}Yb at low magnetic fields. By means of clock-line spectroscopy in state-independent optical lattices, we have determined the s-wave scattering lengths $a_{eg}^+ = 240\,(4)\,a_0$, $a_{eg}^- = 389\,(4)\,a_0$ and $a_{ee} = 108\,(8)\,a_0$ associated with the interorbital pair states $|eg^\pm\rangle$ and intraorbital pair state $|ee\rangle$, where $|g\rangle$ ($|e\rangle$) denotes the electronic ground (clock) state and $+$ ($-$) the symmetric (antisymmetric) superposition of orbital states. In particular, since $a_{eg}^+ < a_{eg}^-$, these results imply antiferromagnetic spin-exchange interactions $V_{ex} < 0$ in ^{171}Yb, in agreement with similar measurements [194, 198]. By measuring the lifetime of atomic pairs in optical lattices, we have also investigated inelastic scattering in these states. While the lifetime of $|eg^\pm\rangle$ states is very long and even comparable to the lifetime of the $|e\rangle$ state in a deep lattice where the motion of clock-state atoms is frozen, $|ee\rangle$ pairs are very quickly lost from the trap owing to strongly inelasting scattering.

In the interaction-dominated regime where the differential Zeeman shift is small, two-orbital physics are dominated by spin-exchange interactions. Here, ^{171}Yb possesses a promising combination of properties for the quantum simulation of two-orbital many-body physics, namely the reasonably large antiferromagnetic spin-exchange interaction arising from $a_{eg}^+ - a_{eg}^- = -149\,(6)\,a_0$, the very long lifetime of interorbital states and the remarkably small s-wave scattering length $a_{gg} = -2.8\,(3.6)\,a_0$ in the ground state [96]. Together with the experimental accessibility of state-dependent lattices with itinerant ground-state atoms and localized clock-state atoms [75], this makes this isotope an ideal platform for the study of the Kondo effect using clock-state atoms as localized magnetic impurities in a Fermi sea of mobile ground-state atoms.

A first step towards the observation of Kondo-type physics has recently been achieved through the observation of spin-exchange dynamics in a one-dimensional state-dependent lattice for ^{171}Yb [76], in analogy to a similar measurement performed in ^{173}Yb [75]. The main experimental challenge which currently needs to be overcome is to reach temperatures smaller than the Kondo temperature T_K, under which spin-singlet correlations become significant. This could be achieved by using a quantum gas microscope together with an optical

tweezer or by enhancing the spin-exchange interaction energy via confinement-induced reso-
nances [75, 120, 121]. A significant achievement would then be for instance the observation
of the Kondo spin-screening cloud, which has recently been observed in a quantum dot [207].
Alternatively, using one Kondo impurity on every lattice site realizes the Kondo lattice model,
which features very rich physics in the antiferromagnetic regime, including heavy-Fermion
behavior [64, 98] or unconventional superconductivity [208].

In a second set of clock-line spectroscopy measurements performed at larger magnetic
fields, we have observed an orbital Feshbach resonance (OFR) occurring at a magnetic field
$B = 1300\,(44)$ G by tracking the energy branches corresponding to the repulsively-interacting
open-channel pair state and to the least-bound state supported by the closed-channel inter-
atomic potential. The data is well-described by the exact energy solutions for two atoms in a
harmonic trap interacting via contact interactions [150], using a simple open-channel model
for the scattering length. On the other hand, the two-channel model which has been success-
fully applied to describe the OFR in ^{173}Yb [105] is not well-suited, even when considering
analytically calculated effective ranges from the van der Waals potential [145]. We attribute
this to the very large differential Zeeman shift around the resonance, making the scattering
amplitude particularly sensitive to finite-range effects. The OFR occurs at a large but experi-
mentally accessible magnetic field, where spin-exchange interactions are strongly suppressed,
in contrast to the OFR in ^{173}Yb [105, 106].

The OFR in ^{171}Yb enables full control over interorbital interactions through an external
magnetic field and makes this isotope an excellent platform to study multiorbital quantum
gases in the strongly-interacting regime. A striking aspect of the OFR is its small strength pa-
rameter $s_{\mathrm{res}} \ll 1$, defining the OFR as narrow [33] while featuring a large resonance width of
several hundreds of Gauss. This is due to the small magnetic moment difference $\delta\mu$ between
the open and the closed channel compared to usual magnetic Feshbach resonances and enables
the study of the famous BEC-BCS crossover [209–212] or strongly-interacting Fermi superflu-
ids in the vicinity of a narrow resonance [107]. While narrow Feshbach resonances also occur
in alkali atoms and have enabled the production of strongly interacting Fermi gases [213],
such systems require precise control of the magnetic field to remain in the strongly interacting
regime and are usually plagued with short lifetimes near resonance. Intriguingly, the equation
of state of the unitary Fermi gas [214–216] could be probed around the OFR as well.

The OFR furthermore offers promising prospects for the quantum simulation of impurity
physics with orbital degree of freedom. A prominent example is the Fermi polaron prob-
lem, which has been extensively studied in numerous experiments with alkali atoms [217–
224]. With alkaline-earth(-like) atoms, such polarons can be realized by preparing few mo-
bile clock-state atoms in a Fermi sea of ground-state atoms and have recently been observed
in ^{173}Yb [118]. Here, the OFR is used to tune the interactions between the impurity and the
surrounding Fermi sea. Fermi polarons have attracted considerable interest in the context of
multiorbital quantum gases [225–227] owing to the complexity of interactions across the OFR
which are in particular expected to lead to Pauli-blocking of two-body scattering processes in
the presence of an additional Fermi sea [117, 228].

We also note that the OFR observed in this work has been exploited in a recent experiment

probing transport in the mass-imbalanced Fermi-Hubbard model using ^{171}Yb atoms in a state-dependent lattice [119]. In this experiment, non-interacting interorbital superposition states are first prepared on the OFR zero-crossing before enabling attractive or repulsive interorbital interactions via a magnetic field ramp.

Finally, we have been able to directly photoassociate the molecular dimer state associated with the OFR on the clock transition. The dimer features a binding energy far exceeding all other relevant energy scales in typical cold-atoms experiment such as the band structure, the Fermi energy, the level spacing of the optical lattice traps or temperatures. This is in strong contrast with the situation in ^{173}Yb [105], where the dimer binding energy is comparable to other typical energy scales. In particular, this implies that the molecular wavefunction is largely independent of the trap parameters, enabling a photoassociation process on a unique and well-defined optical transition. This makes this dimer potentially interesting in the context of molecular optical clocks [132, 133] which have been proposed for precision tests of fundamental physics [134, 135, 205]. For instance, the transition into the dimer state in ^{171}Yb would enable the molecular clock spectroscopy on the Hz level proposed in Ref. [135] for ^{174}Yb atoms, with the additional advantage of featuring direct clock-line photoassociation. Since the wavefunction of the dimer state features a smaller region of the trapping potential than the free atomic pair, the free-to-bound transition energy depends on the local trap depth. We have shown that this effect can be compensated to first order by inducing an appropriate differential light shift between ground- and clock-state atoms. This effectively creates a state-independent potential for the free-to-bound transition at a given lattice depth, an important first step towards molecular clock spectroscopy with ^{171}Yb atoms. An interesting next step would be the observation of coherent Rabi oscillations between the free pair and dimer states, in analogy to the work reported in Ref. [206] for weakly-bound molecules in ^{173}Yb.

To conclude, the findings reported in this work establish ^{171}Yb as an excellent platform for the quantum simulation of two-orbital Fermi-Hubbard models in optical lattices. The antiferromagnetic interorbital spin-exchange interactions together with the long lifetime of the interorbital states offer highly promising prospects for the implementation of Kondo-type models while the OFR paves the way for the study of exciting multiorbital systems in the strongly-interacting regime with these atoms. Furthermore, the strongly-bound molecular dimer state associated with the OFR is an intriguing feature that could be of use in the context of molecular optical clocks.

Bibliography

[1] M. H. Anderson, J. R. Ensher, M. R. Matthews, C. E. Wieman, and E. A. Cornell. *Observation of Bose-Einstein Condensation in a Dilute Atomic Vapor*. Science **269**, 198–201 (1995). See page: 1

[2] K. B. Davis, M. O. Mewes, M. R. Andrews, N. J. van Druten, D. S. Durfee, D. M. Kurn, and W. Ketterle. *Bose-Einstein Condensation in a Gas of Sodium Atoms*. Physical Review Letters **75**, 3969–3973 (1995). See page: 1

[3] B. DeMarco and D. S. Jin. *Onset of Fermi Degeneracy in a Trapped Atomic Gas*. Science **285**, 1703–1706 (1999). See page: 1

[4] A. D. Cronin, J. Schmiedmayer, and D. E. Pritchard. *Optics and interferometry with atoms and molecules*. Reviews of Modern Physics **81**, 1051–1129 (2009). See page: 1

[5] J. Huang, S. Wu, H. Zhong, and C. Lee. *Quantum Metrology with Cold Atoms*. In *Annual Review of Cold Atoms and Molecules*, Volume 2, pages 365–415. World Scientific (2014). ISBN 978-981-4590-16-7 978-981-4590-17-4.

[6] A. D. Ludlow, M. M. Boyd, J. Ye, E. Peik, and P. Schmidt. *Optical atomic clocks*. Reviews of Modern Physics **87**, 637–701 (2015). See pages: 1, 3, 4, 9, 40, 46, 50

[7] C. Monroe. *Quantum information processing with atoms and photons*. Nature **416**, 238–246 (2002). See page: 1

[8] D. Jaksch, J. J. García-Ripoll, J. I. Cirac, and P. Zoller. *Quantum Computing with Cold Ions and Atoms: Theory*. In D. Bruß and G. Leuchs, editors, *Quantum Information*, pages 483–517. Wiley, 1$^{\text{st}}$ edition (2016). ISBN 978-3-527-41353-9 978-3-527-80578-5. See page: 1

[9] I. Bloch. *Ultracold quantum gases in optical lattices*. Nature Physics **1**, 23–30 (2005). See pages: 1, 19

[10] M. Lewenstein, A. Sanpera, V. Ahufinger, B. Damski, A. Sen(De), and U. Sen. *Ultracold atomic gases in optical lattices: mimicking condensed matter physics and beyond*. Advances in Physics **56**, 243–379 (2007).

[11] I. Bloch, J. Dalibard, and W. Zwerger. *Many-body physics with ultracold gases*. Reviews of Modern Physics **80**, 885–964 (2008). See pages: 1, 16, 19

[12] I. Bloch, J. Dalibard, and S. Nascimbène. *Quantum simulations with ultracold quantum gases*. Nature Physics **8**, 267–276 (2012). See pages: 1, 2, 19

[13] M. Lewenstein, A. Sanpera, and V. Ahufinger. *Ultracold Atoms in Optical Lattices: Simulating quantum many-body systems*. Oxford University Press (2012). ISBN 978-0-19-957312-7.

[14] C. Gross and I. Bloch. *Quantum simulations with ultracold atoms in optical lattices*. Science **357**, 995–1001 (2017). See pages: 1, 2, 19

[15] K. M. Jones, E. Tiesinga, P. D. Lett, and P. S. Julienne. *Ultracold photoassociation spectroscopy: Long-range molecules and atomic scattering*. Reviews of Modern Physics **78**, 483–535 (2006). See page: 1

[16] T. Köhler, K. Góral, and P. S. Julienne. *Production of cold molecules via magnetically tunable Feshbach resonances*. Reviews of Modern Physics **78**, 1311–1361 (2006).

[17] L. D. Carr, D. DeMille, R. V. Krems, and J. Ye. *Cold and ultracold molecules: science, technology and applications*. New Journal of Physics **11**, 055049 (2009).

[18] N. Balakrishnan. *Perspective: Ultracold molecules and the dawn of cold controlled chemistry*. The Journal of Chemical Physics **145**, 150901 (2016). See page: 1

[19] N. Goldman, J. C. Budich, and P. Zoller. *Topological quantum matter with ultracold gases in optical lattices*. Nature Physics **12**, 639–645 (2016). See page: 1

[20] M. Aidelsburger. *Artificial gauge fields and topology with ultracold atoms in optical lattices*. Journal of Physics B: Atomic, Molecular and Optical Physics **51**, 193001 (2018).

[21] N. Cooper, J. Dalibard, and I. Spielman. *Topological bands for ultracold atoms*. Reviews of Modern Physics **91**, 015005 (2019). See page: 1

[22] R. Grimm, M. Weidemüller, and Y. B. Ovchinnikov. *Optical Dipole Traps for Neutral Atoms*. In *Advances In Atomic, Molecular, and Optical Physics*, Volume 42, pages 95–170. Elsevier (2000). ISBN 978-0-12-003842-8. See page: 1

[23] P. Jessen and I. Deutsch. *Optical Lattices*. In *Advances In Atomic, Molecular, and Optical Physics*, Volume 37, pages 95–138. Elsevier (1996). ISBN 978-0-12-003837-4. See page: 1

[24] M. Greiner, O. Mandel, T. Esslinger, T. W. Hänsch, and I. Bloch. *Quantum phase transition from a superfluid to a Mott insulator in a gas of ultracold atoms*. Nature **415**, 39–44 (2002). See page: 1

[25] C. Becker, P. Soltan-Panahi, J. Kronjäger, S. Dörscher, K. Bongs, and K. Sengstock. *Ultracold quantum gases in triangular optical lattices*. New Journal of Physics **12**, 065025 (2010). See page: 1

[26] L. Tarruell, D. Greif, T. Uehlinger, G. Jotzu, and T. Esslinger. *Creating, moving and merging Dirac points with a Fermi gas in a tunable honeycomb lattice*. Nature **483**, 302–305 (2012). See page: 1

[27] G.-B. Jo, J. Guzman, C. K. Thomas, P. Hosur, A. Vishwanath, and D. M. Stamper-Kurn. *Ultracold Atoms in a Tunable Optical Kagome Lattice*. Physical Review Letters **108**, 045305 (2012). See page: 1

[28] G. Gauthier, T. A. Bell, A. B. Stilgoe, M. Baker, H. Rubinsztein-Dunlop, and T. W. Neely. *Dynamic high-resolution optical trapping of ultracold atoms*. In *Advances In Atomic, Molecular, and Optical Physics*, Volume 70, pages 1–101. Elsevier (2021). ISBN 978-0-12-824610-8. See page: 1

[29] W. S. Bakr, J. I. Gillen, A. Peng, S. Fölling, and M. Greiner. *A quantum gas microscope for detecting single atoms in a Hubbard-regime optical lattice*. Nature **462**, 74–77 (2009). See pages: 1, 30

[30] J. F. Sherson, C. Weitenberg, M. Endres, M. Cheneau, I. Bloch, and S. Kuhr. *Single-atom-resolved fluorescence imaging of an atomic Mott insulator*. Nature **467**, 68–72 (2010).

[31] C. Gross and W. S. Bakr. *Quantum gas microscopy for single atom and spin detection*. Nature Physics **17**, 1316–1323 (2021). See pages: 1, 2, 30

[32] A. M. Kaufman and K.-K. Ni. *Quantum science with optical tweezer arrays of ultracold atoms and molecules*. Nature Physics **17**, 1324–1333 (2021). See page: 1

[33] C. Chin, R. Grimm, P. Julienne, and E. Tiesinga. *Feshbach resonances in ultracold gases*. Reviews of Modern Physics **82**, 1225–1286 (2010). See pages: 1, 3, 13, 16, 18, 74, 77, 86, 90

[34] R. P. Feynman. *Simulating physics with computers*. International Journal of Theoretical Physics **21**, 467–488 (1982). See page: 1

[35] A. J. Daley, I. Bloch, C. Kokail, S. Flannigan, N. Pearson, M. Troyer, and P. Zoller. *Practical quantum advantage in quantum simulation*. Nature **607**, 667–676 (2022). See page: 1

[36] J. I. Cirac and P. Zoller. *Goals and opportunities in quantum simulation*. Nature Physics **8**, 264–266 (2012).

[37] I. Georgescu, S. Ashhab, and F. Nori. *Quantum simulation*. Reviews of Modern Physics **86**, 153–185 (2014).

[38] W. Hofstetter and T. Qin. *Quantum simulation of strongly correlated condensed matter systems*. Journal of Physics B: Atomic, Molecular and Optical Physics **51**, 082001 (2018). See page: 2

[39] F. Schäfer, T. Fukuhara, S. Sugawa, Y. Takasu, and Y. Takahashi. *Tools for quantum simulation with ultracold atoms in optical lattices*. Nature Reviews Physics **2**, 411–425 (2020). See page: 2

[40] E. Altman, K. R. Brown, G. Carleo, L. D. Carr, E. Demler, C. Chin, B. DeMarco, S. E. Economou, M. A. Eriksson, K.-M. C. Fu, M. Greiner, K. R. Hazzard, R. G. Hulet, A. J. Kollár, B. L. Lev, M. D. Lukin, R. Ma, X. Mi, S. Misra, C. Monroe, K. Murch, Z. Nazario, K.-K. Ni, A. C. Potter, P. Roushan, M. Saffman, M. Schleier-Smith, I. Siddiqi, R. Simmonds, M. Singh, I. Spielman, K. Temme, D. S. Weiss, J. Vučković, V. Vuletić, J. Ye, and M. Zwierlein. *Quantum Simulators: Architectures and Opportunities*. PRX Quantum **2**, 017003 (2021). See page: 1

[41] R. Blatt and C. F. Roos. *Quantum simulations with trapped ions*. Nature Physics **8**, 277–284 (2012). See page: 1

[42] C. Monroe, W. Campbell, L.-M. Duan, Z.-X. Gong, A. Gorshkov, P. Hess, R. Islam, K. Kim, N. Linke, G. Pagano, P. Richerme, C. Senko, and N. Yao. *Programmable quantum simulations of spin systems with trapped ions*. Reviews of Modern Physics **93**, 025001 (2021). See page: 1

[43] A. A. Houck, H. E. Türeci, and J. Koch. *On-chip quantum simulation with superconducting circuits*. Nature Physics **8**, 292–299 (2012). See page: 1

[44] A. Aspuru-Guzik and P. Walther. *Photonic quantum simulators*. Nature Physics **8**, 285–291 (2012). See page: 1

[45] A. Browaeys and T. Lahaye. *Many-body physics with individually controlled Rydberg atoms*. Nature Physics **16**, 132–142 (2020). See page: 1

[46] T. Esslinger. *Fermi-Hubbard Physics with Atoms in an Optical Lattice*. Annual Review of Condensed Matter Physics **1**, 129–152 (2010). See page: 2

[47] L. Tarruell and L. Sanchez-Palencia. *Quantum simulation of the Hubbard model with ultracold fermions in optical lattices*. Comptes Rendus Physique **19**, 365–393 (2018). See page: 2

[48] W. Hofstetter, J. I. Cirac, P. Zoller, E. Demler, and M. D. Lukin. *High-Temperature Superfluidity of Fermionic Atoms in Optical Lattices*. Physical Review Letters **89**, 220407 (2002). See page: 2

[49] P. A. Lee, N. Nagaosa, and X.-G. Wen. *Doping a Mott insulator: Physics of high-temperature superconductivity*. Reviews of Modern Physics **78**, 17–85 (2006). See page: 2

[50] E. H. Lieb and F. Y. Wu. *Absence of Mott Transition in an Exact Solution of the Short-Range, One-Band Model in One Dimension*. Physical Review Letters **20**, 1445–1448 (1968). See page: 2

[51] M. Suzuki, editor. *Quantum Monte Carlo methods in condensed matter physics*. World Scientific, Singapore ; River Edge, NJ (1993). ISBN 978-981-02-1659-7. See page: 2

[52] F. Becca and S. Sorella. *Quantum Monte Carlo Approaches for Correlated Systems*. Cambridge University Press, 1$^{\text{st}}$ edition (2017). ISBN 978-1-107-12993-1 978-1-316-41704-1. See page: 2

[53] A. Georges, G. Kotliar, W. Krauth, and M. J. Rozenberg. *Dynamical mean-field theory of strongly correlated fermion systems and the limit of infinite dimensions*. Reviews of Modern Physics **68**, 13–125 (1996). See page: 2

[54] D. Vollhardt. *Dynamical mean-field theory for correlated electrons*. Annalen der Physik **524**, 1–19 (2012). See page: 2

[55] R. Jördens, N. Strohmaier, K. Günter, H. Moritz, and T. Esslinger. *A Mott insulator of fermionic atoms in an optical lattice*. Nature **455**, 204–207 (2008). See page: 2

[56] U. Schneider, L. Hackermüller, S. Will, T. Best, I. Bloch, T. A. Costi, R. W. Helmes, D. Rasch, and A. Rosch. *Metallic and Insulating Phases of Repulsively Interacting Fermions in a 3D Optical Lattice*. Science **322**, 1520–1525 (2008). See page: 2

[57] R. A. Hart, P. M. Duarte, T.-L. Yang, X. Liu, T. Paiva, E. Khatami, R. T. Scalettar, N. Trivedi, D. A. Huse, and R. G. Hulet. *Observation of antiferromagnetic correlations in the Hubbard model with ultracold atoms*. Nature **519**, 211–214 (2015). See page: 2

[58] L. W. Cheuk, M. A. Nichols, K. R. Lawrence, M. Okan, H. Zhang, E. Khatami, N. Trivedi, T. Paiva, M. Rigol, and M. W. Zwierlein. *Observation of spatial charge and spin correlations in the 2D Fermi-Hubbard model*. Science **353**, 1260–1264 (2016).

[59] M. F. Parsons, A. Mazurenko, C. S. Chiu, G. Ji, D. Greif, and M. Greiner. *Site-resolved measurement of the spin-correlation function in the Fermi-Hubbard model*. Science **353**, 1253–1256 (2016).

[60] M. Boll, T. A. Hilker, G. Salomon, A. Omran, J. Nespolo, L. Pollet, I. Bloch, and C. Gross. *Spin- and density-resolved microscopy of antiferromagnetic correlations in Fermi-Hubbard chains*. Science **353**, 1257–1260 (2016).

[61] P. T. Brown, D. Mitra, E. Guardado-Sanchez, P. Schauß, S. S. Kondov, E. Khatami, T. Paiva, N. Trivedi, D. A. Huse, and W. S. Bakr. *Spin-imbalance in a 2D Fermi-Hubbard system*. Science **357**, 1385–1388 (2017).

[62] A. Mazurenko, C. S. Chiu, G. Ji, M. F. Parsons, M. Kanász-Nagy, R. Schmidt, F. Grusdt, E. Demler, D. Greif, and M. Greiner. *A cold-atom Fermi–Hubbard antiferromagnet*. Nature **545**, 462–466 (2017). See page: 2

[63] J. Kondo. *Resistance Minimum in Dilute Magnetic Alloys*. Progress of Theoretical Physics **32**, 37–49 (1964). See pages: 2, 22

[64] A. C. Hewson. *The Kondo Problem to Heavy Fermions*. Cambridge University Press, 1 edition (1993). ISBN 978-0-521-36382-2 978-0-521-59947-4 978-0-511-47075-2. See pages: 2, 3, 22, 53, 90

[65] G. R. Stewart. *Heavy-fermion systems*. Reviews of Modern Physics **56**, 755–787 (1984). See page: 2

[66] S. Jin, T. H. Tiefel, M. McCormack, R. A. Fastnacht, R. Ramesh, and L. H. Chen. *Thousandfold Change in Resistivity in Magnetoresistive La-Ca-Mn-O Films*. Science **264**, 413–415 (1994). See pages: 2, 22

[67] A. P. Ramirez. *Colossal magnetoresistance*. Journal of Physics: Condensed Matter **9**, 8171–8199 (1997). See pages: 2, 22

[68] S. G. Porsev, A. Derevianko, and E. N. Fortson. *Possibility of an optical clock using the $6^1S_0 \to 6^3P_0^o$ transition in ^{171,173}Yb atoms held in an optical lattice*. Physical Review A **69**, 021403 (2004). See pages: 2, 8, 9, 74

[69] A. V. Gorshkov, M. Hermele, V. Gurarie, C. Xu, P. S. Julienne, J. Ye, P. Zoller, E. Demler, M. D. Lukin, and A. M. Rey. *Two-orbital SU(N) magnetism with ultracold alkaline-earth atoms*. Nature Physics **6**, 289–295 (2010). See pages: 2, 3, 9, 10, 21, 30, 53, 61, 65, 69

[70] A. J. Daley. *Quantum computing and quantum simulation with group-II atoms*. Quantum Information Processing **10**, 865–884 (2011).

[71] C. He, E. Hajiyev, Z. Ren, B. Song, and G.-B. Jo. *Recent progresses of ultracold two-electron atoms*. Journal of Physics B: Atomic, Molecular and Optical Physics **52**, 102001 (2019).

[72] Y. Takahashi. *Quantum simulation of quantum many-body systems with ultracold two-electron atoms in an optical lattice*. Proceedings of the Japan Academy, Series B **98**, 141–160 (2022). See page: 2

[73] F. Scazza, C. Hofrichter, M. Höfer, P. C. De Groot, I. Bloch, and S. Fölling. *Observation of two-orbital spin-exchange interactions with ultracold SU(N)-symmetric fermions*. Nature Physics **10**, 779–784 (2014). See pages: 2, 3, 15, 21, 53, 61, 63, 65, 66, 68, 69

[74] G. Cappellini, M. Mancini, G. Pagano, P. Lombardi, L. Livi, M. Siciliani de Cumis, P. Cancio, M. Pizzocaro, D. Calonico, F. Levi, C. Sias, J. Catani, M. Inguscio, and L. Fallani. *Direct Observation of Coherent Interorbital Spin-Exchange Dynamics*. Physical Review Letters **113**, 120402 (2014). See pages: 59, 60

[75] L. Riegger, N. Darkwah Oppong, M. Höfer, D. Fernandes, I. Bloch, and S. Fölling. *Localized Magnetic Moments with Tunable Spin Exchange in a Gas of Ultracold Fermions*. Physical Review Letters **120**, 143601 (2018). See pages: 2, 3, 21, 65, 68, 69, 89, 90

[76] K. Ono, Y. Amano, T. Higomoto, Y. Saito, and Y. Takahashi. *Observation of spin-exchange dynamics between itinerant and localized Yb 171 atoms*. Physical Review A **103**, L041303 (2021). See pages: 2, 89

[77] A. Heinz, A. Park, N. Šantić, J. Trautmann, S. Porsev, M. Safronova, I. Bloch, and S. Blatt. *State-Dependent Optical Lattices for the Strontium Optical Qubit*. Physical Review Letters **124**, 203201 (2020). See page: 2

[78] M. Kanász-Nagy, Y. Ashida, T. Shi, C. P. Moca, T. N. Ikeda, S. Fölling, J. I. Cirac, G. Zaránd, and E. A. Demler. *Exploring the anisotropic Kondo model in and out of equilibrium with alkaline-earth atoms*. Physical Review B **97**, 155156 (2018). See pages: 2, 61, 69

[79] M. Nakagawa, N. Kawakami, and M. Ueda. *Non-Hermitian Kondo Effect in Ultracold Alkaline-Earth Atoms*. Physical Review Letters **121**, 203001 (2018).

[80] S. Goto and I. Danshita. *Quasiexact Kondo Dynamics of Fermionic Alkaline-Earth-Like Atoms at Finite Temperatures*. Physical Review Letters **123**, 143002 (2019).

[81] R. Zhang and P. Zhang. *Tight-binding Kondo model and spin-exchange collision rate of alkaline-earth-metal atoms in a mixed-dimensional optical lattice*. Physical Review A **101**, 013636 (2020). See page: 2

[82] M. Foss-Feig, M. Hermele, and A. M. Rey. *Probing the Kondo lattice model with alkaline-earth-metal atoms*. Physical Review A **81**, 051603 (2010). See pages: 2, 3, 30, 53

[83] M. Foss-Feig, M. Hermele, V. Gurarie, and A. M. Rey. *Heavy fermions in an optical lattice*. Physical Review A **82**, 053624 (2010).

[84] J. Silva-Valencia and A. M. C. Souza. *Ground state of alkaline-earth fermionic atoms in one-dimensional optical lattices*. The European Physical Journal B **85**, 5 (2012). See pages: 2, 3, 30, 53, 61, 69

[85] M. A. Cazalilla, A. F. Ho, and M. Ueda. *Ultracold gases of ytterbium: ferromagnetism and Mott states in an SU(6) Fermi system*. New Journal of Physics **11**, 103033 (2009). See page: 2

[86] S. Taie, Y. Takasu, S. Sugawa, R. Yamazaki, T. Tsujimoto, R. Murakami, and Y. Takahashi. *Realization of a* SU(2) × SU(6) *System of Fermions in a Cold Atomic Gas*. Physical Review Letters **105**, 190401 (2010). See pages: 3, 30

[87] X. Zhang, M. Bishof, S. L. Bromley, C. V. Kraus, M. S. Safronova, P. Zoller, A. M. Rey, and J. Ye. *Spectroscopic observation of SU(N)-symmetric interactions in Sr orbital magnetism*. Science **345**, 1467–1473 (2014). See pages: 3, 69

[88] S. Taie, R. Yamazaki, S. Sugawa, and Y. Takahashi. *An SU(6) Mott insulator of an atomic Fermi gas realized by large-spin Pomeranchuk cooling*. Nature Physics **8**, 825–830 (2012). See page: 3

[89] C. Hofrichter, L. Riegger, F. Scazza, M. Höfer, D. R. Fernandes, I. Bloch, and S. Fölling. *Direct Probing of the Mott Crossover in the SU(N) Fermi-Hubbard Model*. Physical Review X **6**, 021030 (2016). See pages: 10, 54

[90] G. Pasqualetti, PhD thesis, Ludwigs-Maximilians-Universität München, in preparation. See pages: 3, 10

[91] C. Honerkamp and W. Hofstetter. *Ultracold Fermions and the SU(N) Hubbard Model*. Physical Review Letters **92**, 170403 (2004). See pages: 3, 10

[92] T. A. Tóth, A. M. Läuchli, F. Mila, and K. Penc. *Three-Sublattice Ordering of the SU(3) Heisenberg Model of Three-Flavor Fermions on the Square and Cubic Lattices*. Physical Review Letters **105**, 265301 (2010).

[93] P. Corboz, M. Lajkó, A. M. Läuchli, K. Penc, and F. Mila. *Spin-Orbital Quantum Liquid on the Honeycomb Lattice*. Physical Review X **2**, 041013 (2012).

[94] P. Nataf and F. Mila. *Exact Diagonalization of Heisenberg SU(N) Models*. Physical Review Letters **113**, 127204 (2014). See pages: 3, 10

[95] Y. Takasu, K. Maki, K. Komori, T. Takano, K. Honda, M. Kumakura, T. Yabuzaki, and Y. Takahashi. *Spin-Singlet Bose-Einstein Condensation of Two-Electron Atoms*. Physical Review Letters **91**, 040404 (2003). See page: 3

[96] M. Kitagawa, K. Enomoto, K. Kasa, Y. Takahashi, R. Ciuryło, P. Naidon, and P. S. Julienne. *Two-color photoassociation spectroscopy of ytterbium atoms and the precise determinations of s-wave scattering lengths*. Physical Review A **77**, 012719 (2008). See pages: 3, 7, 10, 15, 30, 60, 63, 68, 89

[97] R. Zhang, Y. Cheng, P. Zhang, and H. Zhai. *Controlling the interaction of ultracold alkaline-earth atoms*. Nature Reviews Physics **2**, 213–220 (2020). See page: 3

[98] P. Coleman. *Heavy Fermions: Electrons at the Edge of Magnetism*. In H. Kronmüller and S. Parkin, editors, *Handbook of Magnetism and Advanced Magnetic Materials*, pages 95–148. John Wiley & Sons, Ltd, Chichester, UK (2007). ISBN 978-0-470-02217-7 978-0-470-02218-4. See pages: 3, 22, 53, 90

[99] W. F. McGrew, X. Zhang, R. J. Fasano, S. A. Schäffer, K. Beloy, D. Nicolodi, R. C. Brown, N. Hinkley, G. Milani, M. Schioppo, T. H. Yoon, and A. D. Ludlow. *Atomic clock performance enabling geodesy below the centimetre level*. Nature **564**, 87–90 (2018). See pages: 3, 4, 40

[100] T. Kobayashi, D. Akamatsu, K. Hosaka, Y. Hisai, M. Wada, H. Inaba, T. Suzuyama, F.-L. Hong, and M. Yasuda. *Demonstration of the nearly continuous operation of an ^{171}Yb optical lattice clock for half a year*. Metrologia **57**, 065021 (2020). See page: 3

[101] A. Jenkins, J. W. Lis, A. Senoo, W. F. McGrew, and A. M. Kaufman. *Ytterbium Nuclear-Spin Qubits in an Optical Tweezer Array*. Physical Review X **12**, 021027 (2022). See page: 3

[102] S. Ma, A. P. Burgers, G. Liu, J. Wilson, B. Zhang, and J. D. Thompson. *Universal Gate Operations on Nuclear Spin Qubits in an Optical Tweezer Array of Yb 171 Atoms*. Physical Review X **12**, 021028 (2022). See page: 3

[103] R. Zhang, Y. Cheng, H. Zhai, and P. Zhang. *Orbital Feshbach Resonance in Alkali-Earth Atoms*. Physical Review Letters **115**, 135301 (2015). See pages: 3, 18, 71, 77

[104] H. Zhai. *Ultracold Atomic Physics*. Cambridge University Press, 1 edition (2021). ISBN 978-1-108-59521-6 978-1-108-49868-5. See page: 3

[105] M. Höfer, L. Riegger, F. Scazza, C. Hofrichter, D. Fernandes, M. Parish, J. Levinsen, I. Bloch, and S. Fölling. *Observation of an Orbital Interaction-Induced Feshbach Resonance in Yb 173*. Physical Review Letters **115**, 265302 (2015). See pages: 3, 18, 71, 75, 77, 78, 79, 82, 86, 90, 91

[106] G. Pagano, M. Mancini, G. Cappellini, L. Livi, C. Sias, J. Catani, M. Inguscio, and L. Fallani. *Strongly Interacting Gas of Two-Electron Fermions at an Orbital Feshbach Resonance*. Physical Review Letters **115**, 265301 (2015). See pages: 3, 18, 71, 77, 78, 90

[107] J. Xu, R. Zhang, Y. Cheng, P. Zhang, R. Qi, and H. Zhai. *Reaching a Fermi-superfluid state near an orbital Feshbach resonance*. Physical Review A **94**, 033609 (2016). See pages: 3, 90

[108] M. Iskin. *Two-band superfluidity and intrinsic Josephson effect in alkaline-earth-metal Fermi gases across an orbital Feshbach resonance*. Physical Review A **94**, 011604 (2016).

[109] L. He, J. Wang, S.-G. Peng, X.-J. Liu, and H. Hu. *Strongly correlated Fermi superfluid near an orbital Feshbach resonance: Stability, equation of state, and Leggett mode*. Physical Review A **94**, 043624 (2016).

[110] M. Iskin. *Trapped Yb 173 Fermi gas across an orbital Feshbach resonance*. Physical Review A **95**, 013618 (2017).

[111] Y.-C. Zhang, S. Ding, and S. Zhang. *Collective modes in a two-band superfluid of ultracold alkaline-earth-metal atoms close to an orbital Feshbach resonance*. Physical Review A **95**, 041603 (2017).

[112] T.-S. Deng, W. Zhang, and W. Yi. *Tuning Feshbach resonances in cold atomic gases with interchannel coupling*. Physical Review A **96**, 050701 (2017).

[113] S. Wang, J.-S. Pan, X. Cui, W. Zhang, and W. Yi. *Topological Fulde-Ferrell states in alkaline-earth-metal-like atoms near an orbital Feshbach resonance*. Physical Review A **95**, 043634 (2017).

[114] H. Zhang, F. Badshah, A. Basit, and G.-Q. Ge. *Fermi gas of orbital Feshbach resonance in synthetic 1D+1 dimensional optical lattice*. Laser Physics Letters **15**, 115501 (2018).

[115] S. N. Klimin, J. Tempere, and M. V. Milošević. *Diversified vortex phase diagram for a rotating trapped two-band Fermi gas in the BCS-BEC crossover*. New Journal of Physics **20**, 025010 (2018).

[116] P. Zou, L. He, X.-J. Liu, and H. Hu. *Strongly interacting Sarma superfluid near orbital Feshbach resonances*. Physical Review A **97**, 043616 (2018).

[117] E. K. Laird, Z.-Y. Shi, M. M. Parish, and J. Levinsen. *Frustrated orbital Feshbach resonances in a Fermi gas*. Physical Review A **101**, 022707 (2020). See pages: 3, 90

[118] N. Darkwah Oppong, L. Riegger, O. Bettermann, M. Höfer, J. Levinsen, M. Parish, I. Bloch, and S. Fölling. *Observation of Coherent Multiorbital Polarons in a Two-Dimensional Fermi Gas*. Physical Review Letters **122**, 193604 (2019). See pages: 3, 34, 37, 52, 69, 90

[119] N. Darkwah Oppong, G. Pasqualetti, O. Bettermann, P. Zechmann, M. Knap, I. Bloch, and S. Fölling. *Probing Transport and Slow Relaxation in the Mass-Imbalanced Fermi-Hubbard Model*. Physical Review X **12**, 031026 (2022). See pages: 3, 22, 77, 91

[120] R. Zhang, D. Zhang, Y. Cheng, W. Chen, P. Zhang, and H. Zhai. *Kondo effect in alkaline-earth-metal atomic gases with confinement-induced resonances*. Physical Review A **93**, 043601 (2016). See pages: 3, 90

[121] Y. Cheng, R. Zhang, P. Zhang, and H. Zhai. *Enhancing Kondo coupling in alkaline-earth-metal atomic gases with confinement-induced resonances in mixed dimensions*. Physical Review A **96**, 063605 (2017). See pages: 3, 90

[122] N. Poli, C. W. Oates, P. Gill, and G. M. Tino. *Optical atomic clocks*. La Rivista del Nuovo Cimento **36**, 555–624 (2013). See page: 4

[123] T. Bothwell, D. Kedar, E. Oelker, J. M. Robinson, S. L. Bromley, W. L. Tew, J. Ye, and C. J. Kennedy. *JILA SrI optical lattice clock with uncertainty of* 2.0×10^{-18}. Metrologia **56**, 065004 (2019). See pages: 4, 40

[124] S. Kolkowitz, I. Pikovski, N. Langellier, M. Lukin, R. Walsworth, and J. Ye. *Gravitational wave detection with optical lattice atomic clocks*. Physical Review D **94**, 124043 (2016). See page: 4

[125] M. Takamoto, I. Ushijima, N. Ohmae, T. Yahagi, K. Kokado, H. Shinkai, and H. Katori. *Test of general relativity by a pair of transportable optical lattice clocks*. Nature Photonics **14**, 411–415 (2020).

[126] T. Bothwell, C. J. Kennedy, A. Aeppli, D. Kedar, J. M. Robinson, E. Oelker, A. Staron, and J. Ye. *Resolving the gravitational redshift across a millimetre-scale atomic sample*. Nature **602**, 420–424 (2022).

[127] X. Zheng, J. Dolde, V. Lochab, B. N. Merriman, H. Li, and S. Kolkowitz. *Differential clock comparisons with a multiplexed optical lattice clock*. Nature **602**, 425–430 (2022). See page: 4

[128] P. Wcisło, P. Ablewski, K. Beloy, S. Bilicki, M. Bober, R. Brown, R. Fasano, R. Ciuryło, H. Hachisu, T. Ido, J. Lodewyck, A. Ludlow, W. McGrew, P. Morzyński, D. Nicolodi, M. Schioppo, M. Sekido, R. Le Targat, P. Wolf, X. Zhang, B. Zjawin, and M. Zawada. *New bounds on dark matter coupling from a global network of optical atomic clocks*. Science Advances **4**, eaau4869 (2018). See page: 4

[129] C. J. Kennedy, E. Oelker, J. M. Robinson, T. Bothwell, D. Kedar, W. R. Milner, G. E. Marti, A. Derevianko, and J. Ye. *Precision Metrology Meets Cosmology: Improved Constraints on Ultralight Dark Matter from Atom-Cavity Frequency Comparisons*. Physical Review Letters **125**, 201302 (2020). See page: 4

[130] M. Safronova, D. Budker, D. DeMille, D. F. J. Kimball, A. Derevianko, and C. W. Clark. *Search for new physics with atoms and molecules*. Reviews of Modern Physics **90**, 025008 (2018). See page: 4

[131] F. Riehle. *Towards a redefinition of the second based on optical atomic clocks*. Comptes Rendus Physique **16**, 506–515 (2015). See pages: 4, 9

[132] T. Zelevinsky, S. Blatt, M. M. Boyd, G. K. Campbell, A. D. Ludlow, and J. Ye. *Highly Coherent Spectroscopy of Ultracold Atoms and Molecules in Optical Lattices*. ChemPhysChem **9**, 375–382 (2008). See pages: 4, 91

[133] S. S. Kondov, C.-H. Lee, K. H. Leung, C. Liedl, I. Majewska, R. Moszynski, and T. Zelevinsky. *Molecular lattice clock with long vibrational coherence*. Nature Physics **15**, 1118–1122 (2019). See pages: 4, 86, 91

[134] T. Zelevinsky, S. Kotochigova, and J. Ye. *Precision Test of Mass-Ratio Variations with Lattice-Confined Ultracold Molecules*. Physical Review Letters **100**, 043201 (2008). See pages: 4, 86, 91

[135] M. Borkowski. *Optical Lattice Clocks with Weakly Bound Molecules*. Physical Review Letters **120**, 083202 (2018). See pages: 4, 87, 91

[136] M. Berglund and M. E. Wieser. *Isotopic compositions of the elements 2009 (IUPAC Technical Report)*. Pure and Applied Chemistry **83**, 397–410 (2011). See page: 7

[137] K. Beloy, J. A. Sherman, N. D. Lemke, N. Hinkley, C. W. Oates, and A. D. Ludlow. *Determination of the $5d6s\,^3D_1$ state lifetime and blackbody-radiation clock shift in Yb*. Physical Review A **86**, 051404 (2012). See pages: 8, 9

[138] Y. Takasu, K. Komori, K. Honda, M. Kumakura, T. Yabuzaki, and Y. Takahashi. *Photoassociation Spectroscopy of Laser-Cooled Ytterbium Atoms*. Physical Review Letters **93**, 123202 (2004). See page: 8

[139] J. W. Cho, H.-g. Lee, S. Lee, J. Ahn, W.-K. Lee, D.-H. Yu, S. K. Lee, and C. Y. Park. *Optical repumping of triplet- P states enhances magneto-optical trapping of ytterbium atoms*. Physical Review A **85**, 035401 (2012). See page: 8

[140] M. M. Boyd, T. Zelevinsky, A. D. Ludlow, S. Blatt, T. Zanon-Willette, S. M. Foreman, and J. Ye. *Nuclear spin effects in optical lattice clocks*. Physical Review A **76**, 022510 (2007). See pages: 9, 49, 50, 52

[141] G. Pasqualetti. *Isotopic mixtures of ytterbium for quantum simulation of Kondo physics*. Master's thesis, Ludwig-Maximilians-Universität München (2018). See page: 31

[142] L. Riegger. *Interorbital spin exchange in a state-dependent optical lattice*. PhD thesis, Ludwig-Maximilians-Universität München (2019). See pages: 11, 27, 29, 31, 33

[143] V. A. Dzuba and A. Derevianko. *Dynamic polarizabilities and related properties of clock states of the ytterbium atom*. Journal of Physics B: Atomic, Molecular and Optical Physics **43**, 074011 (2010). See page: 11

[144] C. Pethick and H. Smith. *Bose-Einstein condensation in dilute gases*. Cambridge University Press, Cambridge ; New York, 2nd ed edition (2008). ISBN 978-0-521-84651-6. See page: 13

[145] V. V. Flambaum, G. F. Gribakin, and C. Harabati. *Analytical calculation of cold-atom scattering*. Physical Review A **59**, 1998–2005 (1999). See pages: 14, 90

[146] M. Greiner. *Ultracold quantum gases in three-dimensional optical lattice potentials*. PhD thesis, Ludwig-Maximilians-Universität München (2003). See page: 19

[147] S. Doniach. *The Kondo lattice and weak antiferromagnetism*. Physica B+C **91**, 231–234 (1977). See page: 21

[148] W. de Haas, J. de Boer, and G. van dën Berg. *The electrical resistance of gold, copper and lead at low temperatures*. Physica **1**, 1115–1124 (1934). See page: 22

[149] J. J. García-Ripoll, S. Dürr, N. Syassen, D. M. Bauer, M. Lettner, G. Rempe, and J. I. Cirac. *Dissipation-induced hard-core boson gas in an optical lattice*. New Journal of Physics **11**, 013053 (2009). See page: 24

[150] T. Busch, B.-G. Englert, K. Rzażewski, and M. Wilkens. *Two Cold Atoms in a Harmonic Trap*. Foundations of Physics **28**, 549–559 (1998). See pages: 24, 72, 74, 90

[151] K. Huang and C. N. Yang. *Quantum-Mechanical Many-Body Problem with Hard-Sphere Interaction*. Physical Review **105**, 767–775 (1957). See page: 24

[152] F. Scazza. *Probing SU(N)-symmetric orbital interactions with ytterbium Fermi gases in optical lattices*. PhD thesis, Ludwig-Maximilians-Universität München (2015). See pages: 27, 32, 33, 37, 39, 56

[153] C. Hofrichter. *Probing the SU(N) Fermi-Hubbard model with ytterbium atoms in an optical lattice*. PhD thesis, Ludwig-Maximilians-Universität München (2016). See pages: 34, 54

[154] M. Höfer. *A two-orbital quantum gas with tunable interactions*. PhD thesis, Ludwig-Maximilians-Universität München (2017). See pages: 74, 75, 79

[155] N. Darkwah Oppong. *Probing many-body physics with multiorbital quantum gases*. PhD thesis, Ludwig-Maximilians-Universität München (2021). See page: 27

[156] E. Haller, J. Hudson, A. Kelly, D. A. Cotta, B. Peaudecerf, G. D. Bruce, and S. Kuhr. *Single-atom imaging of fermions in a quantum-gas microscope*. Nature Physics **11**, 738–742 (2015). See page: 30

[157] L. W. Cheuk, M. A. Nichols, M. Okan, T. Gersdorf, V. V. Ramasesh, W. S. Bakr, T. Lompe, and M. W. Zwierlein. *Quantum-Gas Microscope for Fermionic Atoms*. Physical Review Letters **114**, 193001 (2015). See page: 30

[158] A. Impertro. *Preparation and Study of 1D and 2D Many-Body Systems with Fermionic Ytterbium*. Master's thesis, Ludwig-Maximilians-Universität München (2020). See page: 30

[159] T. Fukuhara, Y. Takasu, S. Sugawa, and Y. Takahashi. *Quantum Degenerate Fermi Gases of Ytterbium Atoms*. Journal of Low Temperature Physics **148**, 441–445 (2007). See page: 30

[160] G. E. Marti, R. B. Hutson, A. Goban, S. L. Campbell, N. Poli, and J. Ye. *Imaging optical frequencies with 100 μHz precision and 1.1 μm resolution*. Physical Review Letters **120**, 103201 (2018). See page: 32

[161] A. Impertro. *Improvement of a laser system to drive the ultranarrow clock transition in ^{173}Yb*. Technical report, Ludwig-Maximilians-Universität München (2019). See page: 33

[162] R. W. P. Drever, J. L. Hall, F. V. Kowalski, J. Hough, G. M. Ford, A. J. Munley, and H. Ward. *Laser phase and frequency stabilization using an optical resonator*. Applied Physics B Photophysics and Laser Chemistry **31**, 97–105 (1983). See page: 33

[163] E. D. Black. *An introduction to Pound–Drever–Hall laser frequency stabilization*. American Journal of Physics **69**, 79–87 (2001). See page: 33

[164] P. Ketterer. *A stable laser setup for the 578 nm clock transition of Ytterbium*. Master's thesis, Johannes Gutenberg Universität Mainz (2012). See page: 33

[165] W. Ketterle, D. S. Durfee, and D. M. Stamper-kurn. *Making, probing and understanding Bose-Einstein condensates*. In *Proceedings of the International School of Physics "Enrico Fermi", Course CXL, edited by M. Inguscio, S. Stringari and C.E. Wieman*, pages 67–176. IOS Press, Amsterdam (1999). See pages: 34, 39

[166] C.-L. Hung, X. Zhang, L.-C. Ha, S.-K. Tung, N. Gemelke, and C. Chin. *Extracting density–density correlations from in situ images of atomic quantum gases*. New Journal of Physics **13**, 075019 (2011). See page: 34

[167] G. Reinaudi, T. Lahaye, Z. Wang, and D. Guéry-Odelin. *Strong saturation absorption imaging of dense clouds of ultracold atoms*. Optics Letters **32**, 3143 (2007). See pages: 34, 35, 36

[168] G. Pasqualetti. *Design and characterization of a repump laser for clock state detection using the $^3P_0 \to {}^3D_1$ transition in ^{173}Yb*. Technical report, Ludwig-Maximilians Universität München (2017). See page: 35

[169] B. Hundt. *Optical Potentials for the Realization of Dissipative Fermi-Hubbard Models with Ultracold Ytterbium Atoms*. PhD thesis, Universität Hamburg (2016). See page: 35

[170] W. Gerlach and O. Stern. *Der experimentelle Nachweis der Richtungsquantelung im Magnetfeld*. Zeitschrift für Physik **9**, 349–352 (1922). See page: 39

[171] T. Sleator, T. Pfau, V. Balykin, O. Carnal, and J. Mlynek. *Experimental demonstration of the optical Stern-Gerlach effect*. Physical Review Letters **68**, 1996–1999 (1992). See page: 39

[172] M. O. Scully and M. S. Zubairy. *Quantum Optics*. Cambridge University Press, 1$^\text{st}$ edition (1997). ISBN 978-0-521-43595-6 978-0-521-43458-4 978-0-511-81399-3. See page: 40

[173] J. C. Slater. *Atomic Radii in Crystals*. The Journal of Chemical Physics **41**, 3199–3204 (1964). See page: 40

[174] C. Gerry and P. Knight. *Introductory Quantum Optics*. Cambridge University Press, 1 edition (2004). ISBN 978-0-521-52735-4 978-0-521-82035-6 978-0-511-79123-9. See page: 40

[175] R. H. Dicke. *The Effect of Collisions upon the Doppler Width of Spectral Lines*. Physical Review **89**, 472–473 (1953). See page: 43

[176] T. Ido and H. Katori. *Recoil-Free Spectroscopy of Neutral Sr Atoms in the Lamb-Dicke Regime*. Physical Review Letters **91**, 053001 (2003). See page: 43

[177] H. Katori, M. Takamoto, V. G. Pal'chikov, and V. D. Ovsiannikov. *Ultrastable Optical Clock with Neutral Atoms in an Engineered Light Shift Trap*. Physical Review Letters **91**, 173005 (2003). See pages: 43, 46

[178] D. Leibfried, R. Blatt, C. Monroe, and D. Wineland. *Quantum dynamics of single trapped ions*. Reviews of Modern Physics **75**, 281–324 (2003). See pages: 43, 44

[179] J. Eschner, G. Morigi, F. Schmidt-Kaler, and R. Blatt. *Laser cooling of trapped ions*. Journal of the Optical Society of America B **20**, 1003 (2003). See page: 43

[180] J. J. Sakurai and J. Napolitano. *Modern Quantum Mechanics*. Cambridge University Press, 3rd edition (2020). ISBN 978-1-108-58728-0 978-1-108-47322-4. See page: 44

[181] E. Jaynes and F. Cummings. *Comparison of quantum and semiclassical radiation theories with application to the beam maser*. Proceedings of the IEEE **51**, 89–109 (1963). See page: 44

[182] S. Haroche and J.-M. Raimond. *Exploring the Quantum*. Oxford University Press (2006). ISBN 978-0-19-850914-1. See page: 44

[183] D. J. Wineland and W. M. Itano. *Laser cooling of atoms*. Physical Review A **20**, 1521–1540 (1979). See page: 45

[184] D. A. Steck. *Quantum and Atom Optics* (2007). Available online at `http://steck.us/teaching` (revision 0.13.11, 7 April 2022). See page: 46

[185] J. Ye, H. J. Kimble, and H. Katori. *Quantum State Engineering and Precision Metrology Using State-Insensitive Light Traps*. Science **320**, 1734–1738 (2008). See page: 46

[186] N. Lemke, A. Ludlow, Z. Barber, T. Fortier, S. Diddams, Y. Jiang, S. Jefferts, T. Heavner, T. Parker, and C. Oates. *Spin-1/2 Optical Lattice Clock*. Physical Review Letters **103**, 063001 (2009). See pages: 46, 52

[187] R. Jáuregui, N. Poli, G. Roati, and G. Modugno. *Anharmonic parametric excitation in optical lattices*. Physical Review A **64**, 033403 (2001). See page: 47

[188] O. Bettermann, N. D. Oppong, G. Pasqualetti, L. Riegger, I. Bloch, and S. Fölling. *Clock-line photoassociation of strongly bound dimers in a magic-wavelength lattice*. arXiv:2003.10599 (2020). See pages: 47, 51, 58, 60, 62, 64, 66, 73, 84, 85

[189] M. Köhl. *Thermometry of fermionic atoms in an optical lattice*. Physical Review A **73**, 031601 (2006). See pages: 48, 54

[190] J. E. Sansonetti and W. C. Martin. *Handbook of Basic Atomic Spectroscopic Data*. Journal of Physical and Chemical Reference Data **34**, 1559–2259 (2005). See page: 49

[191] M. M. Boyd, T. Zelevinsky, A. D. Ludlow, S. M. Foreman, S. Blatt, T. Ido, and J. Ye. *Optical Atomic Coherence at the 1-Second Time Scale*. Science **314**, 1430–1433 (2006). See page: 49

[192] A. Taichenachev, V. Yudin, C. Oates, C. Hoyt, Z. Barber, and L. Hollberg. *Magnetic Field-Induced Spectroscopy of Forbidden Optical Transitions with Application to Lattice-Based Optical Atomic Clocks*. Physical Review Letters **96**, 083001 (2006). See pages: 50, 52

[193] N. D. Lemke. *Optical Lattice Clock with Spin-1/2 Ytterbium Atoms*. PhD thesis, University of Colorado, Boulder (2012). See page: 52

[194] K. Ono, J. Kobayashi, Y. Amano, K. Sato, and Y. Takahashi. *Antiferromagnetic interorbital spin-exchange interaction of* ^{171}Yb. Physical Review A **99**, 032707 (2019). See pages: 52, 58, 59, 61, 68, 69, 89

[195] N. Poli, Z. W. Barber, N. D. Lemke, C. W. Oates, L. S. Ma, J. E. Stalnaker, T. M. Fortier, S. A. Diddams, L. Hollberg, J. C. Bergquist, A. Brusch, S. Jefferts, T. Heavner, and T. Parker. *Frequency evaluation of the doubly forbidden* $^1S_0 \rightarrow {}^3P_0$ *transition in bosonic* ^{174}Yb. Physical Review A **77**, 050501 (2008). See page: 52

[196] K. Kugel and D. I. Khomskii. *Crystal structure and magnetic properties of substances with orbital degeneracy*. Soviet Physics - JETP **37**, 725–730 (1973). See page: 53

[197] M. A. Cazalilla and A. M. Rey. *Ultracold Fermi gases with emergent SU(N) symmetry*. Reports on Progress in Physics **77**, 124401 (2014). See page: 53

[198] B. Abeln, K. Sponselee, M. Diem, N. Pintul, K. Sengstock, and C. Becker. *Interorbital interactions in an* $SU(2) \otimes SU(6)$-*symmetric Fermi-Fermi mixture*. Physical Review A **103**, 033315 (2021). See pages: 58, 59, 61, 68, 69, 89

[199] A. D. Ludlow, N. D. Lemke, J. A. Sherman, C. W. Oates, G. Quéméner, J. von Stecher, and A. M. Rey. *Cold-collision-shift cancellation and inelastic scattering in a Yb optical lattice clock*. Physical Review A **84**, 052724 (2011). See pages: 65, 67, 68

[200] A. Traverso, R. Chakraborty, Y. N. Martinez de Escobar, P. G. Mickelson, S. B. Nagel, M. Yan, and T. C. Killian. *Inelastic and elastic collision rates for triplet states of ultracold strontium*. Physical Review A **79**, 060702 (2009). See pages: 65, 68, 69

[201] D. A. Butts and D. S. Rokhsar. *Trapped Fermi gases*. Physical Review A **55**, 4346–4350 (1997). See page: 67

[202] A. J. Moerdijk, B. J. Verhaar, and A. Axelsson. *Resonances in ultracold collisions of Li 6 , Li 7 , and Na 23*. Physical Review A **51**, 4852–4861 (1995). See page: 74

[203] J. Levinsen and M. M. Parish. Private Communication. See page: 77

[204] F. Ferlaino, S. Knoop, and R. Grimm. *Ultracold Feshbach Molecules*. In *Cold Molecules: Theory, Experiment, Applications*, pages 319–354. CRC Press, USA, first edition (2009). See page: 86

[205] S. Kotochigova, T. Zelevinsky, and J. Ye. *Prospects for application of ultracold Sr 2 molecules in precision measurements*. Physical Review A **79**, 012504 (2009). See pages: 87, 91

[206] G. Cappellini, L. Livi, L. Franchi, D. Tusi, D. Benedicto Orenes, M. Inguscio, J. Catani, and L. Fallani. *Coherent Manipulation of Orbital Feshbach Molecules of Two-Electron Atoms*. Physical Review X **9**, 011028 (2019). See pages: 87, 91

[207] I. V. Borzenets, J. Shim, J. C. H. Chen, A. Ludwig, A. D. Wieck, S. Tarucha, H.-S. Sim, and M. Yamamoto. *Observation of the Kondo screening cloud*. Nature **579**, 210–213 (2020). See page: 90

[208] N. D. Mathur, F. M. Grosche, S. R. Julian, I. R. Walker, D. M. Freye, R. K. W. Haselwimmer, and G. G. Lonzarich. *Magnetically mediated superconductivity in heavy fermion compounds*. Nature **394**, 39–43 (1998). See page: 90

[209] M. Randeria and E. Taylor. *Crossover from Bardeen-Cooper-Schrieffer to Bose-Einstein Condensation and the Unitary Fermi Gas*. Annual Review of Condensed Matter Physics **5**, 209–232 (2014). See page: 90

[210] C. Chin, M. Bartenstein, A. Altmeyer, S. Riedl, S. Jochim, J. H. Denschlag, and R. Grimm. *Observation of the Pairing Gap in a Strongly Interacting Fermi Gas*. Science **305**, 1128–1130 (2004).

[211] M. W. Zwierlein, C. A. Stan, C. H. Schunck, S. M. F. Raupach, A. J. Kerman, and W. Ketterle. *Condensation of Pairs of Fermionic Atoms near a Feshbach Resonance*. Physical Review Letters **92**, 120403 (2004).

[212] C. A. Regal, M. Greiner, and D. S. Jin. *Observation of Resonance Condensation of Fermionic Atom Pairs*. Physical Review Letters **92**, 040403 (2004). See page: 90

[213] K. E. Strecker, G. B. Partridge, and R. G. Hulet. *Conversion of an Atomic Fermi Gas to a Long-Lived Molecular Bose Gas*. Physical Review Letters **91**, 080406 (2003). See page: 90

[214] S. Nascimbène, N. Navon, K. J. Jiang, F. Chevy, and C. Salomon. *Exploring the thermodynamics of a universal Fermi gas*. Nature **463**, 1057–1060 (2010). See page: 90

[215] N. Navon, S. Nascimbene, F. Chevy, and C. Salomon. *The Equation of State of a Low-Temperature Fermi Gas with Tunable Interactions*. Science **328**, 729–732 (2010).

[216] M. J. H. Ku, A. T. Sommer, L. W. Cheuk, and M. W. Zwierlein. *Revealing the Superfluid Lambda Transition in the Universal Thermodynamics of a Unitary Fermi Gas*. Science **335**, 563–567 (2012). See page: 90

[217] P. Massignan, M. Zaccanti, and G. M. Bruun. *Polarons, dressed molecules and itinerant ferromagnetism in ultracold Fermi gases*. Reports on Progress in Physics **77**, 034401 (2014). See page: 90

[218] A. Schirotzek, C.-H. Wu, A. Sommer, and M. W. Zwierlein. *Observation of Fermi Polarons in a Tunable Fermi Liquid of Ultracold Atoms*. Physical Review Letters **102**, 230402 (2009).

[219] C. Kohstall, M. Zaccanti, M. Jag, A. Trenkwalder, P. Massignan, G. M. Bruun, F. Schreck, and R. Grimm. *Metastability and coherence of repulsive polarons in a strongly interacting Fermi mixture*. Nature **485**, 615–618 (2012).

[220] M. Koschorreck, D. Pertot, E. Vogt, B. Fröhlich, M. Feld, and M. Köhl. *Attractive and repulsive Fermi polarons in two dimensions*. Nature **485**, 619–622 (2012).

[221] W. Ong, C. Cheng, I. Arakelyan, and J. Thomas. *Spin-Imbalanced Quasi-Two-Dimensional Fermi Gases*. Physical Review Letters **114**, 110403 (2015).

[222] M. Cetina, M. Jag, R. S. Lous, I. Fritsche, J. T. M. Walraven, R. Grimm, J. Levinsen, M. M. Parish, R. Schmidt, M. Knap, and E. Demler. *Ultrafast many-body interferometry of impurities coupled to a Fermi sea*. Science **354**, 96–99 (2016).

[223] F. Scazza, G. Valtolina, P. Massignan, A. Recati, A. Amico, A. Burchianti, C. Fort, M. Inguscio, M. Zaccanti, and G. Roati. *Repulsive Fermi Polarons in a Resonant Mixture of Ultracold Li 6 Atoms*. Physical Review Letters **118**, 083602 (2017).

[224] G. Ness, C. Shkedrov, Y. Florshaim, O. K. Diessel, J. von Milczewski, R. Schmidt, and Y. Sagi. *Observation of a Smooth Polaron-Molecule Transition in a Degenerate Fermi Gas*. Physical Review X **10**, 041019 (2020). See page: 90

[225] J.-G. Chen, T.-S. Deng, W. Yi, and W. Zhang. *Polarons and molecules in a Fermi gas with orbital Feshbach resonance*. Physical Review A **94**, 053627 (2016). See page: 90

[226] T.-S. Deng, Z.-C. Lu, Y.-R. Shi, J.-G. Chen, W. Zhang, and W. Yi. *Repulsive polarons in alkaline-earth-metal-like atoms across an orbital Feshbach resonance*. Physical Review A **97**, 013635 (2018).

[227] J. Xu and R. Qi. *Polaronic and dressed molecular states in orbital Feshbach resonances*. The European Physical Journal D **72**, 65 (2018). See page: 90

[228] J.-G. Chen, Y.-R. Shi, X. Zhang, and W. Zhang. *Polarons in alkaline-earth-like atoms with multiple background Fermi surfaces*. Frontiers of Physics **13**, 136702 (2018). See page: 90

Danksagung

An erster Stelle möchte ich mich ganz herzlich bei meinem Doktorvater Immanuel Bloch bedanken, der mir die Gelegenheit gegeben hat, mich in einem fantastischen wissenschaflichen Umfeld zu entwickeln. Seine stets positive und motivierende Führungsart und großartige Intuition habe ich im laufe meiner Promotion sehr geschätzt. Für die Leitung des Ytterbium-Experimentes und die tägliche Betreuung bei der Arbeit bin ich Simon Fölling tief dankbar. Dank seines endlosen Wissens über eine beeindruckende Vielfalt von Thematiken und seiner Freude beim Lösen jeglicher Art von Labormysterien habe ich unglaublich viel von ihm lernen können.

Der Alltag am Experiment besteht natürlich aus einer engen Teamarbeit und ich war sehr glücklich, mit der Unterstützung von hochbegabten Kollegen das Experiment durchzuführen. Für die schöne und aufregende Zeit innerhalb und außerhalb des Labores möchte ich mich bei Nelson Darkwah Oppong, Giulio Pasqualetti, Luis Riegger und Moritz Höfer herzlich bedanken. Auch hatte ich das Glück, von den Beiträgen vieler Theorie-Kollegen zu profitieren. Besonders dankbar bin ich Meera Parish und Jesper Levinsen für aufschlussreiche Diskussionen über die orbitale Feshbach-Resonanz in ^{171}Yb.

Viele wichtige technische Projekte zur Weiterentwicklung des Experiments wurden von talentierten Praktikanten oder Bachelor-/Masterstudenten durchgeführt. Dafür möchte ich mich bei Benjamin Schiffer, Florian Fertig, Caroline Tornow, Alexander Impertro und Benedict Röcken bedanken. Ich möchte mich auch bei Bodo Hecker, Karsten Förster und Olivia Mödl von der elektronischen Werkstatt und bei Ildiko Kecskesi, Kristina Schuldt und Doreen Seidl von der Verwaltung für die reibungslose Zusammenarbeit herzlich bedanken. Besonders dankbar bin ich Ildiko für ihre unglaubliche Geduld und ihr Verständnis, wenn ich von der Bürokratie überfordert war.

Allen Mitgliedern der Bloch Gruppe danke ich für die gute Atmosphäre und die schönen Momente auf Konferenzen oder Group Retreats. Insbesondere danke ich allen Kollegen aus den Boson, Fermi I, Fermi II, Caesium und SQM Laboren an der LMU für die vielen interessanten Gespräche, das regelmässige Beschaffen von Laborbedarf und die zahlreichen Mittagspausen in der ganzen Maxvorstadt.

Au cours mes études à Lausanne ainsi qu'à Zurich, j'ai eu l'immense bonheur de pouvoir compter sur un groupe incroyable d'amis physiciens qui m'entourent encore aujourd'hui malgré la distance qui parfois nous sépare. Merci d'avoir égayé tous mes semestres, pour les retrouvailles régulières et magiques, pour les visites ainsi que pour les innombrables parties de cartes, surtout en pleine pandémie. Avec ceux d'entre vous qui avez partagé une partie de mon quotidien à Munich, je garde en mémoire nombre de moments passés ensemble tels que les concerts classiques au Gasteig, les soirées karaoké fort douteuses, les ballades à vélo en

Haute-Bavière ou encore l'initiation à l'Eisstockschießen.

Je voudrais également remercier mes parents et ma famille pour leur présence constante et leur soutien inconditionnel durant mes études. J'ai toujours été ravi de vos déplacements réguliers en Bavière pour venir me tenir compagnie et m'épauler. De plus, mes retours à la maison durant ces dernières années, à Lausanne comme dans les Préalpes vaudoises, ont été comme des parenthèses enchantées dans un havre de paix et je vous en suis extrêmement reconnaissant.

At last but not at least, I would like to thank Reshma for the marvelous time spent together here in Munich. Life is definitely more enjoyable goofing around, going on intrepid trips and watching Malayalam movies with you. Thank you so much for everything, I am very excited to start now the next chapter of our wonderful adventures. To many more Kappa Beef dinners and crazy Wiesn together!